Simulating Wintertime Lake Dynamics Using the MITgcm Ice Model

by

Sarah Walsh

A thesis
presented to the University of Waterloo
in fulfillment of the
thesis requirement for the degree of
Master of Mathematics
in
Applied Mathematics

Waterloo, Ontario, Canada, 2020

Author's Declaration

I hereby declare that I am the sole author of this thesis. This is a true copy of the thesis, including any required final revisions, as accepted by my examiners.

I understand that my thesis may be made electronically available to the public.

Abstract

Lake Erie is an important source of drinking water, a location for recreational activities and a haven for unique ecosystems (e.g. Point Pelee). Recent research has suggested that some wintertime processes are significantly increasing amounts of hypoxic water and harmful algal blooms found in the lake during the following summer. Much of the mixing in Lake Erie is caused by wind forcing. Mixing also occurs via an unstable water column that results from incoming solar radiation when water is below the temperature (around 4 degrees) at which the maximum density occurs. This thesis reports on several highly idealized lake ice simulations using MITgcm (Massachusetts Institute of Technology General Circulation Model). The MITgcm is a 3D ocean model with the ability to model sea ice that was specifically chosen for this work because of its fully nonhydrostatic capabilities. This work was carried out with the intention of gaining a clear understanding of the MITgcm and some of its packages so that the model may be confidently applied to future work involving Lake Erie.

In this thesis, we consider small rectangular lakes with a partial ice cover of constant thickness. We vary several parameter settings for our simulations including initial surface temperature, air temperature, incoming shortwave and longwave radiation, wind forcing, rotation, horizontal domain size, and horizontal resolution. We also carry out simulations using the fully nonhydrostatic version of the MITgcm as well as simulations using hydrostatic approximation. Results from this work suggests that the ice cover acts as a barrier between the wind forcing and the surface of the lake. We observe that the surface currents are generally much weaker in ice-covered regions. Applying the hydrostatic approximation results in less symmetry among the surface currents. Lakes with larger horizontal domains require more time to force a proportional amount of ice across the lake compared to smaller lakes under similar forcing, there is also less ice pile-up observed in the larger lake in terms of height. Rotation also appears to have more influence over larger lakes compared to smaller lakes. Overall, the simulations behave as expected, however some results have been puzzling, such as noise occurring in the net upward heat flux for larger lakes. This thesis also discusses issues we have faced with the model, which includes ice growth during above freezing temperatures, ice remaining stagnant due to strange behaviour of momentum solvers, and confusion surrounding the model's computation of net upward shortwave radiation.

Acknowledgements

Thank you to my supervisors Marek Stastna, Kevin Lamb, and Andrea Scott for all of your teachings and guidance throughout the last two years. I also want to extend an additional thank you to Michael Waite and Francis Poulin for agreeing to be on my thesis committee and reviewing my work.

Thank you to my parents for always valuing and nurturing my love of learning. Thank you to my brothers for the support and a fun time whenever we get to see each other. A big shout-out to my cat Chris who I adopted the first month after beginning this degree. You have been the best (if not the most aggressive) roommate I could have asked for.

Thank you to everyone who has made a positive impact on me at the University of Waterloo and who has made this feel like a home. Thank you to all of my past and present officemates for the fun chats and answering my questions. Specifically, thank you to Lizz for being a friendly face since day one of our degree, and thank you for being a friend that I can count on inside and outside of academia. Thank you to the entire fluids lab for all the help and for being a welcoming environment. Thank you to my DnD group for letting me join your campaign and for giving me something to look forward to on Thursday nights.

Thank you to my friends in Nova Scotia for the support and love from afar. In particular, I want to extend a huge thank you to my friend Shyla for spending many Friday nights with me over voice chat playing video games, watching Netflix, and listening to all of my nonsense. Your consistent friendship has provided me with so much comfort and fun, especially while starting a new program in a new location where I didn't know anyone.

Dedication

To my cat, Chris.

Table of Contents

List of Tables

List of Figures

Chapter 1

Introduction

1.1 Lake Ice

Lakes are bodies of fresh water, surrounded by land, that exist in a wide variety of sizes ranging from small ponds to large basins with areas greater than $10,000$ km^2. The Earth is composed of approximately $125,000$ km^3 of lake water. Lakes can be found in any climate, but in order for lakes to freeze, there must be some recurring period during the year where the average air temperature decreases beneath 0°C. Note that not all lakes located in the aforementioned climates freeze depending on size and geothermal heating. Depending on the size and location of the lake, it may possess a permanent ice cover, or it may partially or completely freeze over during the colder times of the year. The size and depth of the lake will also determine the amount of time required for ice to develop, and potentially fully cover the lake. Seasonally freezing lakes will initially begin growing ice during autumn with ice first growing from the shore inward. In the spring, the ice will begin melting from the shore as well [Leppäranta, 2015].

Lakes that freeze over are essential components of the ecosystem, economy, and community enjoyment. For example, frozen lakes, under sufficient conditions, allow for transportation for various goods and recreational activities such as ice skating and ice fishing. Lake ice may contain impurities that originate from the water of the lake, bottom sediments, or the atmosphere. The environmental impacts of this can be experienced when the ice melts and breaks up. The ice decay causes the impurities to be released which may affect water quality of the lake [Salonen et al., 2009]. Moreover, ice covers significantly impedes the amount of oxygen that can get into the water. This can cause hypoxic water and may result in fish mortality, impacting our ecosystem and economy. Hypoxic water

can also be lethal for insects and invertebrates that are stuck in the lake sediments. The freeze-over period also impacts the hydrological year, the twelve months in which precipitation is measured via its impact on runoff. The ice cover of a lake may show significant variability between years, thus it is important that we have an accurate understanding of the process and how it can influence phenomena such as climate change [Leppäranta, 2015].

In the past, we have used results from sea ice research to help direct lake ice research. According to Leppäranta [2015], less research has been done on lake ice because it was more practical to study sea ice. In general, compared to river ice and sea ice, lake ice is more straightforward to study. This is because lake ice covers move around less and freshwater lake ice contains smaller amounts of impurities (however, if the lake ice does move around a lot, then the ice may behave more similarly to river ice). The most important impurities in freshwater lakes are gas bubbles, however for sea ice the most important impurities are liquid brine. It is clear that we need to have an understanding of lake ice, however research in this area has been challenging because safety concerns make it difficult to gather and measure data in the field. Nevertheless, some research has been done pertaining to lake ice. Early scientific lake ice research began during the 1800s when physical limnology and lake hydrology also began its research roots. Freezing and thawing of lakes were observed even before scientific research began because of religion, culture, curiosity, and practicality (e.g. transport) reasons. Until around the 1970s, lake ice research was sporadic. Then, in the 2000s, lake ice research took-off once again, as a response to climate change and environmental concerns (e.g. [Magnuson et al., 2000]) [Leppäranta, 2015].

The flow and deformation of ice can be described by rheology. Natural lake ice has a fairly complicated rheology and it is a polycrystalline medium, meaning that it is formed of many different sized tiny crystals. A lake's ice cover is dependent on its freezing patterns. For instance, if a lake has a seasonal ice cover, then the ice cover tends to be much thinner than the depth of the lake. A lake with a seasonal ice cover will have: relatively large individual crystals, many impurities, and a high homologous temperature (a fraction of the absolute ice temperature to approximately 0°C). These three factors result in an ice cover with properties that may vary significantly [Leppäranta, 2015]. There are crucial differences in how processes occur in open water compared to water with an ice cover. If the water is ice covered, then it is shielded from wind forcing, and so the turbulence and mixing is decreased. Since the ice is acting as a barrier between the atmosphere and lake, the lake water body will absorb much less incoming radiation as well. Moreover, in an ice-covered lake, the temperature profile and circulation is relatively stable. When the lake is located in a cold climate, the absolute humidity of the air is small. This results in smaller mass and heat fluxes because of evaporation and sublimation than in a warmer

climate [Leppäranta, 2015].

A developing ice cover is mainly a thermodynamic process [Leppäranta and Wang, 2008]. The ice will create a stable cover over the lake when it becomes thick enough. If the ice becomes weak, or the lake is just very large, the ice will begin to break as the ice loses its strength as it melts. Ice melt is considered to be a thermo-mechanical process [Leppäranta, 2015]. When the ice melts near the shoreline, the ice detaches from the boundary, once this is accomplished the wind and currents are free to force the ice to move around. Of course, once the ice begins to move around because of the forcing the ice will break even more and the ice-decay process will increase in speed. Note that, for very large lakes, there may be some episodic movement that disturbs the water body.

Note that, in this thesis, we do not consider snow. However, snow is a very important component of lake ice. The only situation in which a lake with an ice cover is snow free is when the lake is in a very cold and dry region. Typically, there is a basic stratification pattern where there is congealed ice and snow-ice. It is important to consider the interaction between snow and an ice cover because of processes such as heat exchange between the lake and atmosphere, and radiation from the sun. When a lake has an ice cover, much less sunlight reaches the surface, this impediment is further exaggerated when there is a layer of snow on top of the ice. Slush is also a consideration as it is transformed into snow-ice when the temperature is cold [Leppäranta, 2015].

1.2 Lake Erie

In this thesis, the lake that we are carrying the present investigation to understand better is Lake Erie. Lake Erie is composed of fresh water and is one of the Laurentian Great Lakes. It located in North America and surrounded by Southern Ontario, Michigan, Ohio, Pennsylvania, and New York. Lake Erie is the smallest of the Great Lakes in terms of volume and it is divided into three basins (western, eastern, and central). Using Leppäranta [2015] as a guide, we can classify the central basin of Lake Erie, which has a maximum depth of 25 m and is approximately 85 km wide and 180 km long, as a large shallow lake [Hawley et al., 2018]. Table 1.1 gives the average depth, area, and volume of water in Lake Erie broken down by its western, central, and eastern basins [Assel, 1990]. Because the lake is large, waves created as a result of wind can be very significant to the mixing process and since the lake is shallow, the lake will generate a (partial) ice cover most winters.

Table 1.1: The average depth, area, and volume of Lake Erie.

	Western Basin	**Eastern Basin**	**Central Basin**
Average Depth (m)	9	27	19
Area (km^2)	5,135	5,909	14,635
Volume (km^3)	46	159	278

Lake Erie has an annual ice cycle, but does not usually freeze over completely (approximately 90% of the lake will freeze over in a typical year). The ice cycle consists of a cooling period during the fall, an ice-forming period during the winter, and an ice-melt period during the spring. During the fall and winter, the temperature of the surface water is higher than the air temperature. This creates an atmospheric instability and the lake heat storage decreases via sensible heat loss and evaporation. Ice begins to form over the shallow western basin, typically from the shore inwards, before forming over the deeper central and eastern basins. According to Assel [1990], the water column below the ice cover is approximately isothermal at a water temperature lower than 1°C. The ice melts in the spring-time due to warmer air temperatures, and the absorption of solar radiation by the ice and the layer of surface water beneath the ice. If the wind is blowing heavily, the upwelling of warmer water can contribute to ice melt. How long it takes for the ice to melt is dependent on various factors such as the amount of ice present, wind, storms, and rate of warming. Typically, Lake Erie attains its maximum ice cover in January and maintains it throughout February.

Lake Erie suffers from harmful algal blooms (HABs) and hypoxic water (water with a low oxygen concentration). Hypoxic water is detrimental, and can be lethal, for fish populations and for insects and invertebrates stuck in the lake sediments. Wintertime processes can increase the amount of hypoxia and HABs. The blooms of phytoplankton under the ice in Lake Erie are stronger than the blooms observed during the spring Twiss et al. [2012]. If the total amount of time with an ice cover over the Great Lakes decreases, there could be a significant and negative impact on both the ecosystem and the economy of surrounding areas. Some harmful economic impacts are lower lake levels, escalated evaporation, and a condensed time-period where activities such as ice-fishing and transporting over the ice cover can be done. Some negative impacts on the ecosystem include modifications to the current fish found in the Great Lake and increased phosphorus levels. It was discovered by Nicholls [1998] that phosphorus concentrations found in Lake Huron were negatively correlated with the amount of surface area of the lake covered by ice. This may be because, during an ice-free winter, wind keeps the phosphorus suspended in the water column and then water masses with high phosphorus concentrations are dispersed far away from the

shore. The ice cover impacts the energy and mass transfer to and from the lakes and therefore affects the ecosystem within the lake [Assel et al., 2003, Assel, 2004]. Having wide-spread ice cover over the Great Lakes will affect storms, regional weather, the hydrological cycle, water levels, water temperatures [Wang et al., 2010], and lake circulation [Fujisaki et al., 2012, Hawley et al., 2018].

It is widely understood that having knowledge on the ice cover, specifically the thickness, over Lake Erie is important. However, logistical reasons make it very difficult to gather direct observations [Hawley et al., 2018]. Consistent observations of the ice cover over the Laurentian Great Lakes by the Canadian and American government began in the early 1960s. Not much is known about the climatology of the ice cover previous to the 1960s since the ice cover was not well documented. In order to give an approximate understanding of the mid-lake ice cover, Assel [1990] used a statistical model to simulate the ice cover for Lake Erie and Lake Superior from the the late 1890s to the late 1990s.

Even though research has been done during the late spring and summer, there have not been as many extensive studies regarding the winter limnology of Lake Erie. Consequently, when modelling wintertime conditions of Lake Erie, assumptions about certain rate and state variable must be made and can lead to biased predictive results. Chandler [1940, 1942b,a, 1944, 1945] performed the most complete study of the winter limnology of the Great Lakes thus far. In this study, he noted diatom blooms in the mid-winter under the ice in the western basin of Lake Erie. Here, there was a low zooplankton biomass, and the light environment was varied [Twiss et al., 2012]. It is not well understood how diatomic blooms in Lake Erie occur during the wintertime. This is relevant since diatoms have been associated with nucleation sites for frazil ice which, in turn, increases the number of diatoms near the lake surface and in the ice [D'souza et al., 2013].

1.3 Lake Ice Models

Mathematical models for environmental phenomena are used in many areas such as weather forecasting and hydrology. Since the 2000s, the mathematical modelling of lake ice has become enticing and gained traction to researchers in the field. Some main areas of interest related to mathematical modelling of lake ice are: ice growth and ice melt, the transfer of radiation through the ice into the lake, ice forces, and the drifting of ice [Leppäranta, 2015]. In this section, we will discuss several models and some of their key features and distinctions.

Dynamic circulation models are concerned with advection and atmospheric circulation

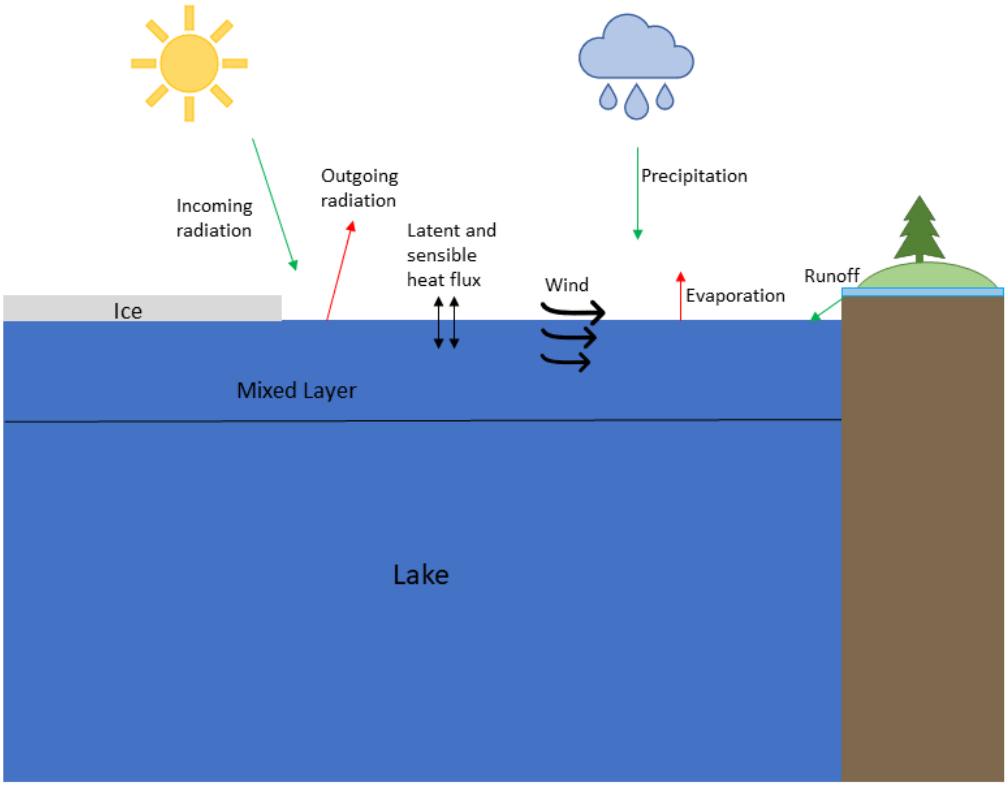

Figure 1.1: The vertical cross-section of a lake with a mixed layer and a partial ice cover. Processes shown include: incoming and outgoing radiation, latent and sensible heat fluxes, evaporation, precipitation, runoff, and wind forcing.

related processes such as wind and pressure systems. Dynamic ice models deal with phenomena such as momentum forcing from the lake surface and atmosphere, internal ice stress, and ice strength and deformation. For instance, a study carried out by Campbell [1965] considered ice movement as a result of only air stress, water stress, stress transmitted though the ice, the Coriolis force, and the pressure gradient as a result of sea surface tilting. Thermodynamic ice models take ice temperature, heat fluxes, and phase changes into consideration. See figure 1.1 for a visual of some processes that lake ice models consider. Thermodynamic ice models may include components such as snow on top of the ice, sensible and latent heat stored within the snow-ice system, converting snow to ice when snow sinks into the water, and the existence of leads [Fichefet and Maqueda, 1997]. The most difficult component of thermodynamic lake ice models is the snow layer [Leppäranta, 2015]. Prior to 1990, thermodynamic lake models were relatively simple in the sense that ice growth occurred on freezing-degree-days and melt took place on positive-degree-days [Leppäranta, 2009]. Numerical models were also used such as the one-dimensional ice cover model discussed in [Croley and Assel, 1994].

In this section we will discuss examples of ice models that are 1-dimensional and 3-dimensional. 1-dimensional models are also known as column models. A single column model can be studied on its own, or comprise a full 3-dimensional general circulation model (GCM). Cells that form a GCM interact with one another through large-scale dynamics [Randall]. Single column models do not have neighbouring grid columns beside them as in GCMs. Consequently, the user must feed data to 1-dimensional models. One very common practice with column models is to feed them observational data, another option is to present the model with specific data to simulate a desired scenario. 1-dimensional models lack large-scale dynamics and 3-dimensional models give far more information, however column models are very computationally inexpensive. We will discuss here two examples of 1-dimensional lake ice models: CLIMo (Canadian Lake Ice Model) and FLake.

CLIMo is based on the 1-dimensional sea ice model by Flato and Brown [1996] that has been used for various lake ice studies [Ménard et al., 2002]. This model solves the 1-dimensional unsteady heat conduction equation from Maykut GA and Untersteiner N [1971] and it was specifically created for studying ice over freshwater bodies. This model possesses a fixed-depth mixed layer, and a user-defined number of ice layers. The mixed-layer temperature is set to the freezing temperature when ice is present and is computed according to the surface energy budget when no ice is present. The majority of parameter settings used by CLIMo are similar to those of Ebert and Curry [1993]. CLIMo is somewhat unique in the way it parameterizes snow conductivity and heat capacity, and surface albedo. Essentially, the value of the surface albedo relies on the surface type (ice, open water, or snow), the surface temperature, and the ice thickness. Details regarding CLIMo and its

parameterizations and equations may be found in Duguay et al. [2003].

FLake [1] is a freshwater lake model used for lakes of various depths and time-scales to predict vertical temperature profiles and mixing conditions. The model was created to be used as a lake parameterization scheme in climate modelling, weather prediction, and other environmental prediction applications. FLake may also be used as an independent lake model [Kirillin et al., 2011]. Unlike CLIMo, which only considers the temperature of the mixed-layer, FLake accounts for the thermocline of the lake, i.e. the layer between the upper mixed layer and the bottom basin layer, by using the concept of self-similarity of the temperature-depth curve. FLake uses an identical concept to model the structure of the temperature for the stratified layer located between the bottom basin and the upper mixed layer. This method is also used to describe the ice and snow cover as well as the upper layer of bottom sediments. As a result, FLake is a computationally efficient 1-dimensional bulk model that accounts for most of the crucial physics that occur in lakes [Reinert et al., 2008].

The 1-dimensional models previously discussed are incapable of capturing many key processes necessary to accurately model larger lakes, where both dynamics and thermodynamics are important. Specifically, 1-dimensional models are unable to simulate ice deformation through mechanical forcing, or the 3-dimensional dynamics of the underlying water. Moreover, CLIMo and FLake were created specifically for modelling lakes. However, numerous 3-dimensional models have been developed to model ocean circulation and sea ice (e.g., Semtner [1976] and Maykut GA and Untersteiner N [1971]) rather than lakes and lake ice. We may apply these models to lakes and lake ice as well. Some hydrodynamic models that we will mention are ROMS, FVCOM, NEMO, and the MITgcm. We will also briefly discuss a popular ice model known as CICE.

ROMS (Regional Ocean Modelling System) is a popular 3-dimensional hydrostatic finite-difference general ocean circulation model commonly utilized by the ocean modelling community. ROMS uses the primitive equations, a split-explicit time stepping scheme, terrain-following coordinates, and a free-surface. Since this model employs terrain-following coordinates, it allows for a better resolution near the surface and bottom of the water body. ROMS is a large scale model, so it is best suited to simulate ocean processes on the scale of 10 km - 10,000 km. The hydrostatic limitations of this model result in it being of little use when nonhydrostatic processes are essential. It should be pointed out that a nonhydrostatic version of ROMS has been produced [Kanarska et al., 2007, Buijsman et al., 2010], but it is not the standard version of ROMS open to the community [Choboter et al., 2016]. ROMS does include algorithms to handle sea ice applications, and the sea ice model for

[1] http://www.flake.igb-berlin.de

ROMS is described in Budgell [2005], Kasper and Weingartner [2015]. Although ROMS is an ocean model, it has been used to model the ice cover of lakes before. For example, ROMS has been used to model the ice cover of Lake Superior at a 5 km resolution [White et al., 2012].

CICE (Los Alamos Sea Ice Model), sometimes referred to as the Community Ice CodE, is the most widely used model globally for sea ice. This sea ice model is computationally efficient at modelling ice growth, melt, and movement, and can be coupled with a global climate model or used as a stand-alone sea ice model [Roberts et al., 2018]. CICE uses Elastic-Viscous-Plastic rheology, has several ice-thickness categories, and has 1D parameterizations of frazil ice and snow. CICE consists of a thermodynamic model which calculates local growth rates of ice and snow by considering snowfall and radiative, conductive, and turbulent heat fluxes. CICE also includes an ice dynamic model that is used to predict the velocity field of ice, variables of state, and a transport model for advection of areal ice concentration. More details regarding CICE can be found in Hunke and Lipscomb [2010].

FVCOM (Finite Volume Community Ocean Model) is a model that has been used for studying coastal oceans (e.g., Chen et al. [2011]) as well as the Great Lakes (e.g., Wilson et al. [2013]). FVCOM is an unstructured grid, free-surface 3-dimensional coupled ocean circulation model that uses an the primitive equations developed by Chen et al. [2006]. This model can also be coupled with a sea ice model. The model was created to study oceans and estuary systems, and was developed to be computationally efficient and to use an unstructured grid. Irregular topography of the sea floor is captured via terrain following coordinates (σ-coordinates). FVCOM allows for different grid resolutions to be used in near-shore and off-shore regions. The unstructured triangular grid in the horizontal and sigma coordinates in the vertical allow this model to be capable of resolving coastlines and coastline bathymetry [Niu et al., 2015]. Horizontal mixing in this model follows the Smagorinsky eddy parameterization [Smagorinsky, 1963]. The original version of FVCOM used the hydrostatic approximation, however validation experiments were performed in 2010 to test out a nonhydrostatic version of the model (FVCOM-NH) [Lai et al., 2010b,a].

NEMO (Nucleus for European Modelling of the Ocean) is being used by Environment and Climate Change Canada for ocean modelling and the Great Lakes. In general, NEMO is a well-supported and popular choice in the ocean modelling community and has been constantly evolving since its original development. In its original conception, NEMO was an ocean model that could be coupled with a sea ice model such as CICE. More recently however, a sea ice model (SI^3) for NEMO has been developed that combines the abilities of CICE, and two other models originally used in NEMO. According to its website (`https://www.nemo-ocean.eu/`), NEMO is a model with three main components: NEMO-

OCE, that models the (thermo)dynamics of the ocean and solves the primitive equations [NEMO System Team]; NEMO-ICE, that models sea ice (thermo)dynamics [NEMO Sea Ice Working Group]; and NEMO-TOP, that models oceanic tracers transport and biogeochemical processes [NEMO TOP Working Group].

This thesis uses the MITgcm (Massachusetts Institute of Technology general circulation model) [Marshall et al., 1997a,b] for all simulations discussed. More information regarding the MITgcm and its packages will be given in chapter two of this thesis. The MITgcm is a general circulation model that has the capability to model both oceanographic and atmospheric processes. This model uses the finite volume method and z-coordinates. The MITgcm includes several packages to capture various physical processes such as a sea ice package, an external forcing package, and a K-profile parameterization (an upper ocean turbulent mixing scheme) package. One reason for choosing the MITgcm for our research is the model's nonhydrostatic capabilities.

A brief comparison of all the models discussed in this section can be found in table 1.2. Several of these models (ROMS, FVCOM, NEMO) are hydrostatic. Hydrostatic models work well for large-scale processes at low resolutions when horizontal length-scales are much larger than vertical length scales, however for small-scale processes at higher resolutions they are not as effective. Most ocean general circulation models are hydrostatic. These hydrostatic models can and have been (e.g. ROMS [White et al., 2012] and NEMO [Dupont et al., 2012]) used for lake and lake ice simulations, but the inability to model small-scale processes well is an issue. One of the main benefits to using the MITgcm is that it has nonhydrostatic capabilities.

Table 1.2: The 7 models discussed in this section.

	1D/3D	**Advantages**
CLIMo	1D	Unique snow conductivity and surface albedo parameteriztions
FLake	1D	Efficient, accounts for lake thermocline
ROMS	3D	Efficient numerical scheme, commonly used in ocean modelling communities
CICE	3D	Most commonly used model for sea ice
FVCOM	3D	Capable of resolving coastlines and coastline bathymetry
NEMO	3D	Very commonly used and constantly updated
MITgcm	3D	Nonhydrostatic capabilities

1.4 Format of Thesis

This thesis discusses high resolution lake ice simulations in an idealized, rectangular domain. Several simulations are explored, altering one parameter at a time for the purpose of easy comparison. The goal of this thesis is to gain a greater understanding of lake ice dynamics when using the MITgcm and the external forcing, KPP, and SEAICE packages. More specifically, we aim to understand how small-scale processes under wintertime conditions work in toy lake simulations when using the MITgcm. This knowledge will eventually be applied to future projects involving Lake Erie.

The format of this thesis is as follows. Chapter two provides an in depth exploration of the MITgcm governing equations and package components. Chapter three discusses a problem with ice growth when the surface temperature is above freezing. Four simulations are studied in this chapter with varying values assigned for downward shortwave and longwave radiation, air temperature, and water temperature in an attempt to understand the ice-growth issue. Chapter four discusses several other simulations where we consider a basic setup of a lake with a partial ice cover and wind forcing. A handful of parameters were varied to monitor how small-scale processes were affected. These parameters include wind forcing, horizontal lake size, horizontal resolution, rotation, and whether or not the simulation was executed using the fully nonhydrostatic model or the hydrostatic model. Finally, chapter five concludes by discussing the main results and future work.

Chapter 2

Background and the MITgcm

2.1 Introduction to the MITgcm

All simulations discussed in this thesis were carried out using the MITgcm. The MITgcm [Marshall et al., 1997a,b] is 3D general circulation model that is very efficient, portable, and may be executed using parallel computing [Adcroft et al., 2004]. The MITgcm has been used in several ocean, lake, and ice studies. For example, Jensen et al. [2018] used the MITgcm to explore sea ice in the Nordic Seas. Additionally, Dorostkar et al. [2010] used temperature measurements from the Cayuga Lake to validate the output from the MITgcm, since the model had not been validated against observational data at that point. Furthermore, a 2010 study performed by Bennington et al. [2010] used the MITgcm to model Lake Superior to study its large-scale circulation relative to climatology and inter-annual variability.

The MITgcm has the capability to model both oceanographic and atmospheric processes. The model can utilize the hydrostatic approximation, but it also has fully nonhydrostatic capabilities. The MITgcm applies the finite volume discretization method (i.e., the governing equations are integrated over finite volumes that make up a discrete grid) and orthogonal curvilinear coordinates to aid in modelling abnormal geometries. Moreover, the model uses the incompressible Navier-Stokes equations conservatively on a staggered Arakawa C-grid [Adcroft and Campin, 2004]. One of the many possible options that the MITgcm may use to model subgrid-scale processes is to use KPP for the vertical diffusivities [Large et al., 1994] and to use the eddy parameterization for horizontal diffusivity given by Smagorinsky [1963]. The model uses the Adams-Bashforth time-stepping method [Marshall et al., 1997a] [Djoumna et al., 2014].

The MITgcm was originally developed for studying the atmosphere and climate. The model was designed with the goal to simulate both small-scale and large-scale processes due to its nonhydrostatic capabilities, a stand-out feature of the MITgcm compared to many other general circulation models. The nonhydrostatic capabilities of the model indicates that it does well with simulating mixing processes. The model also does well modelling mixing and dynamical processes with steep topography when the finite volume method is used. The MITgcm has three options for dealing with the upper boundary: rigid lid, linear free-surface, and non-linear free-surface [Adcroft and Campin, 2004]. Furthermore, the MITgcm is able to simulate snow and ice. The MITgcm models ice with multiple ice thickness categories, and can model 1D parameterizations of snow and frazil ice.

The MITgcm has a number of packages available to be used with the base ocean model (see figure 2.1). The packages that we will be using in this thesis include: the diagnostics package, the external forcing package, the KPP (K-Profile Parameterization) package, and the SEAICE package. These packages allow us to choose which data outputs we wish to see, use a more advanced vertical mixing scheme, incorporate dynamics, and use a coupled dynamic thermodynamic ice model. We will go into these packages in more depth later in this chapter.

Please note that much of this chapter has been paraphrased from the MITgcm documentation[1] and is included for completeness.

[1] https://mitgcm.readthedocs.io/en/latest/

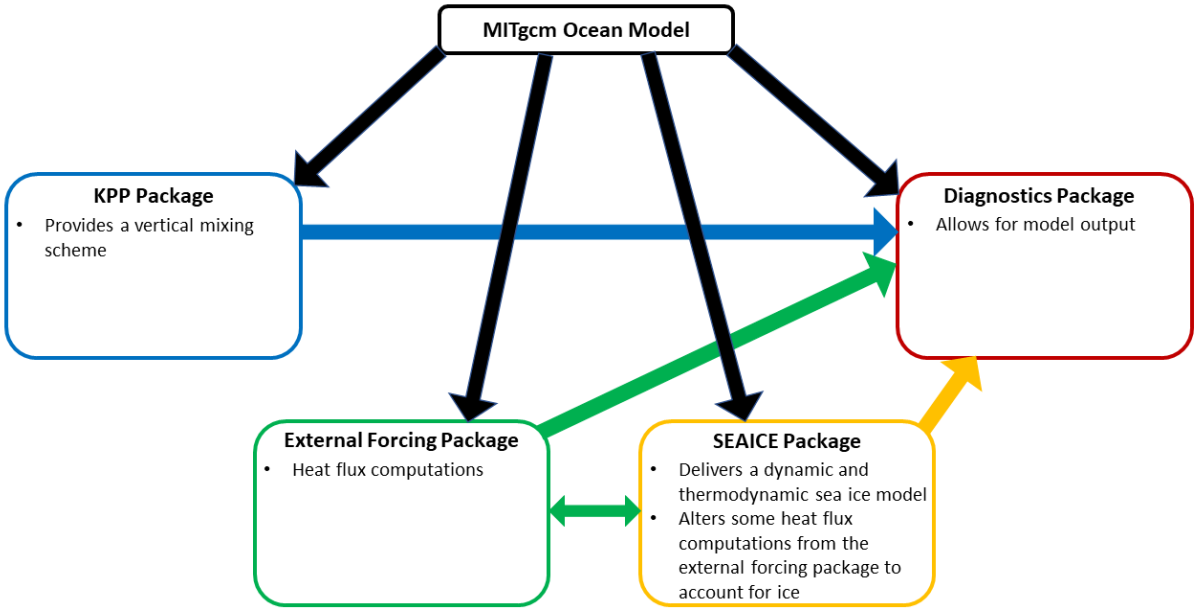

Figure 2.1: Schematic showing how the MITgcm ocean model works together with the packages we are using in this thesis and their main contributions to the model.

2.2 Governing Equations of the MITgcm

The MITgcm can be used to model both the ocean and the atmosphere. Since this thesis exclusively focuses on lake modelling, all terms found in any equations will be in reference to water bodies only and not the atmosphere. The following equations are for the semi-compressible Boussinesq equations. The fluid is semi-compressible because the density is a function of potential temperature and depth rather than potential temperature and pressure. This is accomplished by

$$\frac{Du}{Dt} - fv + \frac{1}{\rho_o}\frac{\partial p'}{\partial x} = \mathcal{F}_u, \tag{2.2.1}$$

$$\frac{Dv}{Dt} + fu + \frac{1}{\rho_o}\frac{\partial p'}{\partial y} = \mathcal{F}_v, \tag{2.2.2}$$

$$\epsilon_{nh}\frac{Dw}{Dt} + \frac{g\rho'}{\rho_o} + \frac{1}{\rho_o}\frac{\partial p'}{\partial z} = \epsilon_{nh}\mathcal{F}_w \tag{2.2.3}$$

where: x and y are the horizontal coordinates and z is the vertical coordinate; $\vec{\mathbf{v}} = (u, v, w)$ is the velocity vector with u and v as the horizontal components and w as the vertical component; $\hat{i}$ and $\hat{j}$ are unit vectors in the horizontal and $\hat{k}$ is the unit vector in the vertical; $\frac{D}{Dt} = \frac{\partial}{\partial t} + \vec{\mathbf{v}} \cdot \nabla$ is the material derivative and it represents the time rate of change of any quantity (such as velocity) moving with the fluid particle at velocity $\vec{\mathbf{v}}$ and $\nabla = \hat{i}\frac{\partial}{\partial x} + \hat{j}\frac{\partial}{\partial y} + \hat{k}\frac{\partial}{\partial z}$ is the gradient operator; $\frac{p'}{\rho_c}$ is the water pressure where ρ_o is a fixed reference density of water; $\mathcal{F}_{\vec{\mathbf{v}}}$ are the forcing and dissipation of $\vec{\mathbf{v}}$; ϵ_{nh} is a nonhydrostatic parameter that may either be 1 or 0; and g is acceleration due to gravity.

The above equations retain compressibility in the density. This is accomplished by splitting the density such that

$$\rho = \rho_o + \rho'$$

where

$$\rho' = \rho(\theta, p_o(z)) - \rho_o,$$

and is the equation of state used for the model where θ is the potential temperature and $p_o(z)$ is a reference pressure and is a function of height. The continuity equation that the model uses is

$$\frac{\partial u}{\partial x} + \frac{\partial v}{\partial y} + \frac{\partial w}{\partial z} = 0. \tag{2.2.4}$$

Finally, the potential temperature equation is

$$\frac{D\theta}{Dt} = \mathcal{Q}_\theta, \tag{2.2.5}$$

where $\mathcal{Q}_\theta$ is the forcing and dissipation of θ.

The vertical kinematic boundary conditions are:

$$w = 0 \text{ at } z = -H, \tag{2.2.6}$$

$$w = \frac{D\eta}{Dt} \text{ at } z = R_{surface}(x, y) = \eta(x, y, t) \tag{2.2.7}$$

where H is the fixed lake bottom, and η is the height of the free-surface. Note that for the simulations we are discussing in this thesis, the bottom is always flat. Equation 2.2.6 is the bottom boundary condition and it states that there is no flow through the bottom boundary. Equation 2.2.7 is the surface boundary condition and it states that a particle at the free-surface will remain at the free-surface.

The horizontal kinematic boundary condition is:

$$\vec{\mathbf{v}} \cdot \vec{\mathbf{n}} = 0 \tag{2.2.8}$$

where $\vec{\mathbf{n}}$ is the normal vector to a solid boundary. Equation 2.2.8 states that there is no flux across the boundaries.

The MITgcm has three options to deal with the upper boundary: there is a rigid lid, linear free-surface, and non-linear free-surface. Note that we are using the linear free-surface in this thesis, the reader may see Adcroft and Campin [2004] for more details.

The MITgcm has hydrostatic, as well as nonhydrostatic, capabilities. To see what equations the model uses for the nonhydrostatic and hydrostatic form we first break-up the pressure term $\phi(x, y, z) = \frac{p(x,y,z)}{\rho_c}$ up into its surface, hydrostatic, and nonhydrostatic components such that

$$\phi(x, y, z) = \phi_s(x, y) + \phi_{hyd}(x, y, z) + \phi_{nh}(x, y, z).$$

Then, we re-write the momentum equations as:

$$\frac{\partial u}{\partial t} + \frac{\partial \phi_s}{\partial x} + \frac{\partial \phi_{hyd}}{\partial x} + \epsilon_{nh}\frac{\partial \phi_{nh}}{\partial x} = G_u, \tag{2.2.9}$$

$$\frac{\partial v}{\partial t} + \frac{\partial \phi_s}{\partial y} + \frac{\partial \phi_{hyd}}{\partial y} + \epsilon_{nh}\frac{\partial \phi_{nh}}{\partial y} = G_v, \tag{2.2.10}$$

$$\frac{\partial \phi_{hyd}}{\partial z} = -\frac{g}{\rho_c}(\rho(\theta, p_o(z)) - \rho_o), \tag{2.2.11}$$

$$\epsilon_{nh}\frac{\partial w}{\partial t} + \frac{\partial \phi_{nh}}{\partial z} = G_w, \tag{2.2.12}$$

where G_u, G_v, G_w are terms that encompass the: advection, metric, Coriolis, and forcing and dissipation terms for their respective equations. See table 2.1 for details. Note that the metric terms are included for completeness, but they are reduced to zero unless using spherical coordinates.

Table 2.1: Advection, metric, Coriolis, and forcing/dissipation terms found in the momentum equations for the nonhydrostatic model.

	Advection	**Metric**	**Coriolis**	**Forcing/Dissipation**
$G_u =$	$-\vec{\mathbf{v}}.\nabla u$	$-\left\{\frac{uw}{z} - \frac{uv\tan\varphi}{z}\right\}$	$-\{-2\Omega v\sin\varphi + 2\Omega w\cos\varphi\}$	$+\mathcal{F}_u$
$G_v =$	$-\vec{\mathbf{v}}.\nabla v$	$-\left\{\frac{vw}{z} - \frac{u^2\tan\varphi}{z}\right\}$	$-\{2\Omega u\sin\varphi\}$	$+\mathcal{F}_v$
$G_w =$	$-\vec{\mathbf{v}}.\nabla w$	$-\left\{\frac{u^2+v^2}{z}\right\}$	$+2\Omega u\cos\varphi$	$+\mathcal{F}_w$

The nonhydrostatic model solves the vertical momentum equation, and because of this it is much more computationally expensive. In addition to running as a nonhydrostatic and a hydrostatic model, the MITgcm may also be ran as a 'quasi-hydrostatic' model. In the nonhydrostatic model, all terms contained in the G_u, G_v, and G_w are considered. For the quasi-hydrostatic model, the terms for G_u, G_v, and G_w are reduced to table 2.2. The G_u, G_v, and G_w are further reduced to table 2.3 for the hydrostatic model. Note that equation 2.2.12 does not exist in the hydrostatic model.

Table 2.2: Advection, metric, Coriolis, and forcing/dissipation terms found in the momentum equations for the quasi-hydrostatic model.

	Advection	**Metric**	**Coriolis**	**Forcing/Dissipation**
$G_u =$	$-\vec{\mathbf{v}}.\nabla u$	$-\left\{\frac{uw}{z} - \frac{uv\tan\varphi}{z}\right\}$	$-\{-2\Omega v\sin\varphi + 2\Omega w\cos\varphi\}$	$+\mathcal{F}_u$
$G_v =$	$-\vec{\mathbf{v}}.\nabla v$	$-\left\{\frac{vw}{z} - \frac{u^2\tan\varphi}{z}\right\}$	$-\{2\Omega u\sin\varphi\}$	$+\mathcal{F}_v$
$G_w =$		$-\left\{\frac{u^2+v^2}{z}\right\}$	$+2\Omega u\cos\varphi$	

Table 2.3: Advection, metric, Coriolis, and forcing/dissipation terms found in the momentum equations for the hydrostatic model.

	Advection	**Metric**	**Coriolis**	**Forcing/Dissipation**
$G_u =$	$-\vec{\mathbf{v}}.\nabla u$	$+\frac{uv\tan\varphi}{z}$	$+2\Omega v\sin\varphi$	$+\mathcal{F}_u$
$G_v =$	$-\vec{\mathbf{v}}.\nabla v$	$+\frac{u^2\tan\varphi}{z}$	$-\{2\Omega u\sin\varphi\}$	$+\mathcal{F}_v$
$G_w =$				

In this thesis we are concerned with both a hydrostatic and nonhydrostatic model setup, so we will describe both time-stepping schemes here and consider an implicit linear free-surface for both cases. For both the hydrostatic and nonhydrostatic model, we use the Adams-Bashforth time-stepping.

Using the hydrostatic and implicit linear free-surface, we may re-write the horizontal momentum equations 2.2.9 and 2.2.10 (excluding the nonhydrostatic terms) and the continuity equation 2.2.4 as

$$\partial_t u + g\partial_x \eta = G_u \tag{2.2.13}$$
$$\partial_t v + g\partial_y \eta = G_v \tag{2.2.14}$$
$$\partial_x u + \partial_y v + \partial_z w = 0 \tag{2.2.15}$$

where the G vectors are containing all terms in the momentum equations besides the surface pressure gradient. Integrating the continuity equation over the depth of the fluid H we get

$$\partial_x H\widehat{u} + \partial_y H\widehat{v} = 0 \tag{2.2.16}$$

where $H\widehat{u} = \int_H u dz$ is the depth integral of u, the same process takes place for $H\widehat{v}$. If we were considering a rigid-lid approximation, then $w = 0$ at the lid. Since we are using an implicit linear free-surface, we take a linearization of the free-surface equation and get

$$\partial_t \eta + \partial_x H\widehat{u} + \partial_y H\widehat{v} = \mathcal{P} - \mathcal{E} + \mathcal{R} \tag{2.2.17}$$

where $\mathcal{P}$ is precipitation, $\mathcal{E}$ is evaporation, and $\mathcal{R}$ is runoff. So, we added on a time-dependent term and a fresh-water source term. The time discretization of the momentum equations and equation 2.2.17 are

$$u^{n+1} + \Delta t g \partial_x \eta^{n+1} = u^n + \Delta t G_u^{(n+1/2)} \tag{2.2.18}$$

$$v^{n+1} + \Delta t g \partial_y \eta^{n+1} = v^n + \Delta t G_v^{(n+1/2)} \tag{2.2.19}$$

$$\eta^{n+1} + \Delta t \partial_x H\widehat{u^{n+1}} + \Delta t \partial_y H\widehat{v^{n+1}} = \eta^n + \Delta t(\mathcal{P} - \mathcal{E}) \tag{2.2.20}$$

all the terms on the LHS of the time discretized equations are for time level $n+1$ so the implicit backward time-stepping scheme is in use. The terms on the RHS are time-explicit. Set

$$u^* = u^n + \Delta t G_u^{(n+1/2)}, \tag{2.2.21}$$

$$v^* = v^n + \Delta t G_v^{(n+1/2)}, \tag{2.2.22}$$

and

$$\eta^* = \epsilon_{fs}(\eta^n + \Delta t(\mathcal{P} - \mathcal{E})) - \Delta t(\partial_x H\widehat{u^*} + \partial_y H\widehat{v^*}). \tag{2.2.23}$$

Then,

$$\partial_x g H \partial_x \eta^{n+1} + \partial_y g H \partial_y \eta^{n+1} - \frac{\epsilon_{fs}\eta^{n+1}}{\Delta t^2} = -\frac{\eta^*}{\Delta t^2}, \tag{2.2.24}$$

and

$$u^{n+1} = u^* - \Delta t g \partial_x \eta^{n+1}, \tag{2.2.25}$$

$$v^{n+1} = v^* - \Delta t g \partial_y \eta^{n+1}. \tag{2.2.26}$$

Solving equations 2.2.21 to 2.2.26 in succession is the time-discretization method for the hydrostatic model with an implicit, linear free-surface.

The nonhydrostatic formulation includes the full vertical momentum equation that requires the solution to the 3D elliptical equations for nonhydrostatic pressure perturbation. To retrieve the hydrostatic pressure, we integrate vertically, and we solve a 2D elliptic equation to retrieve the surface pressure/elevation, this decreases the amount of work required to solve for the nonhydrostatic pressure. For the nonhydrostatic pressure, we discretize the momentum equations as followed

$$\frac{1}{\Delta t}u^{n+1} + g\partial_x\eta^{n+1} + \partial_x\phi_{nh}^{n+1} = \frac{1}{\Delta t}u^n + G_u^{(n+1/2)} \tag{2.2.27}$$

$$\frac{1}{\Delta t}v^{n+1} + g\partial_y\eta^{n+1} + \partial_y\phi_{nh}^{n+1} = \frac{1}{\Delta t}v^n + G_v^{(n+1/2)} \tag{2.2.28}$$

$$\frac{1}{\Delta t}w^{n+1} + \partial_z\phi_{nh}^{n+1} = \frac{1}{\Delta t}w^n + G_w^{(n+1/2)}. \tag{2.2.29}$$

The discretized momentum equations must satisfy the time-discretized continuity (equation 2.2.20) and the local continuity equation

$$\partial_x u^{n+1} + \partial_y v^{n+1} + \partial_z w^{n+1} = 0. \tag{2.2.30}$$

The explicit predictions for the horizontal momentum equations are the same in the hydrostatic and nonhydrostatic methods. The explicit prediction for the vertical momentum equation is similar to the horizontal equations

$$w^* = w^n + \Delta t G_w^{(n+1/2)}. \tag{2.2.31}$$

This algorithm splits the tendency of the flow such that

$$u^{n+1} = u^{**} - \Delta t\partial_x\phi_{nh}^{n+1} \tag{2.2.32}$$

$$v^{n+1} = v^{**} - \Delta t\partial_y\phi_{nh}^{n+1} \tag{2.2.33}$$

where

$$u^{**} = u^* - \Delta t g \partial_x \eta^{n+1} \tag{2.2.34}$$
$$v^{**} = v^* - \Delta t g \partial_y \eta^{n+1}. \tag{2.2.35}$$

We substitute the above equations into the depth integrated continuity equation (equation 2.2.20) to get

$$\partial_x H \partial_x \left(g\eta^{n+1} + \widehat{\phi}_{nh}^{n+1} \right) + \partial_y H \partial_y \left(g\eta^{n+1} + \widehat{\phi}_{nh}^{n+1} \right) - \frac{\epsilon_{fs}\eta^{n+1}}{\Delta t^2} = -\frac{\eta^*}{\Delta t^2} \tag{2.2.36}$$

this equation is approximated by equation 2.2.24 since we do not yet know what ϕ_{nh}^{n+1} and $\nabla\widehat{\phi}_{nh} \ll g\nabla\eta$. If equation 2.2.24 is accurately solved then $\widehat{\phi}_{nh} \approx 0$ and the barotropic motion is not driven by the hydrostatic pressure field. Since the flow must also satisfy the local continuity equation (equation 2.2.30) we find the 3-dimensional elliptic equations for ϕ_{nh}^{n+1}

$$\partial_{xx}\phi_{nh}^{n+1} + \partial_{yy}\phi_{nh}^{n+1} + \partial_{zz}\phi_{nh}^{n+1} = \partial_x u^{**} + \partial_y v^{**} + \partial_z w^*, \tag{2.2.37}$$

where

$$\partial_z w^{n+1} = -\partial_x u^{n+1} - \partial_y v^{n+1} \tag{2.2.38}$$

which we solve for by vertically integrating for w^{n+1}.

When describing the time-stepping methods above we did not describe the explicit terms. The method used for all explicit terms in both the momentum and tracer equations in this thesis use the MITgcm default quasi-second order Adams-Bashforth method. The formula used for the quasi-second order Adams-Bashforth scheme is

$$G_\tau^{(n+1/2)} = (3/2 + \epsilon_{AB})G_\tau^n - (1/2 + \epsilon_{AB})G_\tau^{n-1} \tag{2.2.39}$$

Extrapolating to mid-point in time ($t = (n + 1/2)\Delta t$) implies that $\epsilon_{AB} = 0$ and it would be second order accurate, but this is weakly unstable for oscillatory terms (see the Discretization and Algorithm section of the MITgcm documentation). Therefore, we choose a small value to give ϵ_{AB}.

2.3 External Forcing Package

The first package that we will be discussing is the external forcing (EXF) package. For the purpose of this thesis, the EXF package reads in fields such as air temperature, downward shortwave and longwave radiation, and wind speeds. Then, it uses bulk formulae to transform atmospheric fields to surface fluxes, and then outputs diagnostic fields.

There are several output diagnostics offered by this package. The outputs that we are concerned about in this thesis include: sensible heat flux into the lake, latent heat flux into the lake, net upward surface heat flux, net upward shortwave radiation, and net upward longwave radiation. The EXF package calculates the fluxes by adapting the bulk formulae given in the NCOM (Navy Coastal Ocean Model) model which follows Large and Pond [1981] and Large and Pond [1982]. Note that the bulk formulae presented here are not applicable when ice is present, however this package can be used in conjunction with the sea ice package, which will be discussed in a later section.

We will show here the formulas used in the EXF package to calculate the output diagnostics. The sensible heat flux into the lake is calculated such that

$$Q_{SH} = c_{atm}\tau t^* \tag{2.3.1}$$

where: c_{atm} is the mean atmospheric specific heat which is set to be 1005 J kg^{-1} K^{-1}; $\tau = \rho_{air}U_{air}C_d$ is the surface stress with air density ρ_{air}, wind speed U_{air} at 10 m, and drag coefficient C_d; and t^* is the turbulent temperature scale. The package calculates latent heat flux into the lake as

$$Q_{LH} = \Lambda_v \tau q^* \tag{2.3.2}$$

where: Λ_v is the latent heat of evaporation set to be 2,500,000 J kg^{-1}; and q^* is the turbulent humidity scale. The net upward shortwave radiation is calculated as

$$Q_{SW\uparrow} = -Q_{SW\downarrow}(1 - \text{ice and snow absorption} - \alpha) \tag{2.3.3}$$

where: $Q_{SW\downarrow}$ is the downward shortwave radiation; and α is the surface albedo. Note that the open-water albedo is always 0.1 in the MITgcm. Similarly, the net upward longwave radiation is calculated by

$$Q_{LW\uparrow} = -(Q_{LW\downarrow} - \text{ice and snow absorption} - \epsilon\sigma_B T_0^4) \tag{2.3.4}$$

where: $Q_{LW\downarrow}$ is the downward longwave radiation; $\epsilon \approx 0.97$ is the surface emissivity; $\sigma_B = 5.67 \times 10^{-8}$ W m^{-2} K^{-4} is the Stefan-Boltzmann constant; and T_0 is the surface temperature. We will go more in depth into the ice and snow absorption in the sea ice package section. Finally, the package calculates the net upward surface heat flux as

$$Q_{flux} = Q_{SH} + Q_{LH} + Q_{SW\uparrow} + Q_{LW\uparrow}. \tag{2.3.5}$$

2.4 K-Profile Parameterization Package

Another package available for the MITgcm is the nonlocal KPP (K-Profile Parameterization) package. This package is based off of the vertical mixing scheme first discussed in Large et al. [1994]. The surface boundary layer of large lakes deals with heat and momentum fluxes between the atmosphere, cryosphere, and the interior of the lake. Then, to get a more accurate model output, we must find a way to model the turbulence and vertical mixing occurring in the surface boundary layer. The KPP vertical mixing scheme is one scheme available for modelling this vertical mixing and turbulence [Van Roekel et al., 2018].

The KPP scheme assumes that vertical fluxes dominate the turbulent mixing in the surface boundary layer [Van Roekel et al., 2018]. The surface boundary layer is also known as the mixed layer. According to the KPP section of the MITgcm documentation, the KPP package assumes that interior mixing is governed by a constant internal wave activity and shear instability calculated as a function of the local gradient Richardson number. It calculates the depth of the boundary layer at each grid point. The boundary layer depth is reliant on a critical number of turbulent processes that are parameterized by a bulk Richardson number. The mixing in the surface boundary layer is highly dependent on surface forcing, the KPP accounts for this by a polynomial profile. The boundary layer profile is asymptotically matched to the interior water. This fixes the coefficients of the previously mentioned polynomial and it enables a portion of the mixing in the surface boundary layer to also affect the interior of the lake and vice versa. Finally, when the water column is unstable, a non-local term that is independent of the vertical gradient of properties improves the mixing. See figure 2.2 for a visualization of the the KPP mixing scheme.

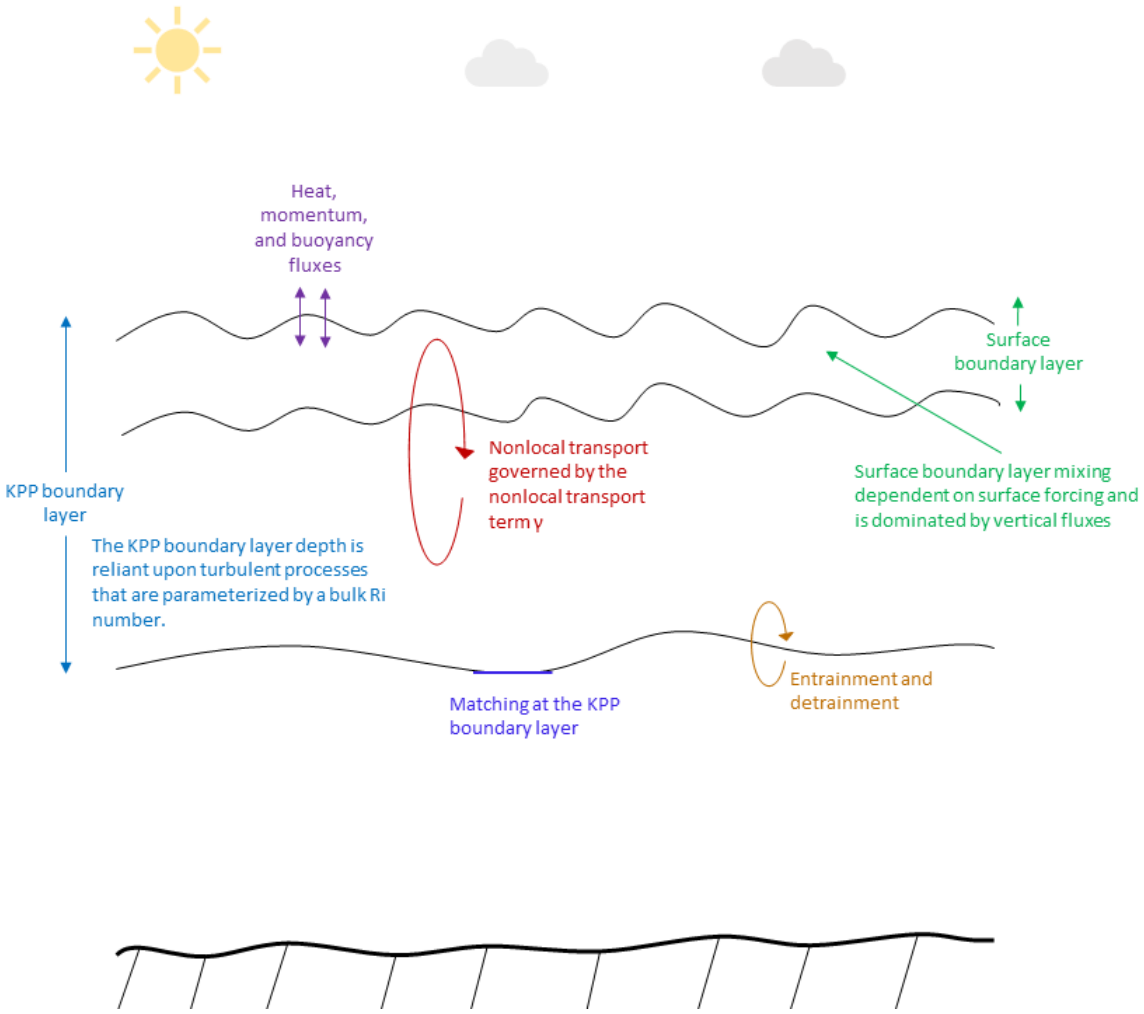

Figure 2.2: The processes that takes place in the surface boundary layer and the KPP boundary layer when using the the KPP vertical mixing scheme in the MITgcm. This figure was inspired by figure 1 in Van Roekel et al. [2018].

The KPP package calculates the surface boundary layer depth. It does this at the shallowest depth in which the bulk Richardson number is equivalent to the critical number which is set to 0.3. The model determines the Bulk Richardson numbers by finding velocity and buoyancy differences between the surface and grid levels below the surface

$$Ri_b = \frac{(b_{sl} - b(z))(-z + \eta)}{|\mathbf{u_{hsl}} - \mathbf{u_h}(\mathbf{z})|^2 + V_t^2(z)}$$

where b is the buoyancy and b_{sl} is the averaged buoyancy over the depth of the surface boundary layer; $\mathbf{u_h}$ is the horizontal velocity field and $\mathbf{u_{hsl}}$ is the horizontal velocity field averaged over the surface boundary layer; and V_t^2 is the parameterized turbulent vertical shear. Small/large buoyancy differences imply weak/strong vertical stratification. Small buoyancy differences are typical within the surface boundary layer and large buoyancy differences are typical of regions below the boundary layer. When the bulk Richardson number at grid level k becomes greater than the critical value, the surface boundary layer depth is linearly interpolated between that grid level and the grid level directly underneath it [Van Roekel et al., 2018]. The KPP package calculates the depth of the surface boundary layer at every grid point.

The KPP scheme uses a shape function to account for vertical variations in the surface boundary layer (see the green text in figure 2.2). It also uses a nonlocal transport term to communicate vertical turbulent fluxes between the interior and surface boundary layer (see the red text in figure 2.2).

In the KPP package, the vertical fluxes $\overline{w\xi}$ of momentum have the following relation at depth d

$$\overline{w\xi}(d) = -K_\xi \left(\frac{\partial \xi}{\partial z} - \gamma_\xi \right) \tag{2.4.1}$$

where ξ are the tracer properties that are made up of a gradient-flux term $\frac{\partial \xi}{\partial z}$, and a non-local term γ_ξ which improves the gradient-flux mixing coefficient K_ξ.

The KPP scheme in the model defines the boundary layer mixing profile to be

$$K_\xi(\sigma) = h w_\xi(\sigma) G(\sigma)$$

where h is the surface boundary layer depth, $w_\xi(\sigma)$ is a turbulent velocity scale that is depth-dependent, and $G(\sigma)$ is a non-dimensional shape function. Here, $\sigma = d/h$ is a dimensionless vertical coordinate. The vertical non-dimensional shape function $G(\sigma)$ determines the vertical structure of diffusivity and the non-local flux in equation 2.4.1. The shape function follows a third order polynomial. More information on how the shape function is constructed can be found in appendix B1 in Van Roekel et al. [2018] or Large et al. [1994].

The nonlocal transport term γ takes on the following values

$$\gamma_\xi = 0 \qquad \zeta \geq 0$$

$$\left.\begin{aligned} \gamma_m &= 0 \\ \gamma_s &= C_s \frac{\overline{ws_0}}{w_s(\sigma)h} \\ \gamma_\theta &= C_s \frac{\overline{w\theta_0}+\overline{w\theta_R}}{w_s(\sigma)h} \end{aligned}\right\} \quad \zeta < 0$$

where $\zeta = d/L$ is the stability parameter with Monin-Obukhov length scale L and C_s is a constant. The nonlocal transport term is only nonzero for unstable convective forcing conditions.

Basically, the KPP package performs the following sequence: first, it calculates the velocity scale at the surface boundary layer depth; then, it computes the viscosities in the lake interior and the derivatives at the surface boundary layer; then it finds the turbulent velocity scales at the interface; then it determines the dimensionless shape function at the interfaces; next, it calculates the boundary layer diffusivities at the interfaces; then is computes the nonlocal transport term; and finally it gets the diffusivities at the grid level below the surface boundary layer [Van Roekel et al., 2018].

2.5 SEAICE Package

The SEAICE package in the MITgcm allows for a dynamic and thermodynamic method to model sea ice. Rates of freezing are dependent on ice thickness and the open water fraction. Additionally, the transportation of ice is dependent on ice thickness and the open water fraction, which regulates how much stress the ice transfers. This is why using a coupled dynamic thermodynamic model is important; they allow transfer of both heat and momentum [Hibler III, 1979]. There are several different options given by this package that the user can choose to apply or not such as thermodynamics. There are also several aspects of the package that can be modified such as the rheology solver.

The SEAICE package is based on a version of the viscous-plastic dynamic-thermodynamic sea ice model from Zhang and Hibler III [1997] that first appeared in Hibler III [1979] and Hibler [1980]. Many aspects of this code have been modified for the SEAICE package [Losch et al., 2010]. For the present study, the sea ice model is coupled with the hydrodynamic solver of the MITgcm.

Here, we consider lake ice to be a continuum and, therefore, basic rheology models such as the viscous-plastic (VP) and Elastic-Viscoplastic Model (EVP) models are suitable for use [Leppäranta, 2015]. For the simulations shown in this thesis, we used the VP model and the Line Successive Over-Relaxation (LSOR) solver with free-drift, and so these are the processes that we go in-depth with in this section. Information on the EVP model and all of its modifications, along with the Jacobian-free Newton-Krylov (JFNK) rheology solver can be found in the SEAICE section of the MITgcm documentation.

The VP model, as is first discussed in Hibler III [1979], was born out of a desire for an ice model where the rheology and thickness of ice would depend on internal stresses placed on the ice cover. The VP model includes a constitutive law that describes the relationship of the ice stress with the strain rate and the ice strength; the constitutive law is probably the most important component of the VP model. Also found in the VP model is a simple ice thickness distribution which includes the fractional area of open water and total ice mass. Finally, the original VP model found in Hibler III [1979] includes ice strength which is calculated using ice thickness and the fraction of open water. In VP models, the ice is taken to be a nonlinear viscous compressible fluid.

The momentum equation used in the MITgcm ice model is

$$m\frac{D\mathbf{u}}{Dt} = -mf\mathbf{k}\times\mathbf{u} + \tau_{\text{air}} + \tau_{\text{ocean}} - m\nabla\phi(0) + \mathbf{F}, \tag{2.5.1}$$

where $m = m_i + m_s$ is the ice and snow mass per unit area; $\mathbf{u} = u\hat{i} + v\hat{j}$ is the ice velocity vector; τ_{air} and τ_{ocean} are the wind-ice and ocean-ice stresses, respectively; $\nabla\phi(0)$ is the tilt (or gradient) of the surface height; $\phi(0) = g\eta + p_a/\rho_{ref} + mg/\rho_{ref}$ is the surface height potential in response to ocean dynamics ($g\eta$), atmospheric pressure loading (p_a/ρ_{ref}, ρ_{ref} is a reference density of air), and a term due to ice and snow loading and $\mathbf{F} = \nabla\cdot\sigma$ is the divergence of the internal stress tensor σ_{ij}. This model does not account for the advection of ice. The wind stress is given by

$$\tau_{\text{air}} = \rho_{\text{air}}C_{\text{air}}|\mathbf{U}_{\text{air}} - \mathbf{u}|R_{\text{air}}(\mathbf{U}_{\text{air}} - \mathbf{u}),$$

and the ice-ocean stress is given by

$$\tau_{\text{ocean}} = \rho_{\text{ocean}}C_{\text{ocean}}|\mathbf{U}_{\text{ocean}} - \mathbf{u}|R_{\text{ocean}}(\mathbf{U}_{\text{ocean}} - \mathbf{u}),$$

where $\rho_{\text{air/ocean}}$ are reference densities of the atmosphere and ocean, respectively; $C_{\text{air/ocean}}$ are the atmosphere and ocean drag coefficients; $\mathbf{U}_{\text{air/ocean}}$ are the the surface winds of the

atmosphere and the surface currents of the ocean, respectively; and $R_{\text{air/ocean}}$ are rotation matrices that act on the wind and current.

As previously mentioned, the VP model includes a constitutive law that give the relationship between ice stress with ice strength and strain rate. The constitutive law that the ice package uses is as follows

$$\sigma_{ij} = 2\eta(\dot{\epsilon}_{ij}, P)\dot{\epsilon}_{ij} + [\zeta(\dot{\epsilon}_{ij}, P) - \eta(\dot{\epsilon}_{ij}, P)]\,\dot{\epsilon}_{kk}\delta_{ij} - \frac{P}{2}\delta_{ij}, \tag{2.5.2}$$

where the ice strain rate $\dot{\epsilon}_{ij}$ is given by:

$$\dot{\epsilon}_{ij} = \frac{1}{2}\left(\frac{\partial u_i}{\partial x_j} + \frac{\partial u_j}{\partial x_i}\right).$$

The maximum ice pressure is given by

$$P_{\max} = P^* c\, h\, \exp\{-C^* \cdot (1-c)\}, \tag{2.5.3}$$

where P^* is the ice strength, h is the ice thickness, c is the compactness (or concentration), and C^* is an ice parameter. The nonlinear bulk viscosity is given by:

$$\zeta = \min\left(\frac{P_{\max}}{2\max(\Delta, \Delta_{\min})}, \zeta_{\max}\right),$$

and the nonlinear shear viscosity is given by

$$\eta = \frac{\zeta}{e^2},$$

where

$$\Delta = \left[(\dot{\epsilon}_{11} + \dot{\epsilon}_{22})^2 + e^{-2}\left((\dot{\epsilon}_{11} - \dot{\epsilon}_{22})^2 + \dot{\epsilon}_{12}^2\right)\right]^{\frac{1}{2}}.$$

For numerical reasons, the bulk viscosities ζ are bounded below by a minimum value $\Delta_{\min} = 10^{-10}\ \text{s}^{-1}$ and a maximum $\zeta_{\max} = P_{\max}/(2\Delta^*)$ where $\Delta^* = 2 \times 10^{-9}\,\text{s}^{-1}$.

The momentum equation 2.5.1 can be discretized such that it takes on the form of a system of linear equations

$$\mathbf{A}(\mathbf{x})\,\mathbf{x} = \mathbf{b}(\mathbf{x}), \tag{2.5.4}$$

where $\mathbf{x}$ is a 2×1 solution vector with u and v as the components which hold the corresponding velocity variables at all grid points at one time level.

The MITgcm offers two options for the momentum solver in the SEAICE package: the LSOR, and the JFNK solvers. The default solver used in the model is a Picard iterative method, LSOR, which was first introduced by Zhang and Hibler III [1997]. This solver converges slowly, but after a user-defined amount of nonlinear steps will abort. The JFNK solver was presented in Lemieux et al. [2010] as an alternative to the slowly converging LSOR method. We will not go into detail about the JFNK solver in this thesis since this solver was not used for the present work.

Ice sheets are often broken up into floes that move around due to forcing, such as wind. This broken ice is known as drift ice. For a *free-drift* rheology (which this thesis uses), there is no stress, i.e. $\sigma = 0$. Free drift rheology is useful when the ice compactness is < 0.8, and there is low stress [Leppäranta, 2015].

The MITgcm uses a 2D ice model, and there is only 1 vertical layer in the ice model, as opposed to the user-defined amount of vertical layers found in the ocean model for the MITgcm. FLake also only has one ice layer [Semmler et al., 2012], however CLIMo has a user-defined number of vertical ice layers [Duguay et al., 2003]. The MITgcm follows the zero-layer model found in the appendix of Semtner [1976] for the thermodynamics of its sea ice model. This model considers three prognostic variables: snow thickness, ice thickness, and surface temperature. This model takes the heat capacity of ice to be zero and reduces the heat equation to a constant conductive heat flux. There is a linear temperature profile. Boundary conditions for the heat equations in this model are:

$$T|_{bottom} = T_{fr},$$

and

$$Q_{top} = K\frac{\partial T}{\partial z} = (K/h)(T_0 - T_{fr}),$$

where $T|_{bottom}$ is the temperature at the bottom of the ice, T_{fr} is the freezing temperature of the water, Q_{top} is the surface heat flux, $K = 2.1656$ W m^{-1} K^{-1} is the constant ice conductivity, h is the ice thickness, and $T_0 - T_{fr}$ is the difference between the surface temperature of the ice and the the freezing temperature of water (also, it is the temperature

of the bottom of the ice here). The ice model in the MITgcm calculates the surface heat flux similarly to Parkinson and Washington [1979] and Manabe et al. [1980]. The surface temperature equation (surface energy balance) is

$$\frac{K}{h}(T_0 - T_{fr}) = Q_{SW\downarrow}(1 - \text{albedo}) + \epsilon Q_{LW\downarrow} - Q_{LW\uparrow}(T_0) + Q_{LH}(T_0) + Q_{SH}(T_0), \quad (2.5.5)$$

where ϵ is the emissivity of the ice, $Q_{SW/LW\downarrow}$ is the downward shortwave and longwave radiation, $Q_{LW\uparrow} = \epsilon\sigma_B T_0^4$ is the emitted longwave radiation where $\sigma_B = 5.67 \times 10^{-8}$ W m^{-2} K^{-4} is the Stefan-Boltzman constant, and the units for temperature are in Kelvin. At T_0, the latent heat Q_{LH} and sensible heat Q_{SH} are defined as follows

$$Q_{LH} = \rho_{\text{air}} C_E (\Lambda_v + \Lambda_f) |\mathbf{U}_{\text{air}}| \left[q_{\text{air}} - q_{\text{sat}}(T_0)\right], \quad (2.5.6)$$

$$Q_{SH} = \rho_{\text{air}} c_p air C_E |\mathbf{U}_{\text{air}}| \left[T_{10\text{m}} - T_0\right], \quad (2.5.7)$$

where ρ_{air} is the air density. C_E is an ice-ocean transfer coefficient for sensible heat and latent heat, Λ_v and Λ_f are the latent heat of vaporization and fusion, respectively, $q_{air/sat}$ is the air and saturation humidity, respectively, $\mathbf{U}_{\text{air}}$ is the wind velocity, and $c_p air$ is the specific heat of air. Equation 2.5.5 is solved for T_0 using an iterative Ralphson-Newton method that typically converges in less than 10 iterations.

When computing the upward shortwave radiation, the model must take into consideration what the surface albedo value is. Basically, surface albedo determines the fraction of sunlight reflected back into the atmosphere. Excluding snow, the MITgcm considers three different albedo values: 0.75 (dry ice), 0.66 (wet ice), and 0.1 (open-water). If there is no ice, the model uses the open-water albedo value. Otherwise, the model determines which ice albedo value to use according to

$$\text{ice} = \begin{cases} \text{dry}, & T_w < T_{melt}, \\ \text{wet}, & T_w \geq T_{melt}. \end{cases}$$

where T_w is the surface temperature, and T_{melt} is the melting temperature of the lake. Figure 2.3 shows the albedo values given for the open-water, wet ice, and dry ice surfaces in the MITgcm. From this figure we can see that the open-water surface absorbs the most incoming solar energy and the dry ice surface reflects the most incoming solar energy.

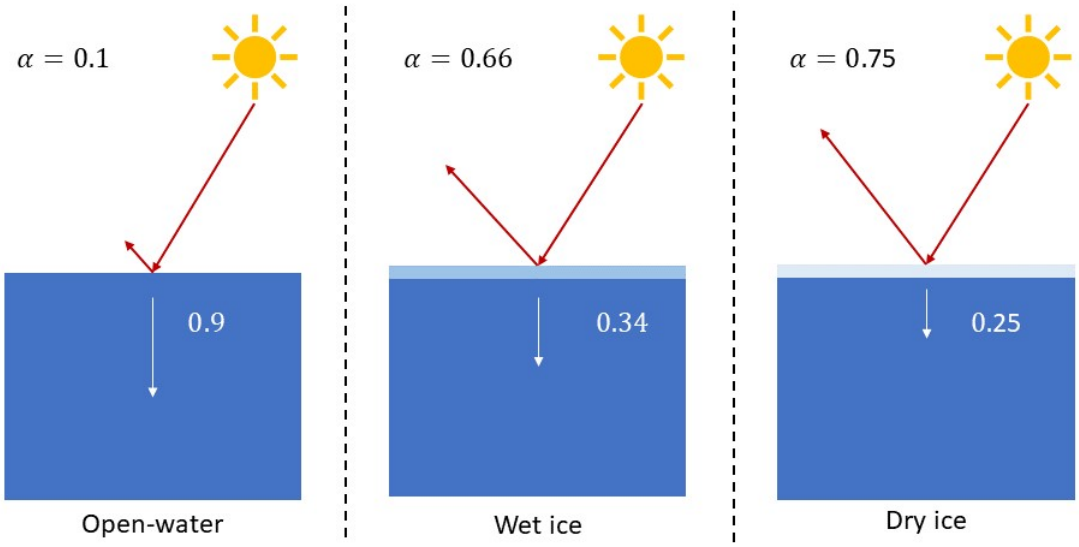

Figure 2.3: The surface albedo values for open-water, wet ice, and dry ice.

There is a high dependency between conductive heat flux and ice thickness in the zero-layer thermodynamics model. The ice thickness h in the ice model in the MITgcm represents a mean over a thickness distribution in any given surface cell with an ice cover. Realistically, each surface cell of the model may represent a large area and contain a lot of variation among ice thickness. For the model to compute the conductive heat flux through the ice, the model divides h into a user-specified number m of thickness categories H_n such that $H_n = \frac{2n-1}{m}h$ for $n = 1, ..., m$. The total heat flux is then calculated by computing the heat flux for each thickness category and taking the average over the area Losch et al. [2010]. The simulations examined in this thesis all use seven thickness categories as that is the default value suggested for the MITgcm.

Ice velocities advect the effective ice thickness $X = (c \cdot h)$ (units: meters), where c is concentration, by

$$\frac{\partial X}{\partial t} = -\nabla \cdot (\mathbf{u}\, X) + \Gamma_X + D_X \tag{2.5.8}$$

where Γ_X are the thermodynamic source terms and D_X are the diffusive quantities for the $X = (c \cdot h)$ and c quantities. There are several advection schemes offered for the model. The advection scheme recommended by the model's manual is any flux-limited schemes, as they maintain the sharp edges and slopes that are found in ice; these schemes also prevent the

model from outputting negative concentrations or ice thickness. The flux-limited schemes conserve volume, horizontal-area, and are unconditionally stable, this means that $D_X = 0$.

The SEAICE model in the MITgcm is similar to the CICE model when it comes to ice distribution and ridging. The two areas that the similarities occur are some participation and ridging functions, and the ice strength parameterization. For this thesis, the model ice thickness follows the ice thickness distribution function from Thorndike et al. [1975]. Our simulations are made using the ice strength given in equation 2.5.3.

Chapter 3

Ice Growth Simulations

3.1 Introduction to the Problem

The motivation of this thesis is to explore the vertical mixing of small-scale processes under wintertime conditions using the MITgcm. By studying these small simulations, we hope to detect any model-related issues before applying the MITgcm to larger-scale Lake Erie simulations. Mixing and convection in lakes are primarily due to wind forcing and incoming solar radiation. Before we begin adding wind and ice into our simulations, it is important that we are aware of any issues that may occur under a more simple parameterization.

The general setup for all the simulations ran in this chapter can be seen in figure 3.1. Essentially, we are considering a shallow rectangular lake of constant depth that is small in the horizontal scale. The lake has an area of 10,000 m^2 and a depth of 20 m with 100 evenly spaced grid cells in the x, y, and z directions. The horizontal resolution is 1 m and the vertical resolution is 0.2 m. The temperature profile of the lake is linearly stratified with a specified surface temperature and a temperature of 4°C (the density maximum) at the bottom. There is a 50% relative humidity, and there is no wind forcing. These simulations consider varying values for constant incoming downward shortwave and longwave radiation. The timestep the model used is 0.1 s, the background horizontal and vertical diffusion coefficients are 10^{-4} m^2/s, and the background horizontal and vertical viscosity coefficients are 7×10^{-4} m^2/s. The order of horizontal background viscosity and diffusion coefficients were chosen similarly to Padon and Ashkenazy [2018] and we chose to use the same values for the background vertical coordinates in this thesis. All of the simulations in this chapter were carried out using the nonhydrostatic version of the MITgcm.

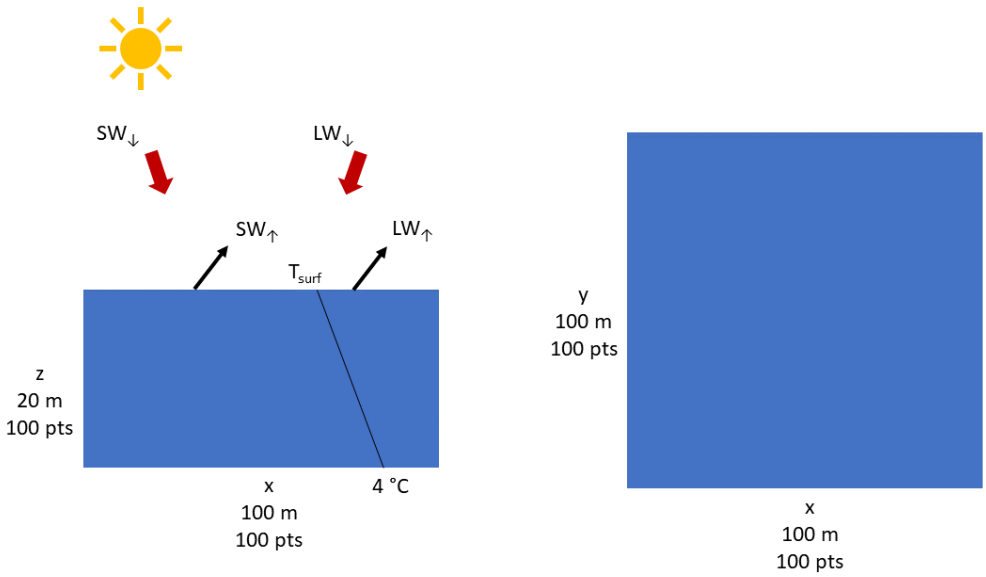

Figure 3.1: The general setup for cases A1, A2, A3, and A4. On the left is the side view of the toy lake and on the right is the view from above.

In this chapter we will be studying four simulations. The specific parameterizations for each simulation can be found in table 3.1. The parameters being varied in this chapter are the downward shortwave and longwave radiation, the surface temperature, and the air temperature. Note that we choose the downward shortwave and longwave radiation values such that they are always equivalent in this chapter. For example, if table 3.1 states that the downward radiation is 150 W/m^2, then that implies the downward shortwave radiation is 150 W/m^2 and the downward longwave radiation is also 150 W/m^2. More realistic values for average wintertime incoming radiation over Lake Erie would be approximately 100 W/m^2 downward shortwave radiation and approximately 300 W/m^2 downward longwave radiation.

Table 3.1: The specific parameter settings for all simulations shown in this chapter.

Case	Downward Radiation (W/m^2)	Surface Temperature (°C)	Air Temperature (°C)
A1	150	-0.03	1
A2	150	1	5
A3	300	1	5
A4	300	-0.03	1

3.2 Results

We begin the results section with case A1. This simulation has a downward shortwave and longwave radiation of 150 W/m^2, a -0.03°C surface temperature, and a 1°C air temperature. Figure 3.2 shows how the surface temperature and the ice thickness evolved over the 1.5 day simulation for case A1 at 0 minutes, 1125 minutes (18 hours and 45 minutes), and 2160 minutes (36 hours). The surface temperature of case A1 warms from -0.03° (the freezing temperature) to approximately 0.66°C. We notice that ice also thickens in case A1 to be about 2.4 cm thick. This implies that, under the current parameterizations, even though the model output states that the surface is warming above the freezing temperature, it is still growing ice. Note that there is no spatial variability in surface temperature and ice thickness for case A1. Refer to figure 3.2 for a visualization of the surface temperature and ice thickness evolution for case A1 at the beginning, middle, and end of the 1.5 day simulation.

Table 3.2: The values for average surface temperature and ice thickness at 0 minutes, 1125 minutes, and 2160 minutes for cases A1, A2, A3, and A4.

Time (min)	Average Surface Temp (°C)				Average Ice Thickness (m)			
	A1	**A2**	**A3**	**A4**	**A1**	**A2**	**A3**	**A4**
0	-0.03	1	1	-0.03	0	0	0	0
1125	0.5646	0.8052	2.0503	1.2188	0.0148	7.0307×10^{-10}	0	0
2160	0.6565	0.789	2.4984	1.7532	0.024	1.5279×10^{-9}	0	0

Figure 3.3 shows the average surface temperature (a) and the average ice thickness (b) over the entire 1.5 day simulation. The average computations were carried out by adding up all the upper, non-boundary cells and dividing the sum by the total number of non-boundary cells. The reason that boundary cells were not considered for these calculations

is that each model output field takes on a value of zero at the boundary due to our closed boundary conditions. We observe from figure 3.3a that the surface temperature begins to heat up quickly, but slows considerably after the first quarter of the total simulation time. Figure 3.3b shows that the ice thickness appears to increase in a much more linear pattern, however it also increases somewhat faster at the beginning of the simulation.

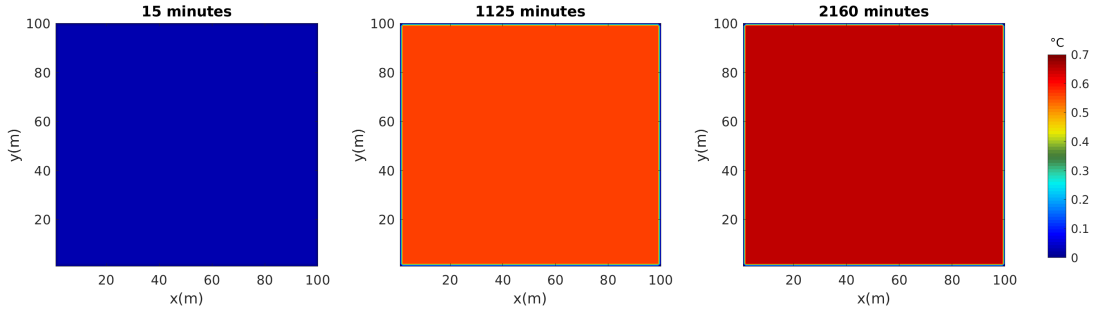

(a)

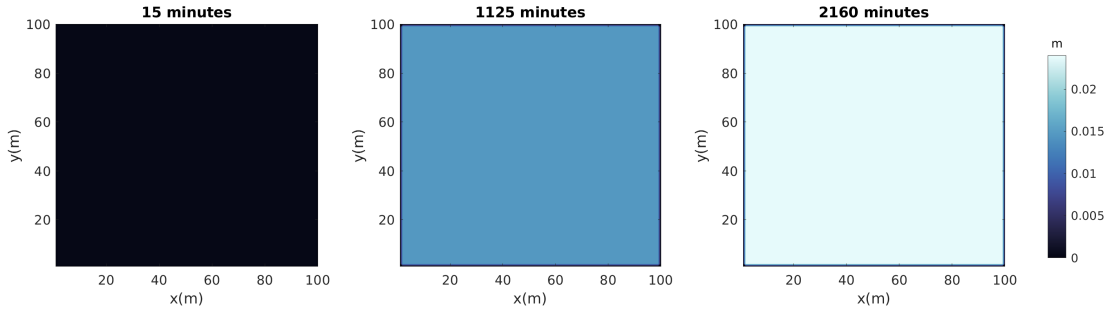

(b)

Figure 3.2: The evolution of the surface temperature (a) and the ice thickness (b) for case A1 given at 15 minutes, 1125 minutes (18 hours and 45 minutes), and 2160 minutes (36 hours). Colormap used in (b) from Thyng et al. [2016].

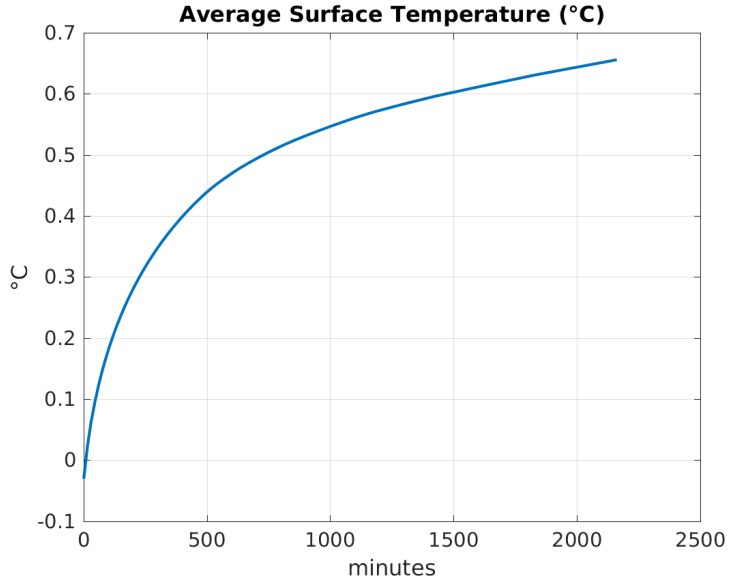

(a)

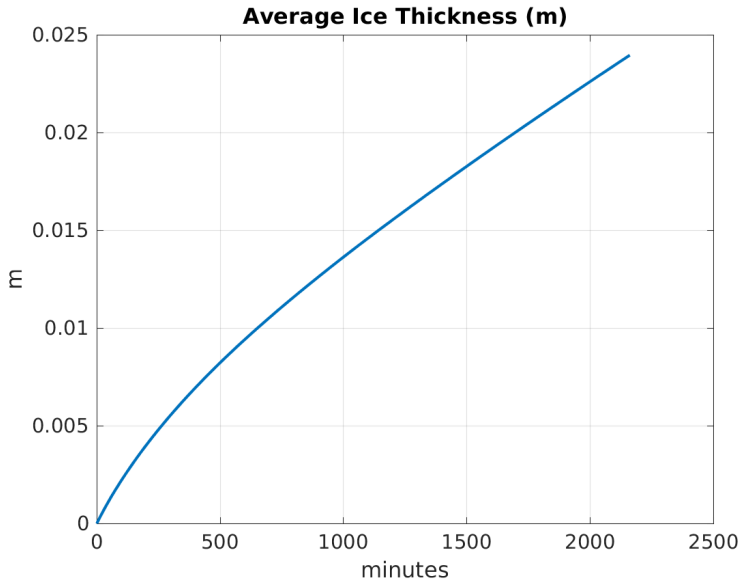

(b)

Figure 3.3: The average surface temperature (a) and the average ice thickness (b) of case A1 for the entire 1.5 day simulation.

Note that case A1 should not be growing ice since the surface temperature is warming above the freezing temperature. The next three simulations we explore in this chapter were carried out in an attempt to gain some clarity with respect to why the the MITgcm is growing ice for case A1, and to establish if we can determine some sort of threshold for when ice will begin growing. Figure 3.4 shows the average surface temperature and average ice thickness for all four cases examined in this chapter over the simulation period. Looking at figure 3.4a, we can see that all the cases are warming up except for case A2 (red line). Case A2 has a 150 W/m^2 downward shortwave and longwave radiation (as in case A1), and a 1°C surface temperature with a 5°C air temperature (different than case A1). Cases A1 and A2 have the same downward radiation, and figure 3.4a shows those two cases possibly approaching a similar horizontal asymptote near 0.7°C. The curves for cases A3 and A4 in figure 3.4a take on a very similar shape, case A3 is just shifted by approximately 1°C. Cases A3 and A4 have different air and surface temperatures, but their downward radiation values are equivalent.

Cases A3 and A4 begin the simulation with surface temperatures 1°C apart, and after 1.5 days of model time there is only a surface temperature difference of approximately 0.8°C (refer to table 3.2), after another 1.5 days this difference in surface temperature decreases further to 0.6°C (not shown here). It is reasonable to hypothesize that, if left to run for a longer period of time, cases A3 and A4 would reach a similar surface temperature. This conclusion is derived from the surface heat balance (see equation 2.5.5). Since there is no ice in these simulations, the open-water albedo is constant at 0.1 for both case A3 and A4. The downward shortwave and longwave radiation is also constant at 300 W/m^2 for both cases. From figure 3.6, we see that there is no latent or sensible heat flux for any of the cases discussed in this chapter. So then, the only term that could cause discrepancies in the surface temperature for cases A3 and A4 is the outgoing longwave radiation, which is relatively similar in cases A3 and A4 according to figure 3.6.

Figure 3.4b displays the average ice thickness for cases A1-A4. The ice thickness increases by the largest amount in case A1, however note that case A2 also grows some ice. Case A2 grows ice up to the order of 10^{-9} m in thickness by the end of the 1.5 day simulation (refer to table 3.2 for exact values). Cases A3 and A4 grow no ice. These results imply that, when incoming radiation is strong enough, the MITgcm will not grow ice even when the SEAICE model is in use. Even though case A2 grew ice, it was an ice thickness on an order so small that one may consider it just noise. Next, we will take a look at some of the heat flux results to aid in determining whether the small amount of ice found in case A2 may be considered insignificant for our purposes.

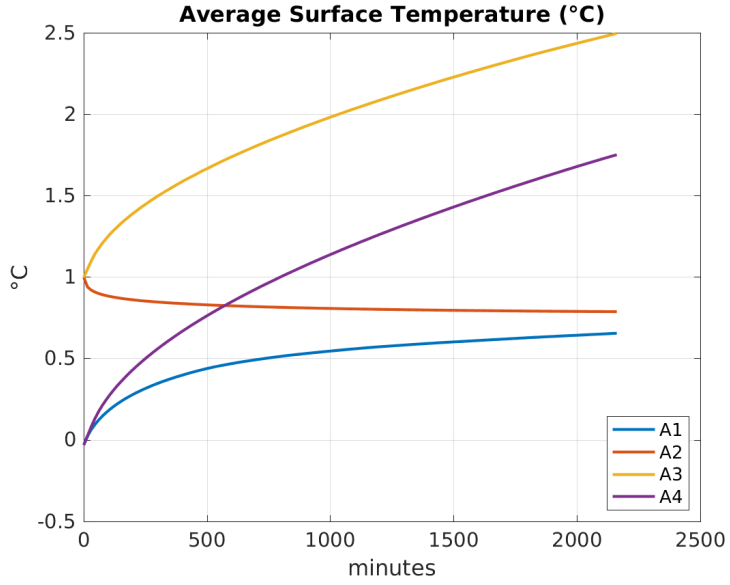

(a)

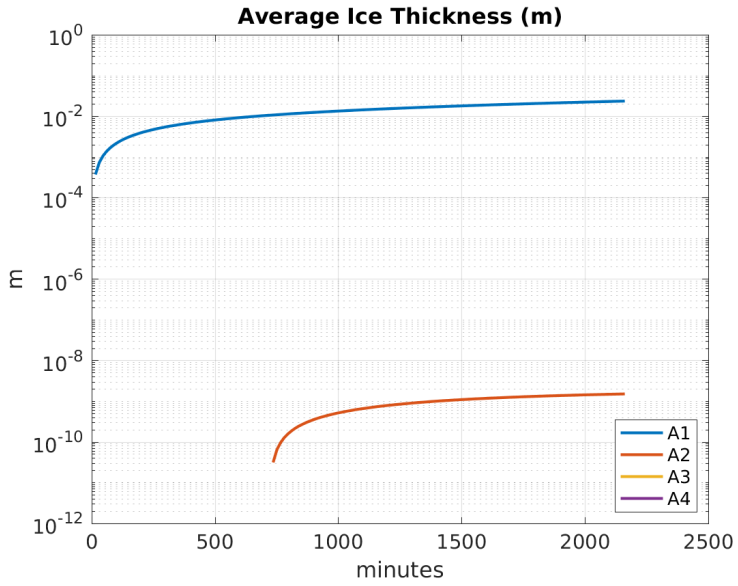

(b)

Figure 3.4: The average surface temperature (a) and the average ice thickness (b) for cases A1, A2, A3, and A4 over the entire 1.5 day simulation. Note that we are using the log scale for the y-axis in (b). Cases A3 and A4 are not visible in (b) since they have no ice appearing.

Figure 3.6 shows the net upward heat flux, net upward surface shortwave radiation, net upward longwave radiation, latent heat flux, and sensible heat flux for cases A1-A4 over the duration of the 1.5 day simulation. Recall that the latent and sensible heat fluxes are calculated as in equations 2.5.6 and 2.5.7, respectively. Then, it is expected that the latent and sensible heat is 0 W/m^2 for all cases in this chapter throughout the entire simulation since there is no wind.

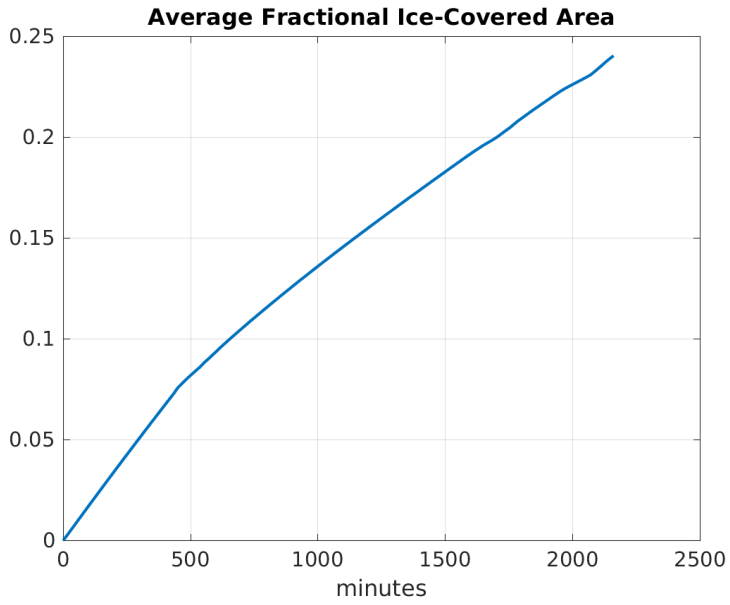

Figure 3.5: The average fractional ice-covered area (units are nondimensional) for case A1 over the entire 1.5 day simulation.

The equation the model uses to calculate the net upward surface shortwave radiation is equation 2.3.3 (recall that, since we are using zero-layer thermodynamics, there is no storage of heat in the ice or snow). The curves for cases A3 and A4 overlap in the plot for surface shortwave radiation because both of these cases have the same amount of incoming shortwave and longwave radiation, and both of these cases do not grow any ice. The net upward surface shortwave radiation for case A2 is also constant at -135 W/m^2. These results for case A2 indicates that, even though a very small amount of ice grows, it is not significant enough to influence the heat flux calculations. Interestingly, the net upward surface shortwave radiation for case A1 is steadily increasing. Physically, it makes sense for the upward shortwave radiation to steadily decrease in magnitude as the ice increases in thickness, however recall that the MITgcm only has two ice albedo values it uses (0.75

for dry ice and 0.66 for wet ice). Note that we find this result here inconsistent with the MITgcm SEAICE package documentation[1], for which the albedo is not a function of ice thickness. However, we also note that the average fractional ice-covered area is not equal to one at any point during this simulation (see figure 3.5). If we take r to be the fractional ice-cover, then the average surface albedo would be $\alpha_{avg} = r\alpha_{ice} + (1 - r)\alpha_{water}$. The average surface albedo will be further complicated as a result of the two options for ice albedo considered in the MITgcm (dry ice and wet ice). Referring to figure 3.5, we notice that values for the average fractional ice-covered area are increasing somewhat steadily, this may account for the steadily increasing net upward surface shortwave radiation we see in figure 3.6 for case A1, however more work should be done to confirm this.

Equation 2.3.4 is used to calculate the net upward longwave radiation. Figure 3.6 shows that the curves for cases A3 and A4 for the net upward longwave radiation are very similar, but the upward flux is slightly larger for case A3. This result make sense given that case A3 has a surface temperature that is approximately 1°C warmer than case A4. The curves for cases A1 and A2 for the net upward longwave radiation begin slightly different due to the small initial surface temperature difference, however the upward longwave flux becomes much more similar for the two cases as they approach the same surface temperature.

Finally, the net upward heat flux is computed by following equation 2.3.5. Figure 3.6 shows that cases A2, A3, and A4 all take on nearly constant values for the net upward heat flux due to their lack of ice coverage. Case A1 however, increases as the ice thickness increases. Notice that the results of the net upward heat fluxes are implying that the lakes in cases A3 and A4 are gaining heat, but the lakes in cases A1 and A2 are losing heat and cooling down. The fact that case A1 is losing heat may be related to why ice is appearing. The lake is cooling down, so ice begins to form. However, as ice begins forming heat must be released, this released heat may be warming the surface temperature. Case A2 is also cooling down, however the surface temperature is initialized above freezing in this case.

[1] https://mitgcm.readthedocs.io/en/latest/phys_pkgs/seaice.html

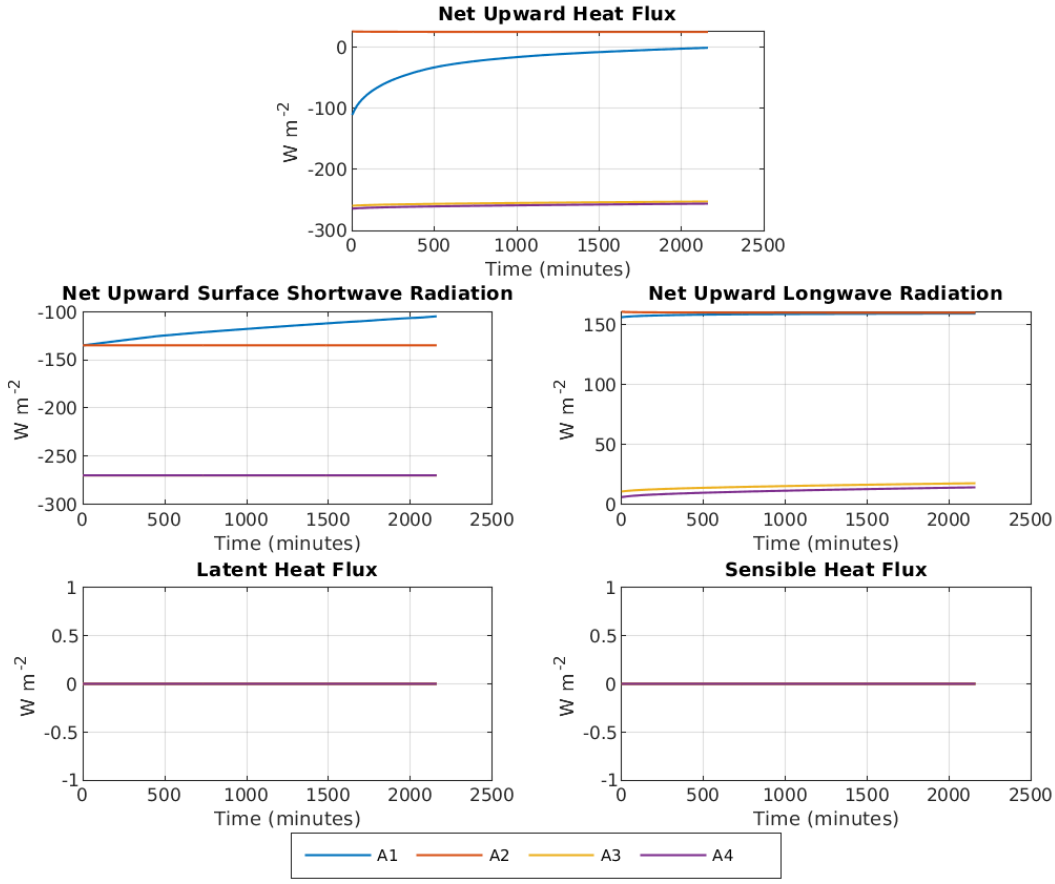

Figure 3.6: The average net upward heat flux, net upward surface shortwave radiation, net upward longwave radiation, latent heat flux, and sensible heat flux for all the simulations performed in this chapter over 1.5 days. The curves for cases A3 and A4 are overlapping in the net upward surface shortwave radiation plot. All curves are overlapping in the plots for latent and sensible heat flux.

Note that if we add a small amount of wind to case A1, the amount of ice that appears is significantly hampered in terms of thickness. We added a 10^{-16} m/s wind in the positive x-direction to case A1, and the ice only reached a maximum thickness on the order of 10^{-8} m. This, in turn caused the net upward shortwave radiation to remain constant at -135 W m^{-2} since the amount of ice thickness was not significant enough to influence the computation.

3.3 Concluding Remarks

The issue that inspired this chapter was that case A1 was producing an ice cover regardless of the fact that the surface was warming well above the freezing temperature. So, we ran three other cases varying downward shortwave and longwave radiation, air temperature, and surface temperature with the intention of learning why the ice was appearing in case A1, and also if we could stop the ice from emerging. Results showed that cases A3 and A4 did not produce any ice. Case A2 did show a very small amount of ice, however the model disregarded it when performing heat flux calculations. Since the heat flux computations were not affected, we may consider the small amount of ice grown as insignificant noise. We also tried adding a 10^{-16} m/s wind in the positive x-direction to the setup of case A1. Results from this test are not shown in this thesis, however the addition of wind reduced the amount ice thickness appearing in this case to such a small amount that the heat flux computations negated it and treated the lake as if there was no ice cover.

An inconsistency found in our simulation results compared to the documentation is the fact that the net upward surface shortwave radiation for case A1 is increasing at each output. According to the documentation, ice albedo is not a function of ice thickness and therefore, the curve for the surface shortwave radiation for case A1 should not look as it does in figure 3.6. It is a possibility that the steadily increasing average net upward surface shortwave radiation in case A1 is due to the steadily increasing average fractional ice-covered area in case A1, however more work should be done to confirm.

It is unclear why the model is producing a significant ice cover in case A1. According to figure 3.6, the lake is losing heat even though the surface temperature is increasing well above freezing. Perhaps it is due to the fact that the surface temperature is initialized to freezing temperature. The incoming radiation appears to be an important factor in determining whether the lake is warming or cooling, so maybe the magnitude of incoming radiation specified for cases A1 was simply not high enough. Case A2 had an equivalent amount of incoming radiation as case A1, however the air temperature and surface temperature were increased from case A2 acting as enough of a barrier to keep the lake from forming a significant ice cover. The ice growth appearing in case A1 may also be due to the fact that the lake is losing heat which results in ice appearing, however when the ice appears it has to release heat and this may be causing the surface to warm.

Chapter 4

Wind Simulations

4.1 Introduction to the Problem

Since the goal of this thesis is to monitor how the MITgcm handles vertical mixing of small-scale processes under wintertime conditions, we will begin adding wind and an ice cover to our simulations. The general setup for all simulations carried out in this chapter can be seen in figure 4.1. The basic setup in this chapter is very similar to the setup used in chapter three given by figure 3.1 except that in this chapter we consider and alter a few more parameters.

Parameter values for the simulations carried out in this chapter can be viewed in table 4.1. Note that each of the cases B1-B7 include a uniformly 1 m thick ice cover over approximately half the lake (the shape of the ice cover is given in the right half of figure 4.1). The surface temperature is always $-0.03°C$ (the freezing temperature), the air temperature is always $1°C$, and the downward shortwave and longwave radiation is always 150 W/m^2. The parameter settings that are varied include wind forcing, rotation, horizontal lake size and resolution, and whether or not the model uses the hydrostatic approximation or its fully nonhydrostatic capabilities. Note that all of simulations discussed in this thesis were executed using 100 processors. On average, using the Compute Canada machine, Graham[1], nonhydrostatic simulations take approximately 36 hours to complete, and hydrostatic simulations take approximately 10 hours to complete.

[1] https://docs.computecanada.ca/wiki/Graham

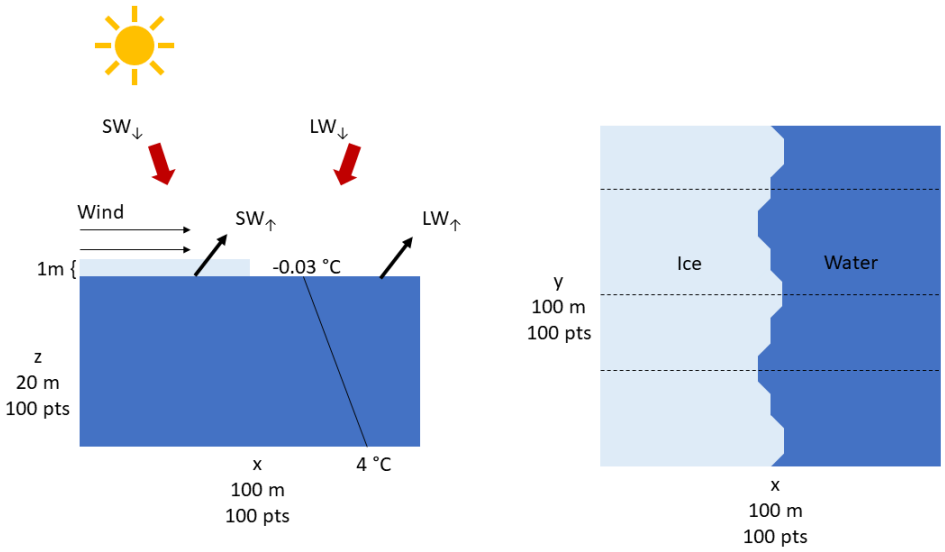

Figure 4.1: Schematic diagram showing the setup for the simulations found in chapter four. The side view of the lake can been seen on the left side, and the top-down view of the lake can be seen on the right. Displayed here is the partial ice cover, the downward (and upward) shortwave and longwave radiation, wind forcing, lake temperature profile, and lake size. The black dashed lines on the right are a reference for the locations of the y-slices shown in figures 4.5 and 4.6.

Table 4.1: Specific parameter settings that are varied for the simulations shown in chapter four.

Case	**Hydro/Nonhydro**	**Wind x-direc (m/s)**	**Horizontal Resolution (m)**	**Horizontal Domain Size (m)**	**Rotation**
B1	Nonhydro	0	1	100×100	Yes
B2	Nonhydro	3	1	100×100	Yes
B3	Hydro	3	1	100×100	Yes
B4	Nonhydro	3	10	1,000×1,000	Yes
B5	Nonhydro	3	10	1,000×1,000	No
B6	Nonhydro	3	100	10,000×10,000	Yes
B7	Nonhydro	6	1	100×100	Yes

4.2 Ice Movement Problem

The first thing we will discuss about the simulations in this chapter is a problem that we came across when adding wind forcing. There are three ice momentum solvers that the MITgcm may use that have been tested for this thesis. See section 2.5 for information regarding each of the momentum solvers. Originally, we were running all of our simulations using the EVP momentum solver. However, the EVP solver did not allow for much ice movement, even with strong wind forcing. When using the EVP momentum solver, only a very small amount of ice would detach from the edge of the larger ice mass and move across the lake. This is a strange result since the EVP momentum solver is often used in the sea ice community, so it is possible that our issues may be related to an incorrect set up. Next, we tried using the LSOR momentum solver without free-drift. This momentum solver did not allow for any ice movement. Finally, we attempted using the LSOR momentum solver with free-drift. This momentum solver set-up allowed for significant ice movement, however the ice closest to the left boundary did not move at all.

An example of a case executed with each of the three aforementioned momentum solvers is considered in this section. Figure 4.2 shows the spatial distribution of ice thickness and the surface current (red arrows) for the same case ran three times with an: EVP (left column), LSOR with no free-drift (middle column), and LSOR with free-drift (right column) momentum solver. Each of the three cases shown in figure 4.2 have a lake size that is 1,000,000 m^2 with a horizontal resolution of 10 m, and a lake depth of 20 m with a 0.2 m vertical resolution. The cases are all initialized with the same $-0.03°C$ initial surface temperature, constant $1°C$ air temperature, 150 W/m^2 downward shortwave and longwave radiation, and 3 m/s wind towards the right.

One issue that we noticed with the LSOR with free-drift case is that there is a single column of grid cells beside the left boundary that remains stagnant throughout the simulation. It is unclear as to why this collection of ice cells are sticking to the boundary. A temporary solution that acts as a work around this issue, that we use for the remainder of this thesis, is to add a frame of water around the ice block that is two grid cells wide. Once a frame of water is included around the initial ice mass, the LSOR momentum solver with free-drift works well and ice moves as expected over the lake. It is also worth noting that cases that use the LSOR momentum solver with free-drift also run more quickly than those using the EVP or the LSOR without free-drift momentum solvers. This is most likely due to the fact that the stress is set to zero for free-drift rheology.

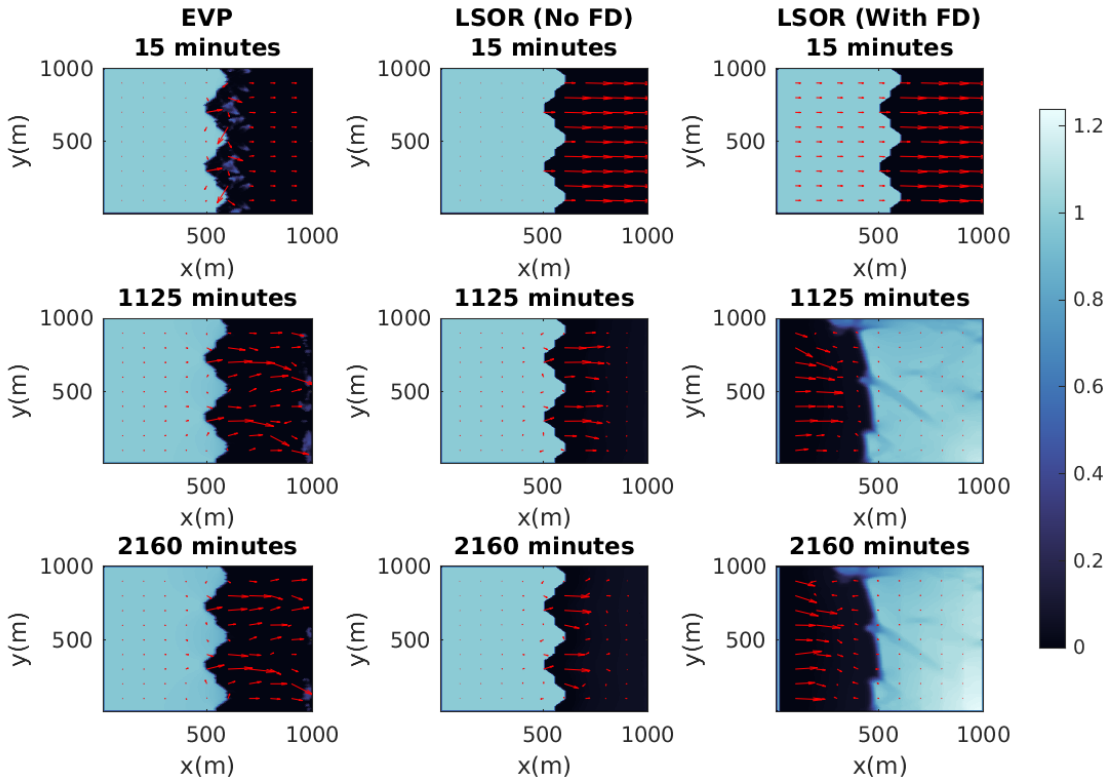

Figure 4.2: The spatial distribution of ice thickness and surface current (red arrows) are shown here for a case that uses three different momentum solvers at 15 minutes, 1125 minutes (18 hours and 45 minutes), and 2160 minutes (36 hours). The left column shows the case executed with the EVP solver, the middle column shows the case executed with the LSOR solver without free-drift, and the right column shows the case executed with the LSOR solver with free-drift. Colormap used from Thyng et al. [2016].

4.3 Ice Movement Results With a Water Frame

As a result of the discussion in the previous section regarding the momentum solvers and ice movement issue, the remainder of the simulations shown in this chapter were carried out using the LSOR momentum solver with free-drift rheology, and a frame of water (2 grid cells wide) around the initial ice mass. The first case that we will be considering briefly is case B1. Case B1 was run using the nonhydrostatic model, with a 1 m horizontal resolution, and no wind forcing. The purpose of running this case was to observe the lake

under wintertime conditions with no wind. Figure 4.3a displays the results of the spatial distribution of ice thickness for case B1 at the beginning, middle, and end of the 1.5 day simulation. Here, we see that without wind, the ice surface becomes increasingly fractured with time due to the warming surface. Additionally, figure 4.3b shows the fractional ice-covered area for case B1 at the beginning, middle, and end of the simulation. Note that this case is very similar to case A1 we discussed in chapter three, except case B1 has an initial partial ice cover. Results from A1 revealed that ice would appear when no wind forcing was present even when the surface temperature increased above freezing. It is difficult to observe because of the range in the colorbar given for figure 4.3a, however it is also true that ice is present in every surface grid cell by the end of the 1.5 day simulation for case B1. Moreover, the total volume of ice at the beginning of the simulation for case B1 was 4,925 m^3 and at the end of the 1.5 day simulation the total volume of ice had increased to 5,122 m^3, indicating that ice growth is occurring in this case.

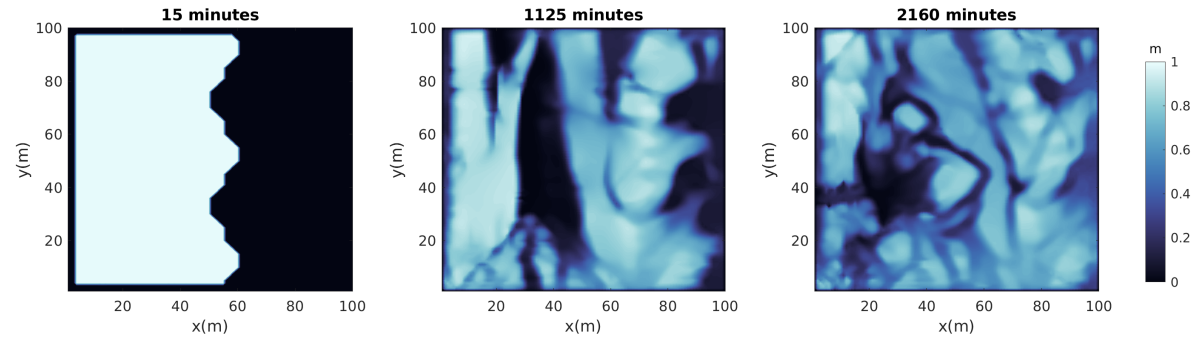

(a)

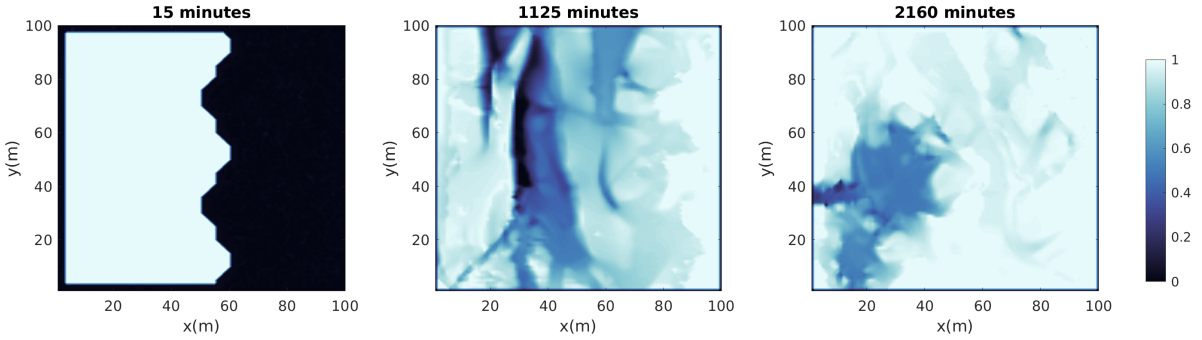

(b)

Figure 4.3: The spatial distribution of ice thickness (a) and the fractional ice-covered area (b) is shown here for case B1 at 15 minutes, 1125 minutes (18 hours and 45 minutes), and 2160 minutes (36 hours). Colormap used from Thyng et al. [2016].

The next case we will discuss is case B2. Case B2 was performed using the nonhydrostatic model, with 1 m horizontal resolution, and has a 3 m/s wind forcing towards the right. The left half of figure 4.4 shows the spatial distribution of ice thickness and the surface current (denoted by the red arrows) at the beginning, middle, and end of the 1.5 day simulation. The inclusion of the frame of water around the ice block resulted in the ice moving across the surface much easier than what we see in the LSOR with free-drift case from section 4.2. Referring once again to the left of figure 4.4, we can see that the surface currents of the lake tend to be much weaker in ice-covered regions and much stronger in open-water regions. This result suggests that the ice is acting as a barrier between the wind forcing and the surface of the lake. We also observe that, by midway through the

simulation, the velocity is strongest in the middle region of the lake (around $y = 40$ m to $y = 60$ m). We can see the re-circulation pattern forming as well in the ice-covered regions near the north and south boundaries.

Figure 4.5 shows the current and the temperature profile of the upper 4 m of case B2 for three different y-slices at the beginning, middle, and end of the 1.5 day simulation. The black dashed lines in the right half of figure 4.1 denote the locations of the three y-slices that are shown figure 4.5. Note that we chose to only show the upper 4 m rather than the full 20 m depth of the lake since this is where most of the activity takes place. At the beginning of the simulation, the temperature in the upper 4 m of the lake ranged between approximately -0.03°C and 0.7°C. By then end of the simulation the temperature ranges between 0.3°C and 0.85°C.

Initially, the y-slices all look relatively similar in figure 4.5, we can see that the current is stronger where there is no ice cover and we can see a small discoloration around $x = 60$ m denoting where the ice covered region and open-water region meet as shown in the left half of figure 4.4. We begin to notice differences between the y-slices at 1125 minutes. At 1125 minutes, the $y = 32$ m and $y = 82$ m slices look relatively similar, but the $y = 52$ m slice is quite different. The $y = 32$ m and $y = 82$ m slices have strong currents moving towards the right in the open water regions and a very weak current moving towards the left in the ice-covered regions. The vertical circulation pattern appears to be strong currents moving towards the right near the surface and then, underneath the surface, there is a less strong current moving towards the left. The $y = 52$ m slice has a strong current moving towards the right in open water regions as well, but this slice also shows currents moving towards the right in the ice-covered region. The $y = 52$ m slice also shows a strong current moving towards the right all throughout the vertical domain. The primary vertical temperature profile that we see for all slices is curved in the open water region and relatively flat horizontally in the ice-covered regions with the temperatures increasing from the surface towards the bottom. We can see that there is a build-up of cooler water near the surface right before a thin ice sheet begins to form, then under the thin ice the water is warmer, and finally under the thicker ice the water is slightly cooler than the water directly under the thinner ice.

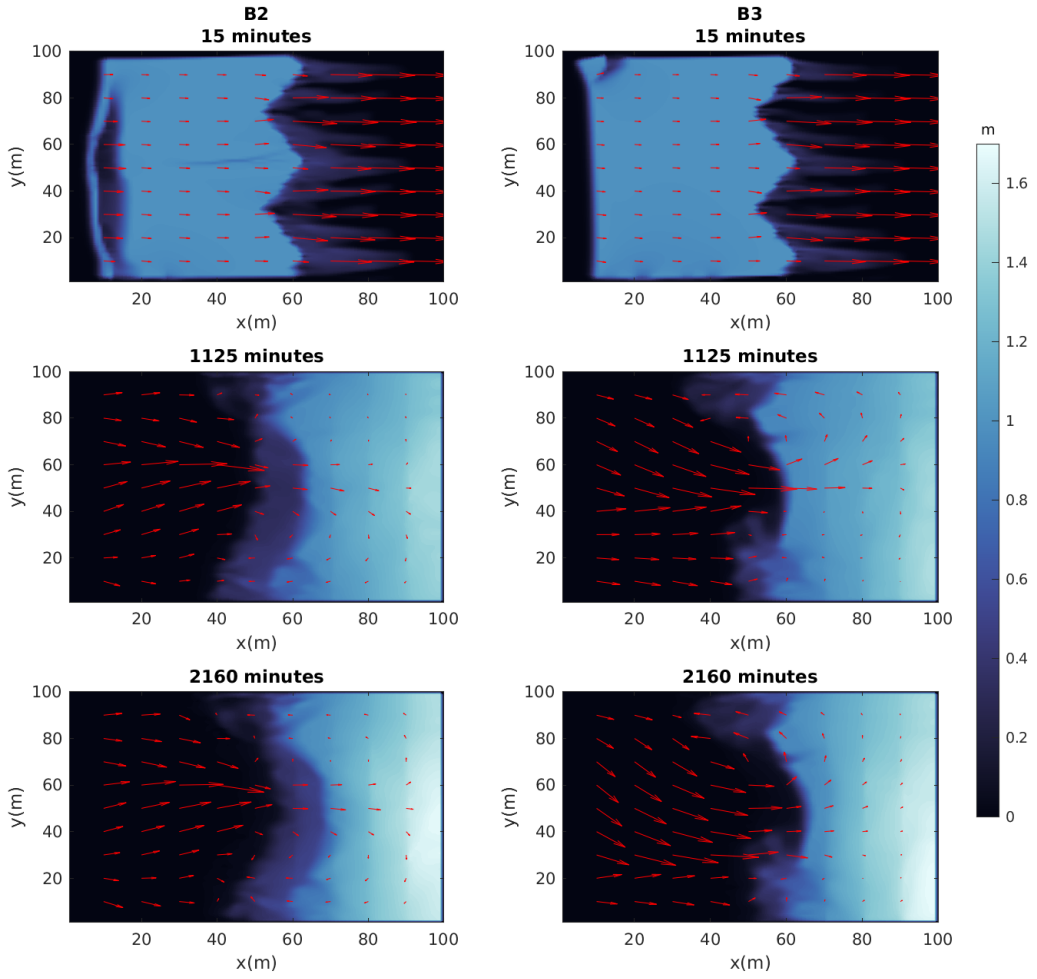

Figure 4.4: The spatial distribution of ice thickness and surface current (arrows) for cases B2 (left) and B3 (right) at 15 minutes, 1125 minutes (18 hours and 45 minutes), and 2160 minutes (36 hours). The only difference between cases B2 and B3 is that case B2 was executed using the nonhydrostatic model and case B3 was executed using the hydrostatic model. The maximum magnitude of the arrows for both cases is 0.02 m/s. Colormap used from Thyng et al. [2016].

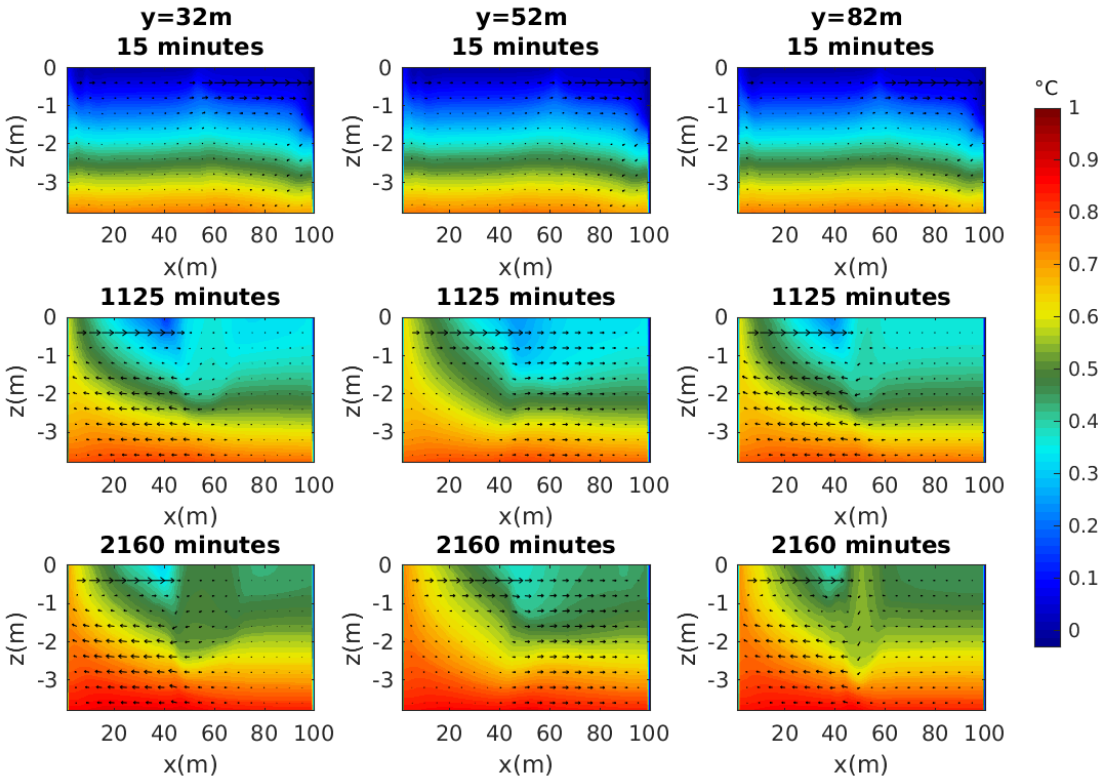

Figure 4.5: The temperature profile of the upper 4 m, and the current (arrows) for case B2 at 15 minutes, 1125 minutes (18 hours and 45 minutes), and 2160 minutes (36 hours). There are three different y-slices of the domain shown. Reference location of the y-slices can be seen via the dashed black lines in figure 4.1.

Now that we have explored case B2 in depth, we will take a somewhat briefer look at cases B3, B4, B5, B6, and B7. First, we will consider case B3. Case B3 was run using the hydrostatic version of the model instead of the nonhydrostatic version of the model as in case B2. Convection is a nonhydrostatic process, however using the nonhydrostatic model is much more computationally expensive than using the hydrostatic version of the model. So, it is reasonable to execute a run where we use the hydrostatic model to determine if there are any significant difference between the two cases.

The right half of figure 4.4 shows the spatial distribution of ice thickness and the surface current for case B3. Observing this figure and comparing it to case B2 on the left, we can see that one of the primary differences between the two cases is the lack of symmetry in

the hydrostatic case, though it is unclear why this is occurring. The two cases begin very similarly, they both have surface currents moving towards the right that are stronger in open water regions and weaker in ice-covered regions. Notice that the ice does initially break up slightly different in the two cases. By the end of the simulation at 2160 minutes, the results for the two cases look somewhat different. Case B2 (on the left of figure 4.4) is relatively symmetric about $y = 50$ m, compared to case B3 (on the right). We see recirculation occurring to a similar degree in the southern and northern regions in case B2, but case B3 appears to have a stronger recirculation pattern in the northern region. One enticing feature of the hydrostatic model is that the simulations take much less time to run than when using the nonhydrostatic model. For example, using the Compute Canada machine, Graham, with 100 processors, case B2 (nonhydrostatic) took approximately 31 hours to execute but case B3 (hydrostatic) only took approximately 10 hours to complete. This time difference gets much larger as domain size increases and resolution gets finer.

Figure 4.6 shows the current (arrows) along with the temperature profile of the upper 4 m of the lake for case B3. To get a better appreciation for the differences between the hydrostatic and nonhydrostatic case, it is appropriate to see how the temperature and current evolves vertically over time for both cases. We described what was happening in figure 4.5 in detail, so we will only explore the differences between figures 4.5 and 4.6 here. It is worth noting that the ice distribution is slightly different for these two cases (as can be seen in figure 4.4), and this will account for some differences that we see in the temperature profiles and current. At the beginning of the simulation, the hydrostatic and nonhydrostatic case look relatively similar. The first difference to point out between the two cases is the current at 1125 minutes (18 hours and 45 minutes). For case B2, there appears to be a smoother transition in the current between the open water and ice-covered regions compared to case B3. In case B3 we can see a sudden strong downward current at $y = 32$ m, a similar phenomena can be seen in the $y = 82$ m at the same time. There appears to be stronger gradients in the temperature field in the hydrostatic case. We noted previously that figure 4.4 showed a recirculation pattern that favored the northern region of the lake in the hydrostatic case, we can also see this occurring in figure 4.6 where we see a strong current moving towards the left shown throughout most of the panel at $y = 82$ m and 2160 minutes (36 hours), and a much weaker current moving towards the left at $y = 32$ m for the same time.

Figure 4.7 shows the kinetic energy of the surface currents at 15 minutes, 1125 minutes (18 hours and 45 minutes), and 2160 minutes (36 hours). The kinetic energy was computed as $KE = \frac{1}{2}(U^2 + V^2)$, where U and V are the lake horizontal velocity components. Comparing figure 4.7 to figure 4.4, we can observe that the energy is generally strongest in the open-water regions. The kinetic energy plots behave largely as expected when com-

paring them to the spatial ice distribution and surface current plots for the same cases. The energy tends to be strongest closer to the middle of the domain (around $y = 50$ m to $y = 60$ m) for the nonhydrostatic (B2) case, and the kinetic energy takes on a more nonsymmetric pattern for the hydrostatic (B3) case. Overall, the kinetic energy gradients are sharper for the non-hydrostatic case.

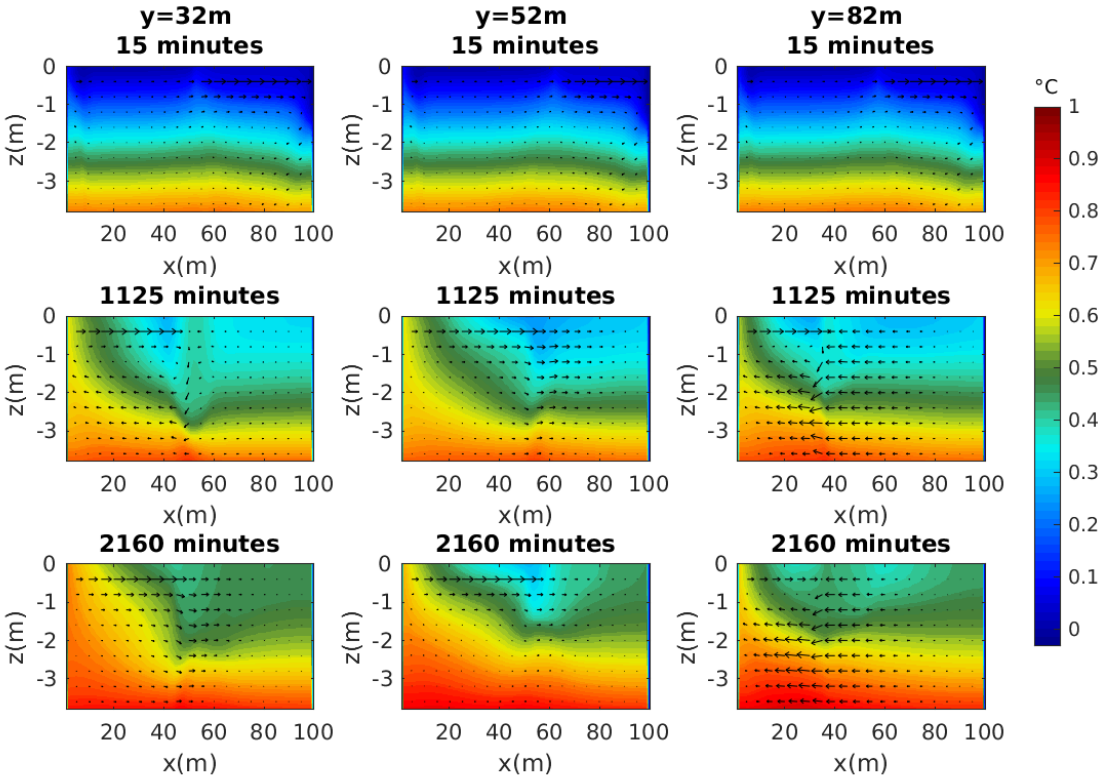

Figure 4.6: The temperature profile of the upper 4 m, and the current (arrows) for case B3 at 15 minutes, 1125 minutes (18 hours and 45 minutes), and 2160 minutes (36 hours). There are three different y-slices of the domain shown. Reference location of the y-slices can be seen via the dashed black lines in figure 4.1.

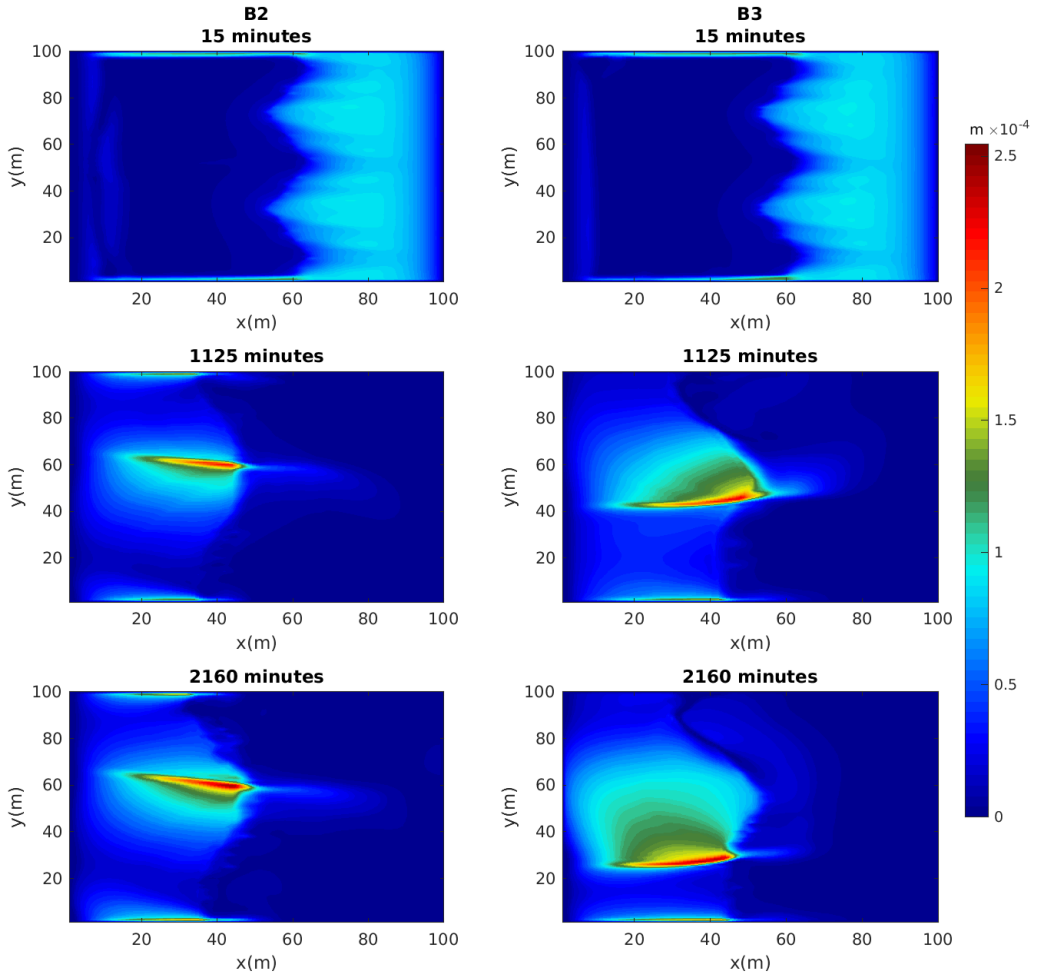

Figure 4.7: The kinetic energy of surface currents for cases B2 (left) and B3 (right) at 15 minutes, 1125 minutes (18 hours and 45 minutes), and 2160 minutes (36 hours). The only difference between cases B2 and B3 is that B2 was executed using the nonhydrostatic model and B3 was executed using the hydrostatic model.

Next we will compare case B2 and case B4. Case B4 is a 1,000×1,000 m lake with a 10 m horizontal resolution, and case B2 is a 100×100 m lake with a 1 m horizontal resolution. Moreover, the background horizontal and vertical diffusion and viscosity coefficients also

differ between cases B2 and B4 (see table 4.2). The purpose of comparing cases B2, B4, and B6 is to study how results, such as ice thickness and surface current, scale with size and resolution. Since we have altered the horizontal domain size and the horizontal resolution simultaneously for cases B2, B4, and B6 it is difficult to fully determine which differences in results are due to the horizontal size of the lake and which differences are due to the horizontal resolutions. It seems most likely that horizontal resolution is the more important factor in result differences between cases since forcing is relatively proportional between cases, however more work should be done to determine this for certain. Furthermore, the initial ice mass for these cases differ as well and should be kept in mind as we discuss the differences between cases B2, B4, and B6. The right half of figure 4.1, displays the shape of the initial ice mass for each simulation in this chapter. The shape of the initial ice mass remains the same for each case, even if the horizontal domain of the lake is increased. For example, if the components of the initial ice mass that jet out the furthest are 5 grid cells long, then in case B2 that would represent 5 m, in case B4 it would represent 50 m, and in case B6 it would represent 500 m.

Figure 4.8 displays noticeable differences between the spatial distribution of ice thickness for case B2 (left) and B4 (right). We observe that the ice does not break up at 15 minutes for case B4 as it did with case B2. Additionally, the maximum ice thickness for case B4 is less than the maximum ice thickness for case B2. The final spatial distribution of ice thickness does look somewhat similar for the two cases except for the small patch of ice jetting out from the main ice mass in the middle of the lake for case B4. Other differences in the final spatial distribution of ice thickness may be due to the fact that the surface currents in case B2 have a structure that seems more jet-like than what was seen in case B4, and this may be contributing to the shape of the ice edge for case B2. Moreover, the circulation of the surface current is somewhat different for the larger lake than it is for the smaller lake. The circulation for the larger lake is weaker than what we see for case B2, and the surface circulation appears less ordered in case B4 in comparison to case B2 according to figure 4.8. Another noticeable difference between the two cases is that, at 2160 minutes (36 hours), the (B2) case with the smaller lake and finer resolution has a section of thin ice off of the main ice mass, and the (B4) case with the larger lake and coarser resolution does not appear to possess this feature to the same extent. Figure 4.8 indicates that case B4 takes longer for ice to pile-up at the right boundary, and small amounts of thin ice can be seen near the ice edge of the ice mass for case B4 at 2160 minutes (36 hours).

Figure 4.9 displays the kinetic energy of the surface currents for the smaller lake (B2) case and the larger lake (B4) case. The kinetic energy values for case B4 have been multiplied by 10 in this figure. The kinetic energy values were scaled for easier comparison purposes since the larger lake size resulted in decreased local kinetic energy values. This

decrease in local kinetic energy values is to be expected, given that the surface velocity also decreases in case B4 compared to case B2. Cases B2 and B4 have similar maximum surface velocity values around 0.02 m/s, however there are much fewer instances of this high velocity occurring and the average value of surface velocity is smaller in case B4. The weaker surface velocity in case B4 likely has more to do with horizontal resolution than it does with the horizontal domain size. The kinetic energy of the surface currents for case B4 is somewhat similar to case B2, but rather than having one elongated region of strong energy, case B4 had two more circular regions close to the ice edge. Results from both of these cases indicate that the kinetic energy of the surface currents are stronger, typically, in open-water regions. This suggests that the ice is acting as a barrier between the lake surface and the wind forcing.

Next, we will compare cases B4 and B5. The only difference between cases B4 and B5 is that case B4 has rotation turned on, and case B5 has no rotation. Referring to figure 4.10, we can see that rotation does indeed does have an affect here. Without rotation the ice builds up near the right boundary with a straighter ice edge. We can observe that the circulation in case B5 is almost exclusively towards the right, except for an interesting little anomaly near the northern boundary. The small pocket of circulation near the northern boundary is numerical since the initial conditions and forcing are symmetric about the middle of the lake. The small section of ice jetting out near the northern boundary in case B5 further demonstrates that the surface current influences the shape of the ice edge. There are also noticeable differences between cases B4 and B5 that can be detected from the kinetic energy of the surface currents as seen in figure 4.11. The kinetic energy seen in case B5 is much more symmetric than what is seen for case B4, this behaviour is to be expected given the lack of rotation. Apart from this however, the plots do not look overly different, similar magnitudes of kinetic energy are observed.

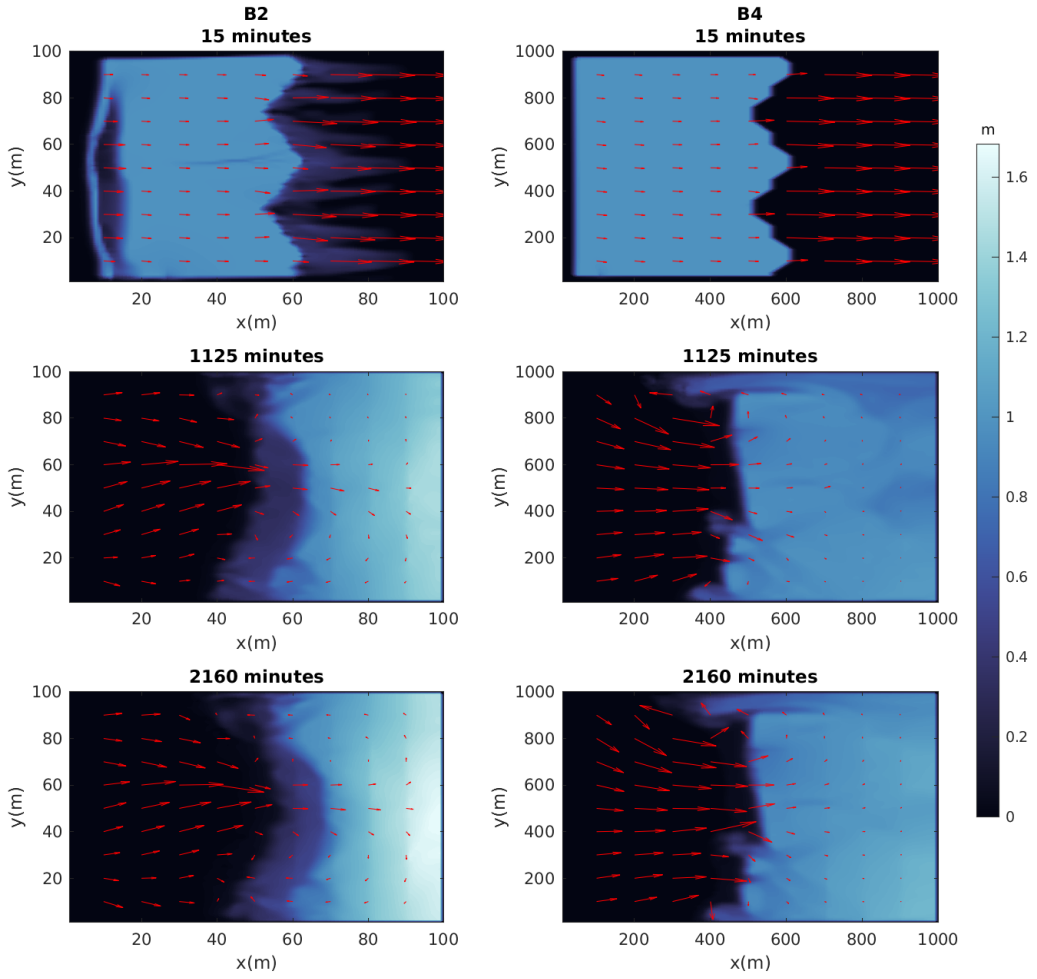

Figure 4.8: The spatial distribution of ice thickness and surface current (arrows) for cases B2 (left) and B4 (right) at 15 minutes, 1125 minutes (18 hours and 45 minutes), and 2160 minutes (36 hours). The differences between cases B2 and B4 include background horizontal and vertical viscosity and diffusion values (see table 4.2), and case B2 uses a 100×100 m lake with a 1 m horizontal resolution and case B4 uses a 1,000×1,000 m lake with a 10 m horizontal resolution. The maximum magnitude of the arrows is 0.02 m/s for both cases. Colormap used from Thyng et al. [2016].

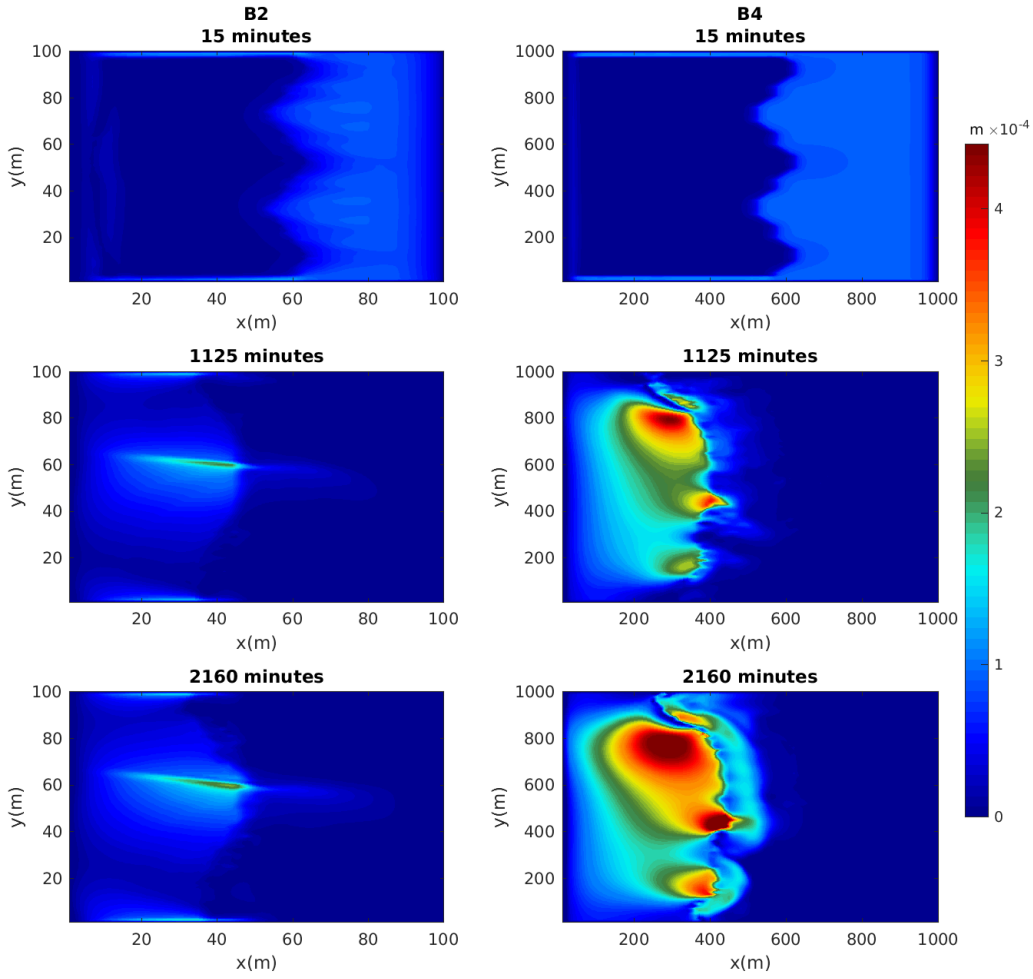

Figure 4.9: The kinetic energy of surface currents for cases B2 (left) and B4 (right) at 15 minutes, 1125 minutes (18 hours and 45 minutes), and 2160 minutes (36 hours). The differences between cases B2 and B4 include background horizontal and vertical viscosity and diffusion values (see table 4.2), and case B2 uses a 100×100 m lake with a 1 m horizontal resolution and case B4 uses a 1,000×1,000 m lake with a 10 m horizontal resolution. Note that the kinetic energy values for case B4 have been multiplied by 10 since the larger domain size with a coarser resolution resulted in decreased local kinetic energy values.

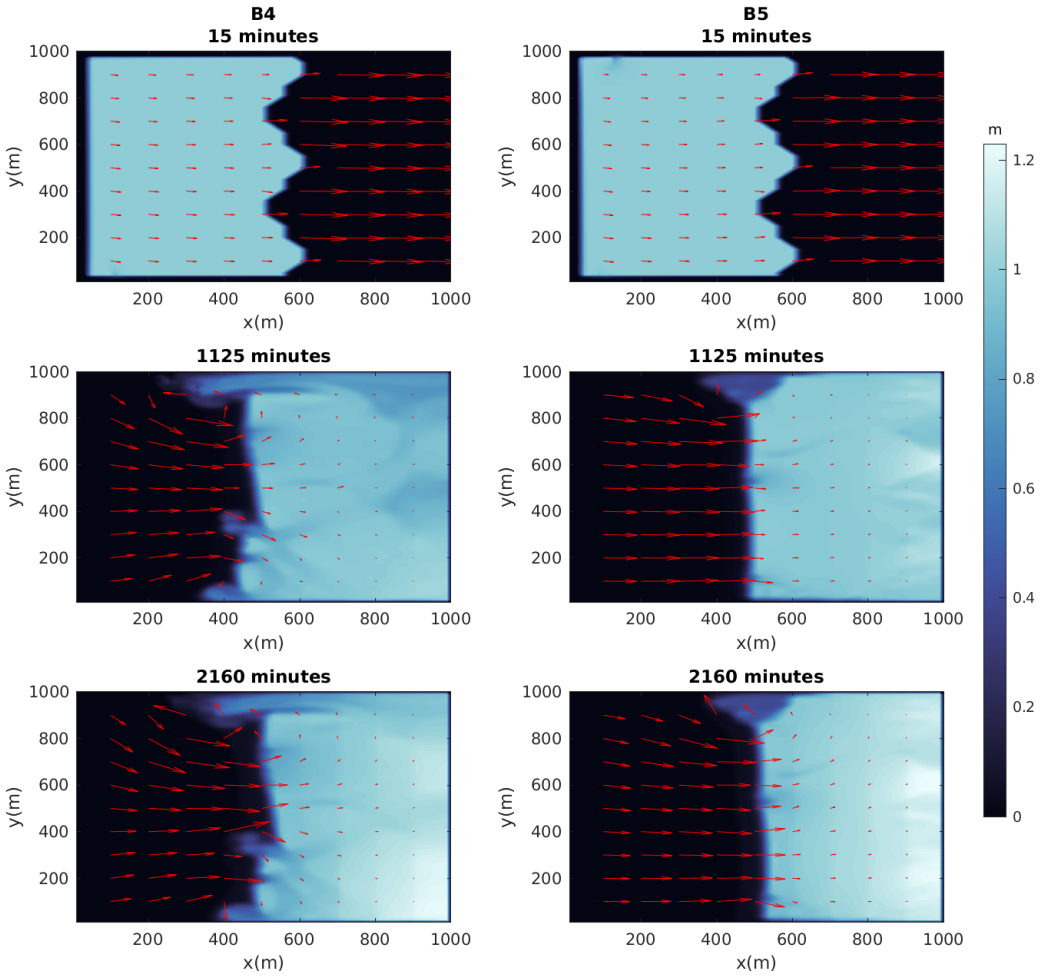

Figure 4.10: The spatial distribution of ice thickness and surface current (arrows) for cases B4 (left) and B5 (right) at 15 minutes, 1125 minutes (18 hours and 45 minutes), and 2160 minutes (36 hours). Both of these cases are exactly the same except that case B4 has rotation and case B5 has no rotation. The maximum magnitude of arrows is 0.02 m/s for both cases. Colormap used from Thyng et al. [2016].

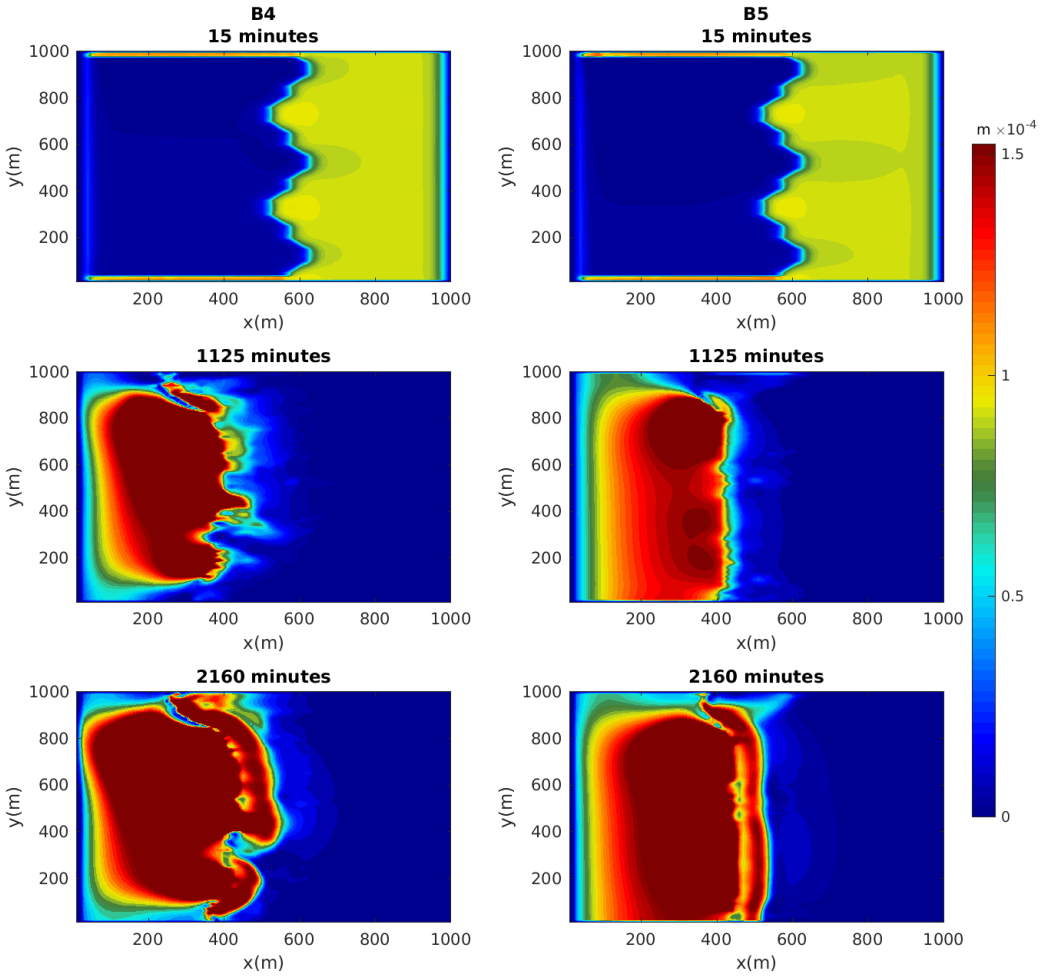

Figure 4.11: The kinetic energy of surface currents for cases B4 (left) and B5 (right) at 15 minutes, 1125 minutes (18 hours and 45 minutes), and 2160 minutes (36 hours). Both of these cases are exactly the same except that case B4 has rotation and case B5 has no rotation. Note that the kinetic energy values for both case B4 and case B5 have been multiplied by 10 since the larger domain size with coarser resolution resulted in decreased local kinetic energy values. Also note that the colorbar covers a much smaller range in this figure than the colorbar shown in figure 4.9

.

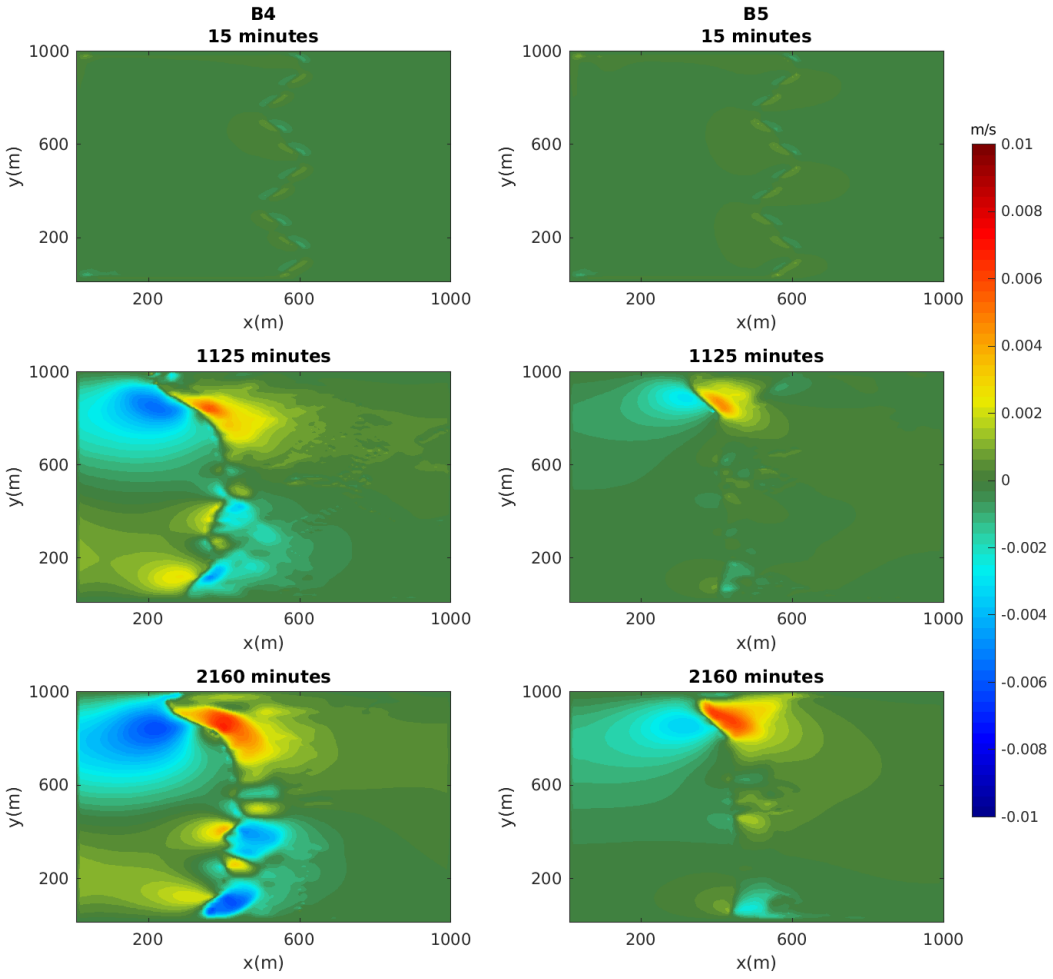

Figure 4.12: The v-component of the velocity at the upper grid cell of the lake for cases B4 and B5 at 15 minutes, 1125 minutes (18 hours and 45 minutes), and 2160 minutes (36 hours) at $z = 0$ m (the surface). The only difference between case B4 and B5 is that B4 has rotation, and case B5 has no rotation.

Since case B4 considers rotation and case B5 does not, it seems reasonable to also study the differences between the two for the v-component of the velocity of the upper grid cell of the lake (see figure 4.12). Near the beginning of the simulation, cases B4 and B5 look very

similar. Noticeable differences between the two cases begin to appear closer to midway through the simulation. Case B4 and case B5 actually have similar velocity patterns, meaning that both cases include positive and negative velocities at similar locations in their respective lakes. However, the velocity is much stronger and has a greater range for case B4 since it considers rotation.

Figure 4.13 displays the surface current and spatial distribution of the ice thickness for cases B2 and B6. Similarly to the differences between cases B2 and B4, cases B2 and B6 also differ in horizontal domain size and horizontal resolution, background horizontal and vertical viscosity and diffusion coefficients (see table 4.2), and in the length scale of the initial ice mass. The domain size of case B2 is 100×100 m with a 1 m horizontal resolution, and the lake size for case B6 is 10,000×10,000 m with a 100 m horizontal resolution. The most noticeable difference between cases B2 and B6 that we observe in figure 4.13 is that the ice in case B6 never completely makes it over to the right boundary after the 2160 minutes (36 hours). The surface current also looks quite different in case B6 compared to B2. Case B2 shows a relatively ordered circulation pattern, though case B6 appears as if it has a vortex in the middle of the ice. Figure 4.14 displays the kinetic energy of surface currents for case B2 (left) and B6 (right). The values of kinetic energy for case B6 have been multiplied by 100 in this figure since the larger lake appears to decrease local kinetic energy values. The reason for the decreased local kinetic energy values in case B6 are the same as those given for the decreased local kinetic energy values in case B4. As the horizontal lake size increases and the horizontal resolution becomes more coarse, the surface velocity decreases (see figure 4.17 for an example of the decreased u-component of the surface lake velocity). There are strong kinetic energy values around the same location as the vortex for case B6 at 2160 minutes (36 hours).

The horizontal size of the lake as well as the horizontal resolution certainly seems to be suggesting that it has a large impact on the spatial distribution of ice thickness and surface current. Figure 4.15 displays the surface current and spatial distribution of ice thickness at 15 minutes, 1125 minutes (18 hours and 45 minutes), and 2160 minutes (36 hours) for cases B2, B4, and B6. This figure shows a clear comparison for the same case with three different domain sizes and horizontal resolutions. As the lake gets larger, the ice appears to become thinner. Perhaps the larger domain size requires more time for the ice to reach the right boundary and to begin piling-up. It also appears that, as the lake gets larger and the horizontal resolution gets more coarse, the surface current becomes more chaotic.

Figure 4.16 shows the profile for the u-component of the velocity for cases B2, B4, and B6 for $y = 50$ m, $y = 500$ m, and $y = 5000$ m, respectively, at 1125 minutes (18 hours and 45 minutes) and 2160 minutes (36 hours). The purpose of this figure was to observe if the increased horizontal lake size and coarser horizontal resolution would have any influence

on the vertical profile of the lake even though the depth and vertical resolution remains unchanged. There is a noticeable difference in the velocities between the three cases. For case B2 the velocity contours are smooth and indicate a large region with flow to the right, decreasing in magnitude deeper in the lakes. Cases B4 continues this trend to a lesser extent, we observe that the strong positive velocity is not a far ranging (relative to lake size) as it is for case B2. The velocity profile for case B6 appears much more noisy than the other two cases, and it is not entirely clear why this is true. Note that we increased the background horizontal and vertical viscosities and diffusivities as the lake size was increased (see table 4.2). We altered our background horizontal viscosities and diffusivities values such that they increased proportional to grid size as was done in a study by Padon and Ashkenazy [2018]. We also chose to scale our background vertical viscosities and diffusivities values in the same manner.

Table 4.2: The horizontal and vertical background diffusivities and viscosities for cases B1-B7.

	Horizontal Diffusivity	**Vertical Diffusivity**	**Horizontal Viscosity**	**Vertical Viscosity**
B1, B2, B3, B7	1×10^{-4}	1×10^{-4}	7×10^{-4}	7×10^{-4}
B4, B5	1×10^{-3}	1×10^{-3}	7×10^{-3}	7×10^{-3}
B6	1×10^{-2}	1×10^{-2}	7×10^{-2}	7×10^{-2}

Figures 4.17 - 4.19 show plots of cases B2, B4, and B6 at 15 minutes, 1125 minutes (18 hours and 45 minutes), and 2160 minutes (36 hours) for $z = 0$ m, $z = -2$ m, and $z = -4$ m. Figure 4.17 shows a more detailed look of the surface circulation than the surface current vectors plotted on the previous ice thickness figures do. In general, figures 4.17 - 4.19 show that case B2 has stronger surface current vectors plotted on the previous ice thickness figures than cases B4 and B6. These figures also continue the trend of more noise appearing in the larger lakes that we originally saw in figure 4.16.

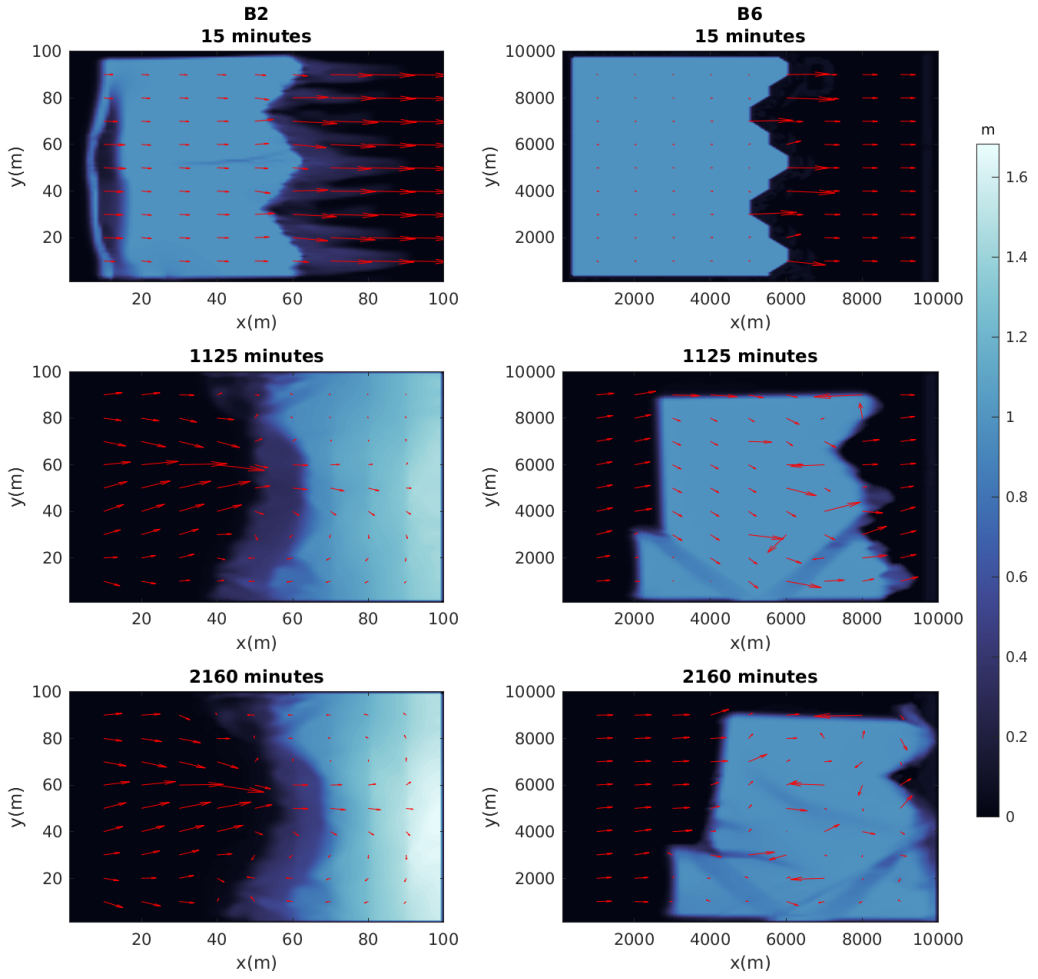

Figure 4.13: The spatial distribution of ice thickness and surface current (arrows) for cases B2 (left) and B6 (right) at 15 minutes, 1125 minutes (18 hours and 45 minutes), and 2160 minutes (36 hours). The differences between cases B2 and B6 include background horizontal and vertical viscosity and diffusion values (see table 4.2), and case B2 uses a 100×100 m lake with a 1 m horizontal resolution and case B6 uses a 10,000×10,000 m lake with a 100 m horizontal resolution. The maximum magnitude of arrows is 0.02 m/s for case B2 and 0.008 m/s for case B6. Colormap used from Thyng et al. [2016].

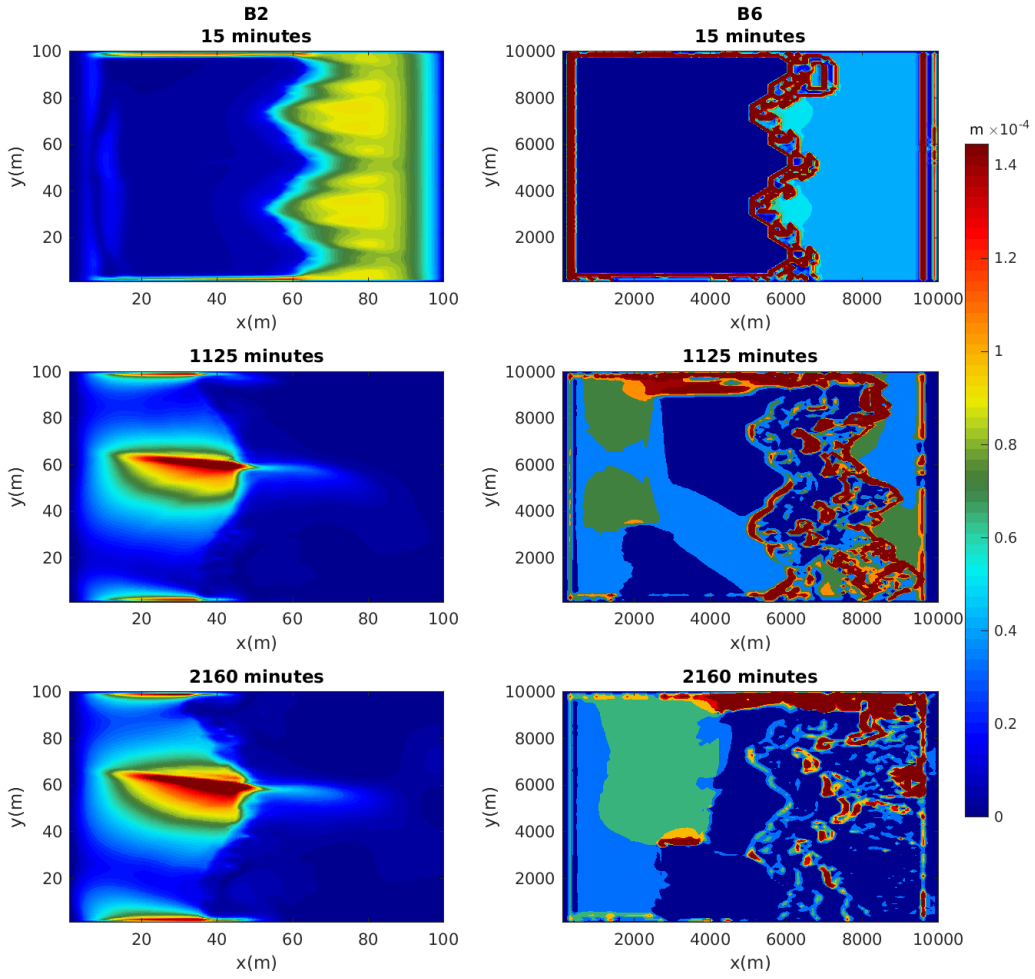

Figure 4.14: The kinetic energy of surface currents for cases B2 (left) and B6 (right) at 15 minutes, 1125 minutes (18 hours and 45 minutes), and 2160 minutes (36 hours). The differences between cases B2 and B6 include background horizontal and vertical viscosity and diffusion values (see table 4.2), and case B2 uses a 100×100 m lake with a 1 m horizontal resolution and case B6 uses a 10,000×10,000 m lake with a 100 m horizontal resolution. Note that the kinetic energy values for case B6 have been multiplied by 10 since the larger domain size with a coarser resolution resulted in decreased local kinetic energy values.

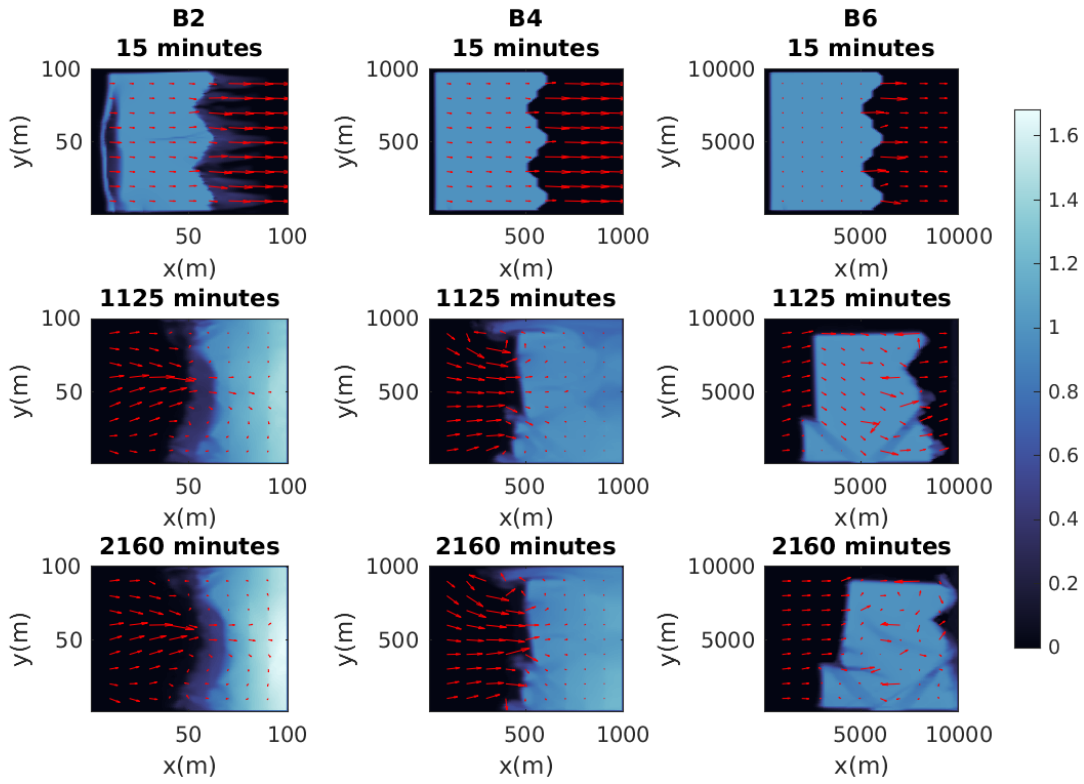

Figure 4.15: The spatial distribution of ice thickness and surface current (arrows) for cases B2 (left), B4 (middle), and B6 (right) at 15 minutes, 1125 minutes (18 hours and 45 minutes), and 2160 minutes (36 hours). The differences between each case include background horizontal and vertical vicosities and diffusivities (see table 4.2), and case B2 uses a 100×100 m lake with a 1 m horizontal resolution, case B4 uses a 1,000×1,000 m lake with a 10 m horizontal resolution, and case B6 uses a 10,000×10,000 m lake with a 100 m horizontal resolution. The maximum magnitude of the arrows is 0.02 m/s for cases B2 and B4, and 0.008 m/s for case B6. Colormap used from Thyng et al. [2016].

Finally, we compare case B2 and case B7. Case B7 simply has a 6 m/s wind forcing towards the right compared to the 3 m/s wind forcing towards the right in case B2. This case behaves as expected, the ice becomes much thicker due to pile-up in case B7 as a result of the stronger wind. The stronger wind also ensures that very little of the surface

current is moving towards the left after ricocheting off of the right boundary. Figure 4.21 shows the kinetic energy of surface currents for cases B2 and B7. As expected, the energy in the B7 case is much stronger than it is in case B2 due to the increased wind forcing. However, the two cases do follow a very similar trend with the strongest energy located mainly in the middle of the lake and near the northern and southern boundaries.

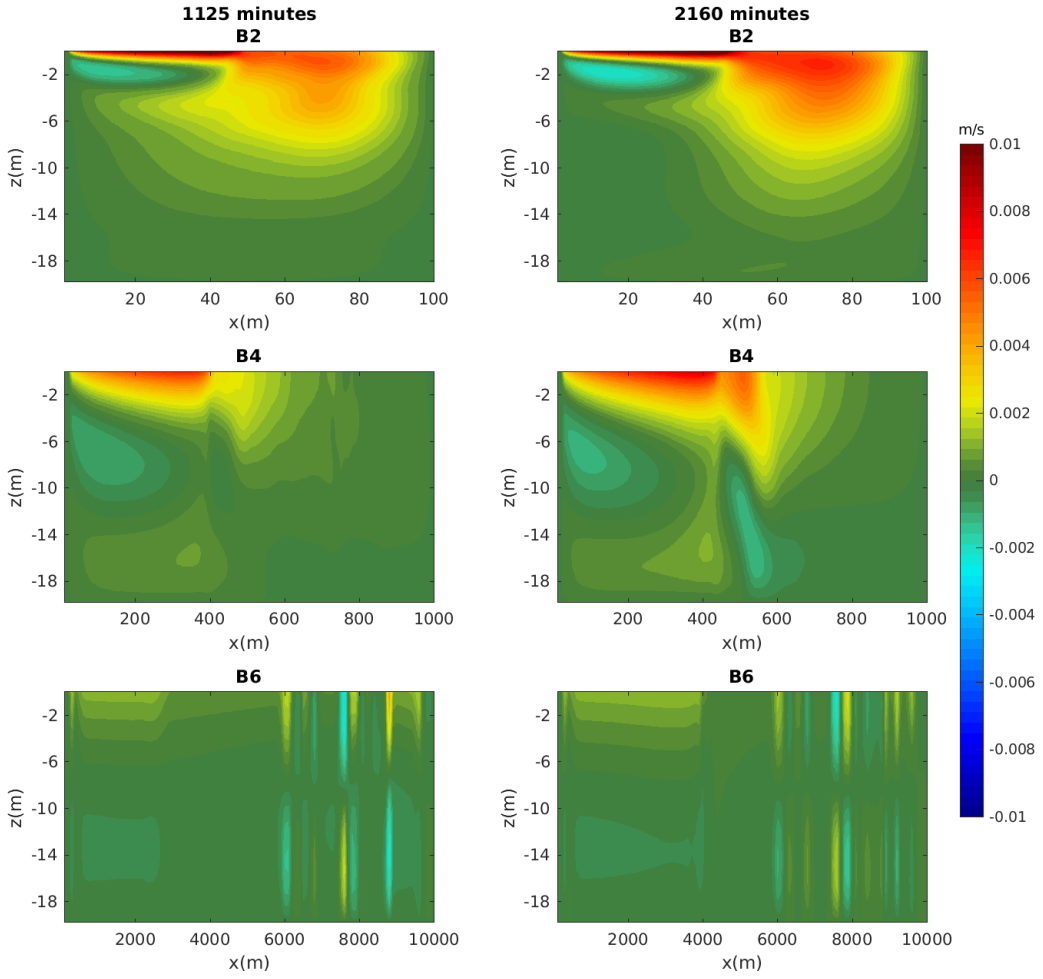

Figure 4.16: The u-component of the velocity profile for cases B2, B4, and B6 for $y = 50$ m, $y = 500$ m, and $y = 5000$ m, respectively, at 1125 minutes (18 hours and 45 minutes) and 2160 minutes (36 hours).

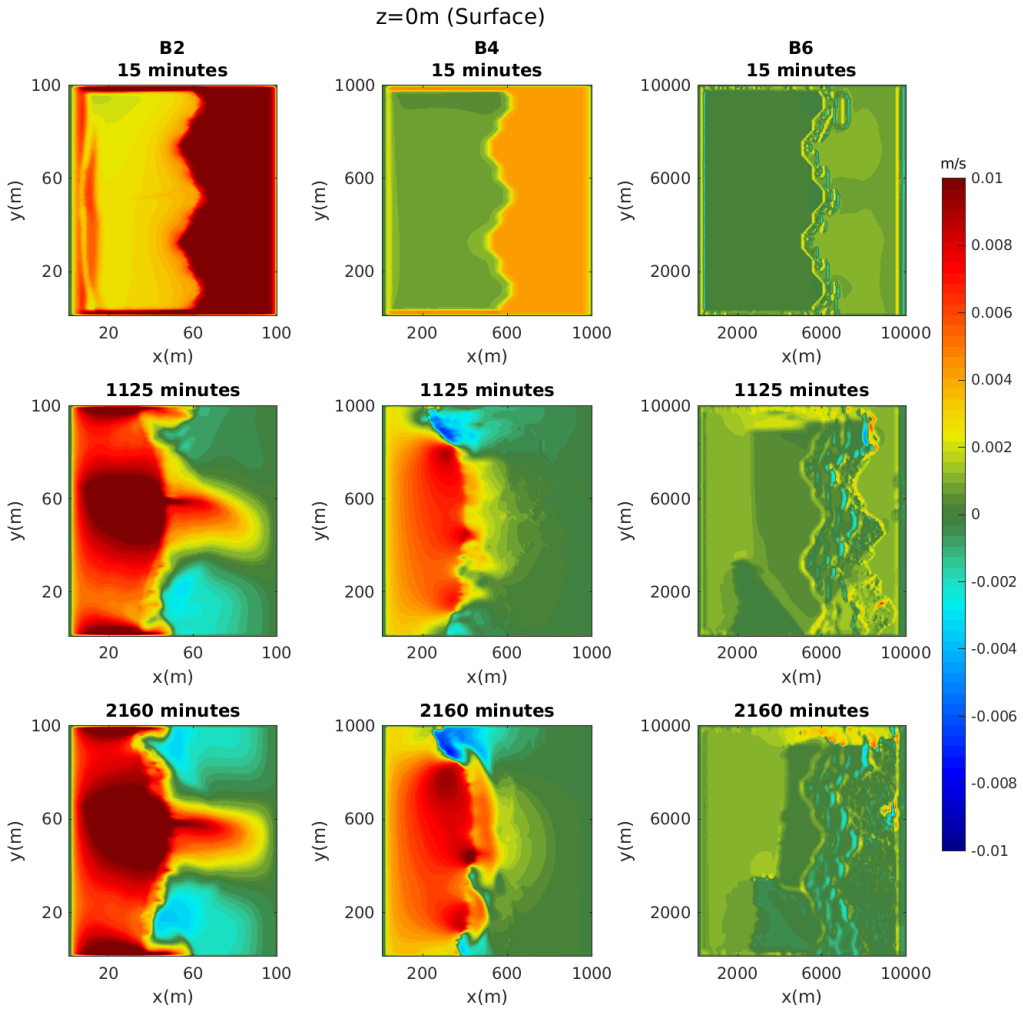

Figure 4.17: The xy-view of the u-component of the velocity at $z = 0$ m (the lake surface) for cases B2, B4, and B6 at 15 minutes, 1125 minutes (18 hours and 45 minutes), and 2160 minutes (36 hours).

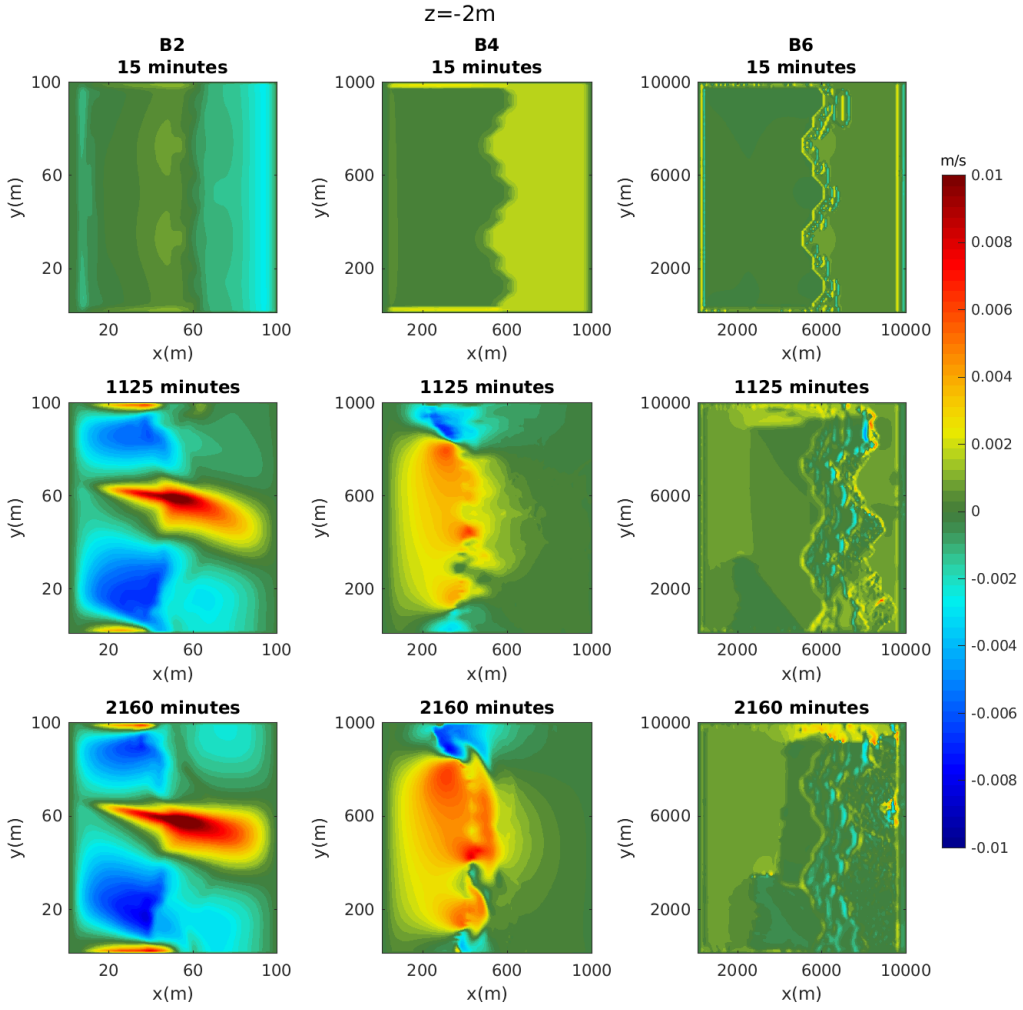

Figure 4.18: The xy-view of the u-component of the velocity at $z = -2$ m for cases B2, B4, and B6 at 15 minutes, 1125 minutes (18 hours and 45 minutes), and 2160 minutes (36 hours).

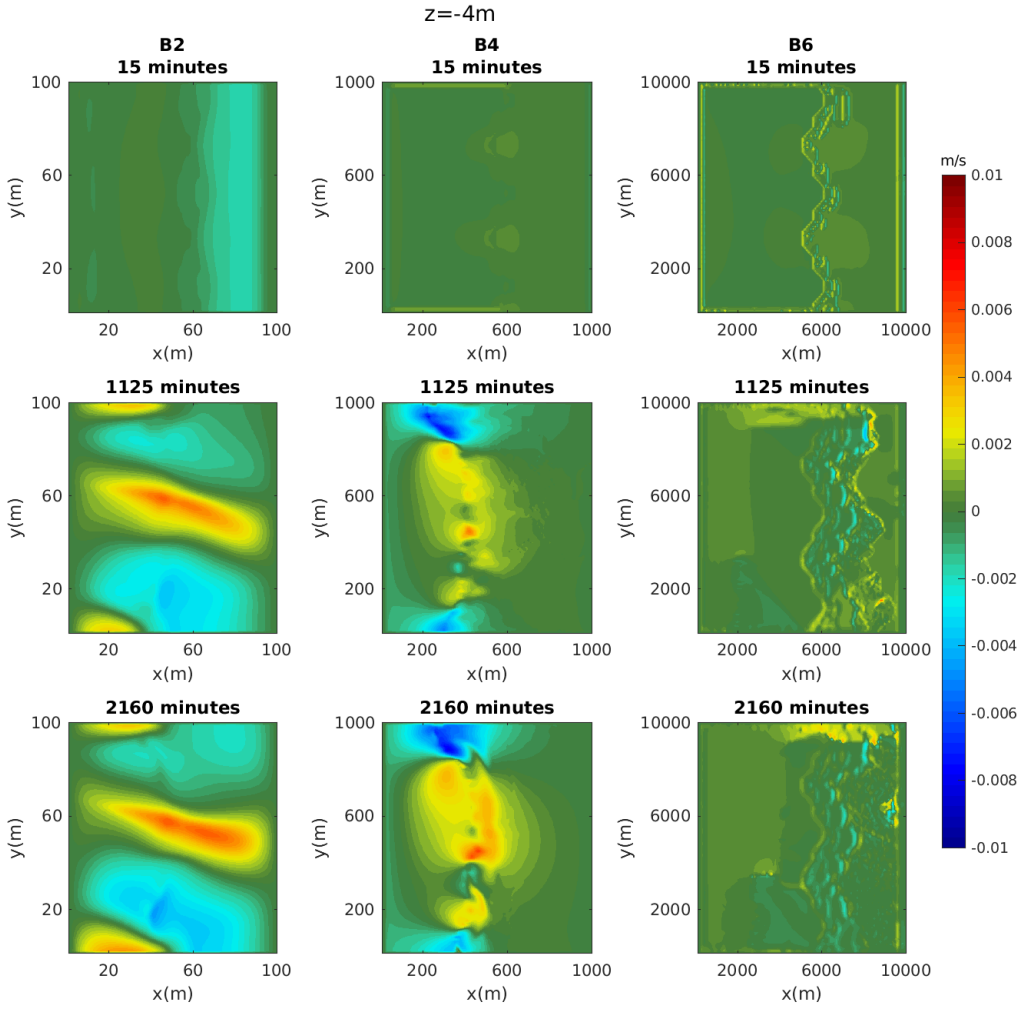

Figure 4.19: The xy-view of the u-component of the velocity at $z = -4$ m for cases B2, B4, and B6 at 15 minutes, 1125 minutes (18 hours and 45 minutes), and 2160 minutes (36 hours).

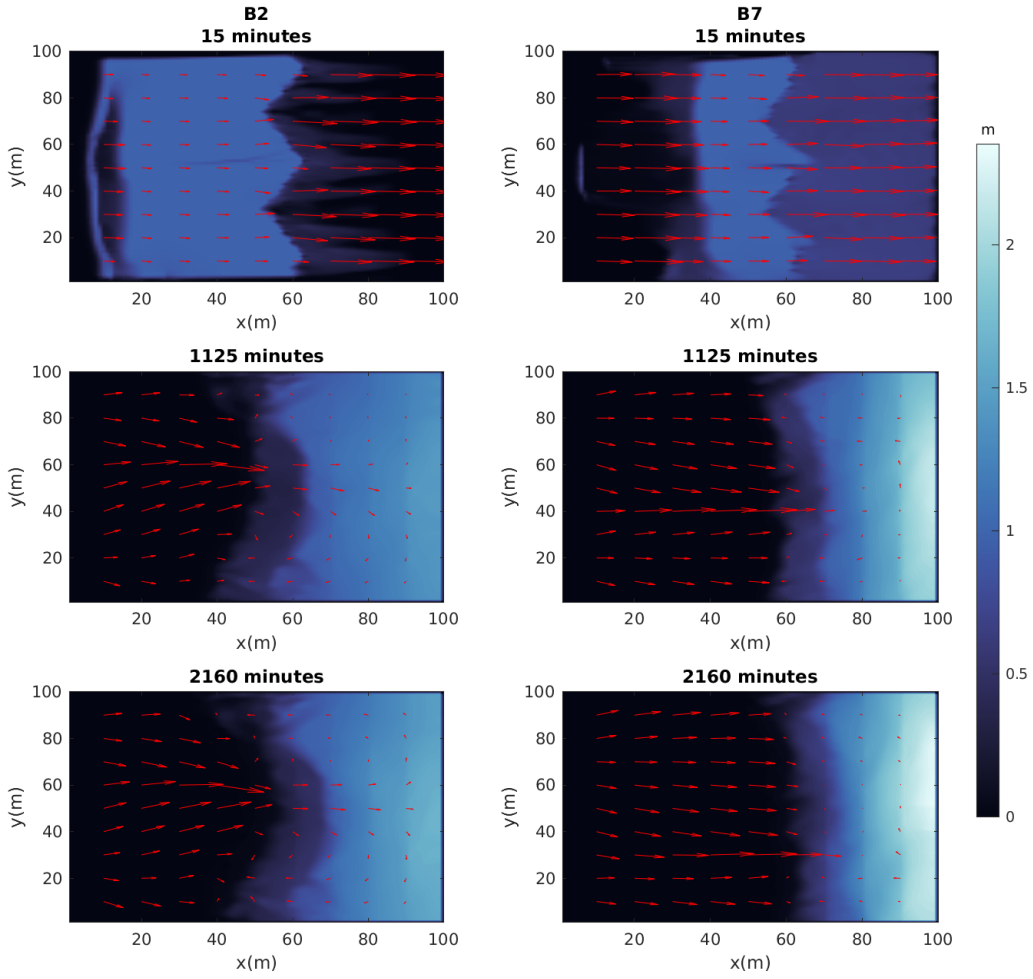

Figure 4.20: The spatial distribution of ice thickness and surface current (arrows) for cases B2 (left) and B7 (right) at 15 minutes, 1125 minutes (18 hours and 45 minutes), and 2160 minutes (36 hours). The only difference between cases B2 and B7 is that case B2 has 3 m/s wind forcing towards the right, and case B7 has a 6 m/s wind forcing towards the right. The maximum magnitude of the arrows is 0.02 m/s for case B2 and 0.06 m/s for case B6. Colormap used from Thyng et al. [2016].

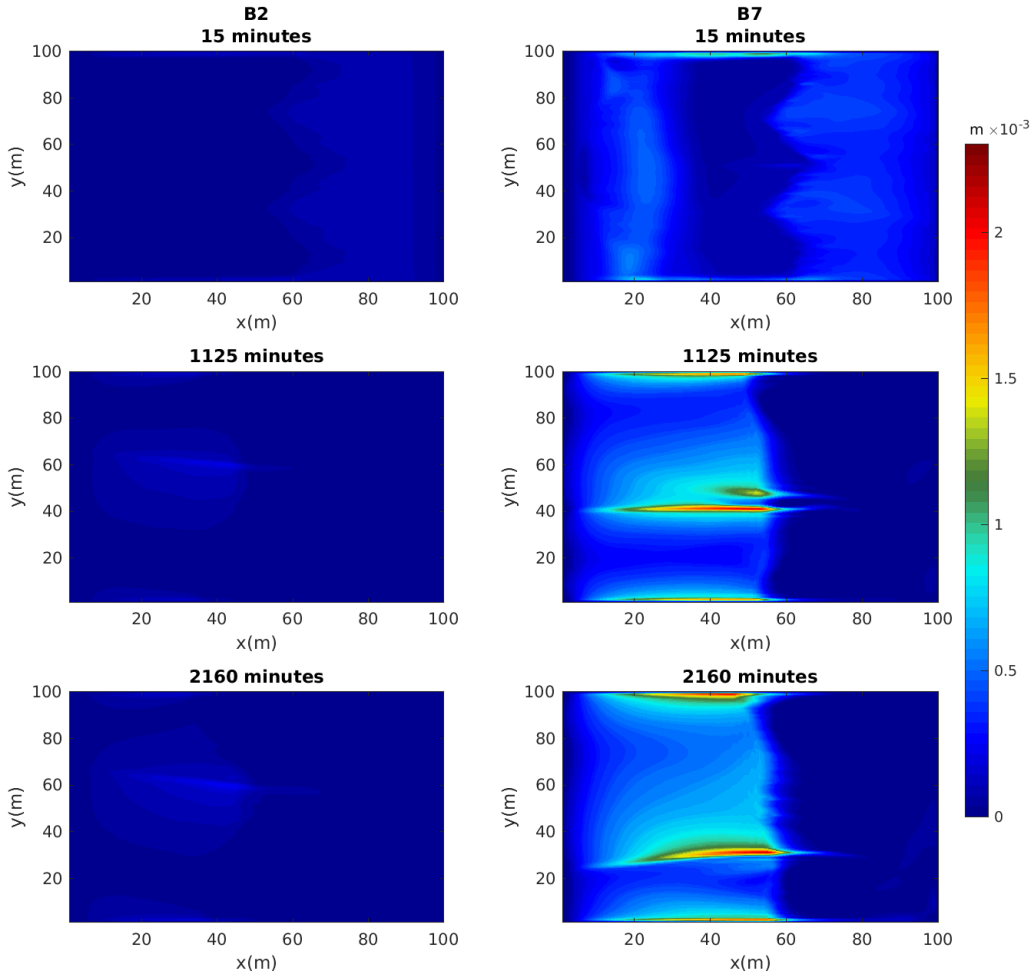

Figure 4.21: The kinetic energy of surface currents for cases B2 (left) and B7 (right) at 15 minutes, 1125 minutes (18 hours and 45 minutes), and 2160 minutes (36 hours). The only difference between cases B2 and B7 is that case B2 has 3 m/s wind forcing towards the right, and case B7 has a 6 m/s wind forcing towards the right.

Figure 4.22 shows the net upward heat flux, net upward surface shortwave radiation, net upward longwave radiation, latent heat flux, and sensible heat flux for cases B2-B7 over the 1.5 day simulation. Since we have wind forcing in all of these cases, there are nonzero latent

and sensible heat values for these cases unlike the previous chapter. Recalling equations 2.5.6 and 2.5.7, it is reasonable for the magnitude of the latent heat flux for case B7 to be so much larger than than the rest of the cases since the wind forcing is doubled in case B7. The rest of the variation found between cases for latent and sensible heat fluxes are likely due to surface temperature differences. Figure 4.23 shows that the average surface temperatures of cases B4, B5, and B6 are approximately 1.5°C warmer than the other cases. The increased surface temperature in these cases are due to the increased horizontal domain size and coarser horizontal resolution. As a result, it is reasonable that the latent heat flux for cases B4-B6 would be of larger magnitude compared to cases B2, and B3. A similar situation can be seen in the sensible heat flux panel of figure 4.22, the increased surface temperature of cases B4-B6 cause the sensible heat flux to fall below 0 W/m^2 for those cases. On the other hand, case B7 has an average surface temperature close to cases B2 and B3, and it has a stronger wind forcing, causing the sensible heat values to be larger than they are for cases B2 and B3.

Next, we will discuss the net upward surface shortwave radiation panel in figure 4.22. Note that all of the panels shown in figure 4.22 are averages taken across the entire horizontal domain (excluding boundary cells), however there is spatial variation between surface grid cells. Since there may be a wide range of surface albedo values over the total horizontal domain, we would expect the average net upward surface shortwave radiation values to vary over a wide range of values throughout the entire simulation as well. However, the numerical matrix of values for the net upward surface shortwave radiation was viewed over the course of the simulation (not shown here) and the results behave differently than expected, similar to what was seen for case A1 in figure 3.6. Equation 2.3.3 is supposedly used in the MITgcm for computing net upward surface shortwave radiation, according to the model documentation. The model should only be considering three different surface albedo values that are independent of ice thickness: dry ice, wet ice, and open water (see figure 2.3). However, the curves shown in the surface shortwave radiation plot are changing steadily over time. We noticed this same behaviour in chapter three for case A1. It is unclear as to why the curves for the net upward shortwave radiation are behaving in this manner. Studying the ice concentration for the simulations in this chapter may help explain the strange net upward surface shortwave radiation results. Another point to mention here is that cases B4 and B5 have very similar values for most of the plots shown in figure 4.22. This result is to be expected, given the only difference between the two cases is that one of them considers rotation and the other does not. However, one plot that cases B4 and B5 do differ slightly is the net upward surface shortwave radiation plot. Here, cases B4 and B5 start off very similar, but later on in the simulation case B4 has a slightly smaller magnitude for the net upward shortwave radiation than case B5. This difference in

radiation is most likely due to the difference in spatial distribution of ice thickness that we see in figure 4.8, case B5 appears to have more open-water cells which most likely accounts for the increase of solar radiation into the lake.

The net upward longwave radiation is computed according to equation 2.3.4. Figure 4.22 shows the net upward longwave radiation for cases B2-B7. Here, we observe that cases B2, B3, B5, B6, and B7 have relatively similar values, but the cases with the larger surface temperature values have slightly larger net upward longwave radiation values. This result is expected given equation 2.3.4. Finally, figure 4.22 also displays the net upward heat flux for cases B2-B7. These flux values were computed according to figure 2.3.5. Note that case B6 has a dip for net upward heat flux near the beginning of the simulation where it goes to approximately -3000 W m^{-2}. This does not seem physical, so we ignore this outlier. Moreover, case B6 appear quite noisy in general for the net upward heat flux, this seems unusual given the equation used to compute it. Other than case B6, the remainder of the net upward heat flux values appear to look reasonable.

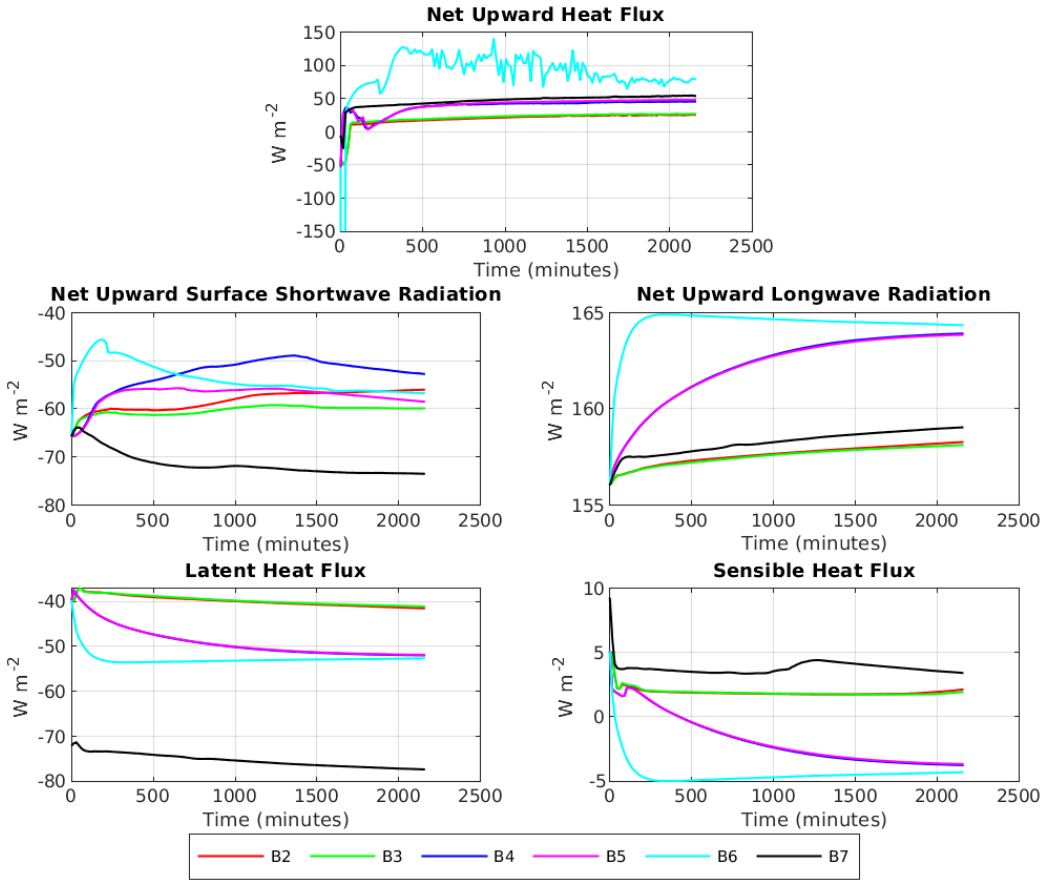

Figure 4.22: The average net upward heat flux, net upward surface shortwave radiation, net upward longwave radiation, latent heat flux, and sensible heat flux for cases B2-B7 over the entire 1.5 day simulation. The curves for cases B2 (red) and B3 (green) are largely overlapping for all plots shown in this figure. The curves for case B4 (dark blue) and case B5 (magenta) are also largely overlapping for the majority of the plots shown here. Cases B4, B5, and B7 also appear to be overlapping in the net upward heat flux plot.

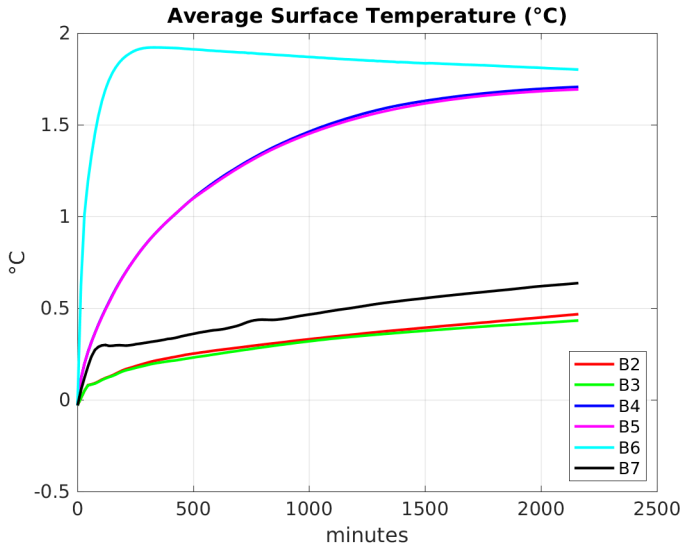

Figure 4.23: The average surface temperature for cases B2-B7 throughout the 1.5 day simulation. Note that there are three horizontal domain sizes and horizontal resolutions shown here: cases B2, B3, and B7 have a horizontal domain size of 100×100 m with a horizontal resolution of 1 m; cases B4 and B5 have a horizontal domain size of $1,000 \times 1,000$ m with a horizontal resolution of 10 m; and case B7 has a horizontal domain size of $10,000 \times 10,000$ m with a horizontal resolution of 100 m. Also note that the curves for cases B2 and B3 overlap in this figure as well as the curves for cases B4 and B5.

4.4 Concluding Remarks

This chapter explored idealized lake ice simulations using the MITgcm under wintertime conditions. The domain used for this thesis was a rectangular lake with 100 evenly spaced grid cells in the x, y, and z-directions. A uniformly 1 m thick ice mass covering approximately half the lake (see figure 4.1) was included with a frame of water surrounding the ice mass. The simulations discussed here varied from 100 m to 1 m in horizontal resolution. Other parameter settings varied here include wind forcing, rotation, and whether or not the model was executed using its fully nonhydrostatic capabilities or the hydrostatic approximation.

Largely, the simulations in this chapter behaved as expected. For instance, when there was no wind involved the ice fractured over the lake increasingly with time. When wind forcing exclusively towards the right was included, the ice would move the right boundary

and ice pile-up would occur. Increasing the magnitude of the wind forcing resulted in the ice reaching the right boundary sooner with more ice pile-up in terms of height. When rotation was turned off the ice formed a more symmetrical ice cover with a straighter ice-edge near the right boundary than when the model considered rotation. As the lake size increased, the ice mass took longer to reach the right boundary and less pile-up was observed. The kinetic energy results also behaved as expected for the most part.

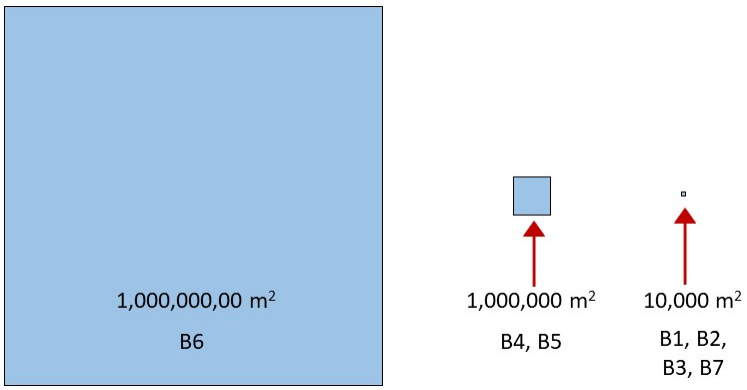

Figure 4.24: The relative size of the lakes considered in chapter four.

In this thesis, we always altered the horizontal domain size and horizontal resolution at the same time due to time restraints. The reason for changing both parameter simultaneously was so that we could always retain 100 grid cells in the x and y directions. The simulations with 100 cells in the x and y direction require approximately 36 hours to complete running when using the nonhydrostatic formulation. However, the amount of time the MITgcm would require to run a simulation that had a 1,000×1,000 m horizontal domain with a 1 m horizontal resolution would take significantly longer (approximately one month longer) to complete than a simulation with a 1,000×1,000 m horizontal domain with a 10 m horizontal resolution using the nonhydrostatic formulation. The largest lake we considered for this thesis was used in case B6. The horizontal lake size is 10,000×10,000 m with a 100 m horizontal resolution. For a size reference that demonstrates how much larger the lake is in case B6 compared to the rest of the cases from this chapter see figure 4.24. To truly untangle the impact of horizontal domain size and horizontal resolution, we should re-run cases B4 and B6 with the same background horizontal and vertical viscosities given for case B2, a 1 m horizontal resolution, and we should add more 'waves' to the discrete sine curve in the initial ice mass so that the length scale remains constant between cases.

It is worth spending some time discussing how case B6 differed in comparison to case B2 and B4. Firstly, the ice breaks up and moves across the lake differently in case B6 than we observe for cases B2 and B4. The ice initially fractures in case B2, (this is not seen in case B4), but then both case B2 and case B4 end up at the right boundary with ice gradually piling up. The ice tends to lean towards the south-east corner and does not completely make it to the right boundary for case B6. Moreover, the surface current appears to become less ordered as the lakes gets larger and the resolution becomes coarser. Rotation also appears to have a stronger influence as lake size increases. Referring to figure 4.16, we observe the profile of the velocity for case B6 in the bottom two panels. We notice that the velocity for case B6 is much noisier than what we see for cases B2 and B4. This is further demonstrated in figures 4.17, 4.18, and 4.19 which display the top-down view of the u-component of the velocity at $z = 0$ m, $z = -2$ m, and $z = -4$ m, respectively. According to figure 4.23, case B6 experiences an average surface temperature peak around the beginning of the simulation, this is a strange phenomena considering the model setup. This strange feature is also represented in the net upward heat flux panel in figure 4.22, there is a massive dip in this figure for case B6 to -3000 W m^{-2}, however the y-axis does not show that far. This figure also shows a lot of noise for case B6 for the net upward heat flux that is most likely related to the noise observed in the velocity and kinetic energy plots. It is likely that the primary cause of differences in results between cases B2, B4, and B6 are due to horizontal resolution more than horizontal domain size, but more work needs to be done before we can be certain.

There were a number of other strange or unexpected features observed in these simulations as well. Section 4.2 discusses the issues we had regarding ice movement with the EVP and LSOR momentum solvers without free-drift. We temporarily remedied this issue by using the LSOR solver with free-drift and including a frame of water around the initial ice mass. This may be a model issue related to the sub-grid and domain size, or it could be an issue due to an incorrect setup. More work is required to find a more permanent solution.

Perhaps one of the most puzzling results from these simulations are the surface heat fluxes, specifically we are experiencing troubling results from the net upward surface shortwave radiation. The model documentation, and everything we have found in the code itself, has stated that the net upward shortwave radiation is calculated according to equation 2.3.3, however the results displayed in figure 4.22 suggest that the computation is a function of ice thickness. More attention to this problem is required before we can be confident in the model results. The ice concentration results for cases B2-B7 should be studied to determine if they may explain the strange behaviour related to the net upward surface shortwave radiation we are observing.

Chapter 5

Discussion

Recent research suggests that wintertime processes are significantly increasing amounts of hypoxic water and HABs found in Lake Erie during the following summer [Twiss et al., 2012]. According to Assel et al. [2003], Assel [2004], a lake ice cover influences the transfer of mass and energy to and from the lake, which in turn impacts lake ecosystems. The majority of the mixing in Lake Erie is due to wind forcing and convection. This thesis explores high resolution lake ice simulations under wintertime conditions using the MITgcm. The aim of this thesis is to gain competence and clarity with the MITgcm and some of its packages so that we may confidently apply the model to future applications involving Lake Erie for further research. We considered several idealized simulations with varied parameter settings involving wind forcing, horizontal domain and resolution size, rotation, and whether or not the simulations were carried out using the hydrostatic or the fully nonhydrostatic version of the model. In this chapter we discuss the main conclusions derived from this work and future research to be done.

5.1 Conclusions

In this work, several simulations were executed with varied amounts of downward shortwave and longwave radiation, and initial surface and air temperatures in an attempt to understand an issue involving ice growth under inappropriate conditions. Increasing the air and surface temperature, as demonstrated in case A2, resulted in very small amounts of ice appearing. However, the model disregards the very small amount of ice for heat flux computations, suggesting that it is insignificant noise. For case A3, the downward

shortwave and longwave radiation was increased as well as the air and surface temperature. Only the downward shortwave and longwave radiation were increased in case A4. Results show that cases A3 and A4 both did not grow any ice. It is not clear why the lake is growing ice in case A1. The ice growth may be due to the fact that the lake is losing energy according to figure 3.6 and growing ice, then heat may be released as the ice is forming causing the surface to warm. One discovery made was that adding a small amount of wind forcing, such as 10^{-16} m/s, to case A1 would decrease the amount of ice appearing enough such that the heat flux computations would ignore it, and treat every cell as an open-water cell. This result suggests that our ice growth problem may not be a significant issue because more realistic simulations will likely always include some wind component.

Lakes were also simulated with a partial ice cover of constant thickness and varied horizontal lake size and resolution, wind forcing, and rotation. Whether or not the simulations were executed using the hydrostatic or the fully nonhydrostatic version of the model was also considered (see table 4.1). When no wind forcing is included, as in case B1, the results are as expected. The ice cover fractures over time as a result of the incoming radiation. When wind forcing is included, as in case B2, the ice mass is forced to the right boundary and ice pile-up occurs. Doubling the magnitude of the wind forcing, as in case B7, resulted in the ice reaching the right boundary sooner and increased amounts of ice pile-up. In general, the surface current tends to be stronger in the open-water regions and weaker in the ice-covered regions, implying that the ice is acting as a barrier between the lake and the wind forcing.

The impact of horizontal lake size, horizontal resolution, and background horizontal and vertical viscosities and diffusivities were tested through cases B2, B4, and B6 as displayed in tables 4.1 and 4.2. General observations from these cases indicate that larger lakes with coarser resolution require more time for the initial ice mass to reach the right boundary and have less ice pile-up in terms of height. The surface current also behaves differently depending on the resolution and lake size. For instance, the surface current seen for the smallest lake with the finest resolution, in case B2, is relatively symmetric. The strongest magnitude occurred near the middle of the lake, and there are recirculation patterns near the northern and southern boundaries. The mid-sized lake with the medium strength resolution, used for case B4, appears to have a similar circulation pattern than case B2, but the surface current is generally less ordered and lacks the same degree of symmetry. The largest lake with the coarsest resolution, in case B6, has a surface current that has much less order than the two smaller lakes under the ice. In addition, there is increased noise we can observe occurring in the largest lake with respect to velocity and the heat fluxes. The velocity profile for cases B2, B4, and B6 were also considered. Results from figure 4.16 show that the majority of the activity take place in the shallowest 4 m of the

lake, however we observe that as the lake gets larger and resolution gets coarser, more of the activity occurs closer to the surface. It is difficult to say for sure which component of our set up is causing the greatest discrepancy in results for cases B2, B4, and B6, however it seems more likely that resolution would be having a larger impact than size. It is also important to consider that the length scale if the initial ice mass also differed between cases B2, B4, and B6.

Effects of rotation were tested through case B4 and case B5. The results from this test do indicate that rotation has an influence on a lake of this size (1,000×1,000 m). The case that does consider rotation (case B4) certainly shows more movement in the y-direction compared to the case that does not consider rotation (case B5). The last feature we tested in this thesis was how results from the fully nonhydrostatic model would differ from those produced by the hydrostatic model. According to Marshall et al. [1997b], some processes that occur in water bodies are fundamentally nonhydrostatic, such as convection, and are not able to be accurately simulated using a hydrostatic model. Cases B2 and B3 have the same parameterizations except that case B2 was executed using the nonhydrostatic version of the model and case B3 was carried out using the hydrostatic version of the model. Results suggests that it does have an impact when we choose to use the hydrostatic over the fully nonhydrostatic version of the MITgcm. From figure 4.4, we observe that case B2 is very symmetric in its surface circulation, and case B3 lacks this same symmetry.

Kinetic energy of surface currents were also examined for cases B2-B7. One interesting feature observed from these plots was that the size of the lake, as well as the resolution, played an important role in the local kinetic every values. The larger the lake and the coarser the resolution, the lower the local kinetic energy values tended to be. This result is to be expected since we also noticed a decrease in the magnitude of the surface currents as the lake got larger and the resolution beame coarser. Other than that, there were not too many surprises in the plots of surface kinetic energy, they indicated where the most energy occurred for the simulations. As we saw with the spatial distribution of the ice thickness plots, the vast majority of the higher magnitude energy is located in the open-water regions. Another expected result is that the kinetic energy also has a much stronger magnitude when the wind is stronger.

5.2 Current Issues and Future Work

There are three main issues that we discovered while examining the results of the simulations presented in this thesis, and the first issue is related to ice growing under inappropriate conditions. Chapter three discusses simulations that are growing ice even when the surface

and air temperatures are above freezing, and incoming shortwave and longwave radiation is included. This should not be happening and it influences the heat flux computations since the model considers there to be an ice cover over the domain. With the addition of a very small wind forcing (10^{-16} W/m^2) in the x direction, we were able to avoid significant amounts of ice appearing however. Since more realistic simulations will most likely contain some wind forcing, the ice growth issue we experienced in chapter three may not be a huge problem. Nevertheless, more work should be done to figure out why there is an initial ice growth in the first place.

The second issue we found is associated with the momentum solvers and the ice remaining stagnant under significant wind forcing. We tested out three momentum solvers and ice rheologies: EVP, LSOR with free-drift, and LSOR with no free-drift. Results when using the EVP momentum solver showed that, when wind forcing was included, the vast majority of the ice remained stagnant at the left boundary. We observed that the LSOR momentum solver without free-drift allowed for even less movement than the EVP solver did. Finally, we noticed that the LSOR momentum solver with free-drift did allow for ice movement, but the ice closest to the left boundary would remain still throughout the simulation. A temporary fix for this problem of using the LSOR solver with free-drift rheology and a frame of water around the initial ice cover was introduced. We believe that this is a model issue related to the subgrid and domain size. The problems regarding the momentum solver could also be due to an issue with the solver setup and flags. More work needs to be done to determine a more permanent solution to this problem.

The final significant issue we discovered is in regards to the net upward shortwave heat flux and the confusion surrounding how the model computes it. The model documentation states that the computation for the net upward surface shortwave radiation is completed according to equation 2.3.3. The only nonzero terms involved in this equation are the downward shortwave radiation and the surface albedo. In this thesis, the downward shortwave radiation is a constant value, and the surface albedo may only take on one of three values (0.1, 0.66, or 0.75) depending on the surface type. Regardless of this information, the MITgcm appears to be calculating the net upward surface shortwave radiation as a function of ice thickness (see figures 3.6 and 4.22). This makes sense physically, but does not agree with the equations for the model that we have found in the documentation. The problem may be due to an ice concentration that is in-between the values of 0 and 1 causing the average surface albedo to take on a range of values. This problem requires urgent attention before model results may be trusted for future applications.

Once the above issues have been addressed, there are still many factors to consider that were not included in this thesis. One of these factors involve ice fracture and surface currents for larger lakes with coarser resolutions. Results from chapter four indicate that

the surface currents and ice fractures behave differently for the larger lake with the coarsest resolution in case B6 than it did for the smaller lakes with finer resolution. Primary differences were most likely due to resolution differences as opposed to size differences. Horizontal domain size and horizontal resolution were always varied together in this thesis because of time restraints. However, it would be interesting to run a simulation for longer and increase the horizontal resolution for a larger lake. Furthermore, the background horizontal and vertical diffusion and viscosity coefficients should be held constant. The length scale used for the initial ice mass should also be held constant between simulations. The MITgcm has been used in previous studies with many different sized water bodies and horizontal resolutions, however the horizontal resolutions used in this thesis have been on the higher-end of the range. For instance, a non-exhaustive, search shows that the MITgcm was used to simulate the Gulf of Trieste using a 250 m horizontal resolution according to Querin et al. [2007], Bennington et al. [2010] utilized the MITgcm with a horizontal resolution of 2 km to simulate Lake Superior, a 450 m horizontal resolution was used in a study by Dorostkar et al. [2010] where they applied the MITgcm to Cayuga Lake, Djoumna et al. [2014] used the MITgcm with a 2 km horizontal resolution to simulate Lake Erie, and Padon and Ashkenazy [2018] performed simulations with the MITgcm using a 100 m horizontal resolution on the Dead Sea. Note that none of these previously mentioned studies included ice.

Another factor that we wish to consider in the future is snow, as Lake Erie deals with snowfall during the winter months. As was briefly mentioned in chapter one, snow is an important component of lake ice. If heavy enough, snow can cause the ice to lower beneath the lake surface and produce slush. Moreover, this thesis discusses the impact an ice cover has on heat transfer between the lake and atmosphere, and this interaction is further impeded if snow is involved [Leppäranta, 2015]. The lack of snow is just one of the ways in which the simulations considered in this thesis are highly idealized. We only considered rectangular domains with flat bottom topographies and equally spaced grid cells. Constant wind forcing exclusively in one direction was included. Furthermore, the incoming radiation was always constant and we only considered equivalent amounts of downward shortwave and longwave radiation.

Bibliography

Alistair Adcroft and Jean Michel Campin. Rescaled height coordinates for accurate representation of free-surface flows in ocean circulation models. *Ocean Modelling*, 7(3-4): 269–284, 2004. ISSN 14635003. doi: 10.1016/j.ocemod.2003.09.003.

Alistair Adcroft, Chris Hill, Jean-michel Campin, John Marshall, and Patrick Heimbach. Overview of the Formulation and Numerics of the MIT GCM. pages 139–149. ECMWF, 2004.

Aymond A. Assel. An ice-cover climatology for lake erie and lake superior for the winter seasons 1897–1898 to 1982–1983. *International Journal of Climatology*, 10(7):731–748, 1990. ISSN 10970088. doi: 10.1002/joc.3370100707.

Raymond Assel, Kevin Cronk, and David Norton. Recent trends in Laurentian Great Lakes ice cover. *Climatic Change*, 57(1-2):185–204, 2003. ISSN 01650009. doi: 10.1023/A:1022140604052.

Raymond A. Assel. Lake Erie Ice Cover Climatology – Basin Averaged Ice Cover: Winter 1898-2002. *NOAA Technical Memorandum*, pages 1–15, 2004.

Val Bennington, Galen A. McKinley, Nobuaki Kimura, and Chin H. Wu. General circulation of Lake Superior: Mean, variability, and trends from 1979 to 2006. *Journal of Geophysical Research: Oceans*, 115(12):1–14, 2010. ISSN 21699291. doi: 10.1029/2010JC006261.

W. P. Budgell. Numerical simulation of ice-ocean variability in the Barents Sea region. *Ocean Dynamics*, 55(3-4):370–387, 2005. ISSN 1616-7341. doi: 10.1007/s10236-005-0008-3.

M. C. Buijsman, Y. Kanarska, and J. C. McWilliams. On the generation and evolution of nonlinear internal waves in the South China Sea. *Journal of Geophysical Research: Oceans*, 115(2):1–17, 2010. ISSN 21699291. doi: 10.1029/2009JC005275.

William J. Campbell. The wind-driven circulation of ice and water in a polar ocean. *Journal of Geophysical Research*, 70(14):3279–3301, 1965. ISSN 0148-0227. doi: 10.1029/jz070i014p03279.

David C. Chandler. Limnological studies of western Lake Erie: I. Plankton and certain physical-chemical data of the Bass Islands region, from September 1938, to November, 1939. *The Ohio Journal of Science*, XL(6), 1940.

David C. Chandler. Limnological studies of western Lake Erie: III. Phytoplankton and physical-chemical data from November, 1939, to November, 1940. *The Ohio Journal of Science*, 1942a.

David C. Chandler. Limnological Studies of Western Lake Erie: II. Light Penetration and Its Relation to Turbidity. *Ecology*, 23(1):41–52, 1942b.

David C. Chandler. Limnological Studies of Western Lake Erie IV. Relation of Limnological and Climatic Factors to the Phytoplankton of 1941. *Transactions of the American Microscopical Society*, 63(3):203–236, 1944.

David C. Chandler. Limnological Studies of Western Lake Erie: V. Relation of Limnological and Meteorological Conditions to the Production of Phytoplankton in 1942. *Ecological Monographs*, 15(4):435–457, 1945.

Changsheng Chen, Robert C. Beardsley, and Geoffrey Cowles. An unstructured-grid, finite-volume coastal ocean model (FVCOM) system. *Oceanography*, 19(SPL.ISS. 1):78–89, 2006. ISSN 10428275. doi: 10.5670/oceanog.2006.92.

Changsheng Chen, Haosheng Huang, Robert C. Beardsley, Qichun Xu, Richard Limeburner, Geoffrey W. Cowles, Yunfang Sun, Jianhua Qi, and Huichan Lin. Tidal dynamics in the Gulf of Maine and New England Shelf: An application of FVCOM. *Journal of Geophysical Research: Oceans*, 116(12), 2011. ISSN 21699291. doi: 10.1029/2011JC007054.

Paul F. Choboter, Mariangel Garcia, Dany De Cecchis, Mary Thomas, and Ryan K. Walter. Nesting Nonhydrostatic GCCOM within Hydrostatic ROMS for Multiscale Coastal Ocean Modeling. (September), 2016. doi: 10.1109/OCEANS.2016.7761488.

Thomas E. Croley and Raymond A. Assel. A one-dimensional ice thermodynamics model for the Laurentian Great Lakes. *Water Resources Research*, 30(3):625–639, 1994. ISSN 19447973. doi: 10.1029/93WR03415.

G. Djoumna, K. G. Lamb, and Yerubandi R. Rao. Sensitivity of the parameterizations of vertical mixing and radiative heat fluxes on the seasonal evolution of the thermal structure of Lake Erie. *Atmosphere - Ocean*, 52(4):294–313, 2014. ISSN 14809214. doi: 10.1080/07055900.2014.939824. URL http://dx.doi.org/10.1080/07055900.2014.939824.

A. Dorostkar, L. Boegman, P. J. Diamessis, and A. Pollard. Sensitivity of MITgcm to different model parameters in application to Cayuga Lake. *Environmental Hydraulics - Proceedings of the 6th International Symposium on Environmental Hydraulics*, 1(June): 373–378, 2010. doi: 10.1201/b10553-58.

N. A. D'souza, Y. Kawarasaki, J. D. Gantz, R. E. Lee, B. F.N. Beall, Y. M. Shtarkman, Z. A. Koçer, S. O. Rogers, H. Wildschutte, G. S. Bullerjahn, and R. M.L. McKay. Diatom assemblages promote ice formation in large lakes. *ISME Journal*, 7(8):1632–1640, 2013. ISSN 17517362. doi: 10.1038/ismej.2013.49.

Claude R. Duguay, Greg M. Flato, Martin O. Jeffries, Patrick Ménard, Kim Morris, and Wayne R. Rouse. Ice-cover variability on shallow lakes at high latitudes: Model simulations and observations. *Hydrological Processes*, 17:3465–3483, 2003. ISSN 1550445X. doi: 10.1109/AINA.2010.136.

Frederic Dupont, Padala Chittibabu, Vincent Fortin, Yerubandi R. Rao, and Youyu Lu. Assessment of a NEMO-based hydrodynamic modelling system for the Great Lakes. *Water Quality Research Journal of Canada*, 47(3-4):198–214, 2012. ISSN 12013080. doi: 10.2166/wqrjc.2012.014.

Elizabeth E. Ebert and Judith A. Curry. An intermediate one-dimensional thermodynamic sea ice model for investigating ice-atmosphere interactions. *Journal of Geophysical Research*, 98(C6):10085, 1993. ISSN 0148-0227. doi: 10.1029/93jc00656.

T. Fichefet and M. A. Morales Maqueda. Sensitivity of a global sea ice model to the treatment of ice thermodynamics and dynamics. *Journal of Geophysical Research: Oceans*, 102(C6):12609–12646, 1997. ISSN 21699291. doi: 10.1029/97JC00480.

Gregory M. Flato and Ross D. Brown. Variability and climate sensitivity of landfast Arctic sea ice. *Journal of Geophysical Research C: Oceans*, 101(C11):25767–25777, 1996. ISSN 01480227. doi: 10.1029/96JC02431.

Ayumi Fujisaki, Jia Wang, Haoguo Hu, David J. Schwab, Nathan Hawley, and Yerubandi R. Rao. A modeling study of ice-water processes for Lake Erie applying

coupled ice-circulation models. *Journal of Great Lakes Research*, 38(4):585–599, 2012. ISSN 03801330. doi: 10.1016/j.jglr.2012.09.021. URL http://dx.doi.org/10.1016/j.jglr.2012.09.021.

Nathan Hawley, Dmitry Beletsky, and Jia Wang. Ice thickness measurements in Lake Erie during the winter of 2010–2011. *Journal of Great Lakes Research*, 44(3):388–397, 2018. ISSN 03801330. doi: 10.1016/j.jglr.2018.04.004. URL https://doi.org/10.1016/j.jglr.2018.04.004.

W. D. Hibler. Modeling a variable thickness sea ice cover. *Monthly Weather Review*, 108 (12):1943–1973, 1980. ISSN 00270644. doi: 10.1175/1520-0493(1980)108⟨1943:MAVTSI⟩2.0.CO;2.

W. D. Hibler III. A Dynamic Thermodynamic Sea Ice Model. *Journal of Physical Oceanography*, 9:815–846, 1979.

E. C. Hunke and William H. Lipscomb. CICE : the Los Alamos Sea Ice Model Documentation and Software User's Manual LA-CC-06-012. *Research Report*, pages 1–76, 2010. ISSN 0022-202X. doi: 10.1111/j.1523-1747.2003.12629.x.

Mari F. Jensen, Kerim H. Nisancioglu, and Michael A. Spall. Large changes in sea ice triggered by small changes in Atlantic water temperature. *Journal of Climate*, 31(12): 4847–4863, 2018. ISSN 08948755. doi: 10.1175/JCLI-D-17-0802.1.

Y. Kanarska, A. Shchepetkin, and J. C. McWilliams. Algorithm for non-hydrostatic dynamics in the Regional Oceanic Modeling System. *Ocean Modelling*, 18(3-4):143–174, 2007. ISSN 14635003. doi: 10.1016/j.ocemod.2007.04.001.

Jeremy L. Kasper and Thomas J. Weingartner. The spreading of a buoyant plume beneath a landfast ice cover. *Journal of Physical Oceanography*, 45(2):478–494, 2015. ISSN 15200485. doi: 10.1175/JPO-D-14-0101.1.

G. Kirillin, J. Hochschild, D. Mironov, A. Terzhevik, S. Golosov, and G. Nützmann. FLake-Global: Online lake model with worldwide coverage. *Environmental Modelling & Software*, 26(5):683–684, 5 2011. ISSN 13648152. doi: 10.1016/j.envsoft.2010.12.004. URL https://linkinghub.elsevier.com/retrieve/pii/S1364815210003245.

Zhigang Lai, Changsheng Chen, Geoffrey W. Cowles, and Robert C. Beardsley. A nonhydrostatic version of FVCOM: 2. Mechanistic study of tidally generated nonlinear internal waves in Massachusetts Bay. *Journal of Geophysical Research: Oceans*, 115(12):1–21, 2010a. ISSN 21699291. doi: 10.1029/2010JC006331.

Zhigang Lai, Changsheng Chen, Geoffrey W. Cowles, and Robert C. Beardsley. A non-hydrostatic version of FVCOM: 1. Validation experiments. *Journal of Geophysical Research: Oceans*, 115(11):1–23, 2010b. ISSN 21699291. doi: 10.1029/2009JC005525.

W. G. Large and S. Pond. Open ocean momentum flux measurements in moderate to strong winds. *Journal of Physical Oceanography*, 11(3 , Mar. 1981):324–336, 1981. ISSN 00223670. doi: 10.1175/1520-0485(1981)011⟨0324:OOMFMI⟩2.0.CO;2.

W. G. Large and S. Pond. Sensible and Latent Heat Flux Measurements over the Ocean. *Journal of Physical Oceanography*, 12(5):464–482, 1982. ISSN 0022-3670. doi: 10.1175/1520-0485(1982)012⟨0464:salhfm⟩2.0.co;2.

W. G Large, J C Mcwilliams, and S C Doney. Oceanic With Vertical Mixing : a Review Layer and a Model a Nonlocal Boundary. *Reviews of Geophisics*, (94):363–403, 1994.

Jean François Lemieux, Bruno Tremblay, Jan Sedláček, Paul Tupper, Stephen Thomas, David Huard, and Jean Pierre Auclair. Improving the numerical convergence of viscous-plastic sea ice models with the Jacobian-free Newton-Krylov method. *Journal of Computational Physics*, 2010. ISSN 10902716. doi: 10.1016/j.jcp.2009.12.011.

Matti Leppäranta. The Impact of Climate Change on European Lakes. In *The Impact of Climate Change on European Lakes*, chapter Chapter 5. Springer-Verlag., 2009. ISBN 9789048129454. doi: 10.1007/978-90-481-2945-4.

Matti Leppäranta. *Freezing of lakes and the evolution of their ice cover*. Published in association with Praxis Publishing, Chichester, UK, 2015. ISBN 9783642290817. doi: 10.1007/978-3-642-29081-7.

Matti Leppäranta and Keguang Wang. The ice cover on small and large lakes: Scaling analysis and mathematical modelling. *Hydrobiologia*, 599(1):183–189, 2008. ISSN 00188158. doi: 10.1007/s10750-007-9201-3.

Martin Losch, Dimitris Menemenlis, Jean Michel Campin, Patick Heimbach, and Chris Hill. On the formulation of sea-ice models. Part 1: Effects of different solver implementations and parameterizations. *Ocean Modelling*, 33(1-2):129–144, 2010. ISSN 14635003. doi: 10.1016/j.ocemod.2009.12.008. URL http://dx.doi.org/10.1016/j.ocemod.2009.12.008.

John J. Magnuson, Dale M. Robertson, Barbara J. Benson, Randolph H. Wynne, David M. Livingstone, Tadashi Arai, Raymond A. Assel, Roger G. Barry, Virginia Card, Esko Kuusisto, Nick G. Granin, Terry D. Prowse, Kenton M. Stewart, and Valery S. Vuglinski.

Historical Trends in Lake and River Ice Cover in the Northern Hemisphere. Technical report, 2000.

S. Manabe, K. Bryan, and M. J. Spelman. A global ocean—Atmosphere climate model with seasonal variation for future studies of climate sensitivity. *Dynamics of Atmospheres and Oceans*, 5(2):137, 1980. ISSN 03770265. doi: 10.1016/0377-0265(80)90022-6.

John Marshall, Alistair Adcroft, Chris Hill, Lev Perelman, and Curt Heisey. A finite-volume, incompressible navier stokes model for, studies of the ocean on parallel computers. *Journal of Geophysical Research C: Oceans*, 102(C3):5753–5766, 1997a. ISSN 01480227. doi: 10.1029/96JC02775.

John Marshall, Chris Hill, Lev Perelman, and Alistair Adcroft. Hydrostatic, quasi-hydrostatic, and nonhydrostatic ocean modeling. *Journal of Geophysical Research*, 102: 5733–5752, 1997b.

Maykut GA and Untrersteiner N. Some results from a time- dependent thermodynamic model of sea ice. *J Geophys Res*, 76(6):1550–1575, 1971. doi: 10.1029/jc076i006p01550.

Patrick Ménard, Claude R. Duguay, Greg M. Flato, and Wayne R. Rouse. Simulation of ice phenology on Great Slave Lake, Northwest Territories, Canada. *Hydrological Processes*, 16(18):3691–3706, 2002. ISSN 08856087. doi: 10.1002/hyp.1230.

NEMO Sea Ice Working Group. *Sea Ice modelling Integrated Initiative (SI^3) – The NEMO Sea Ice engine*.

NEMO System Team. *NEMO ocean engine*.

NEMO TOP Working Group. *Tracers in Ocean Paradigm (TOP) – The NEMO Tracers engine*.

K. H. Nicholls. El Niño, Ice Cover, and Great Lakes Phosphorus: Implications for Climate Warming. *Limnology and Oceanography*, 43(4):715–719, 1998.

Qianru Niu, Meng Xia, Edward S. Rutherford, Doran M. Mason, Eric J. Anderson, and David J. Schwab. Investigation of interbasin exchange and interannual variability in Lake Erie using an unstructured-grid hydrodynamic model. *Journal of Geophysical Research C: Oceans*, 120(3):2212–2232, 2015. ISSN 21699291. doi: 10.1002/2014JC010457.

Oded Padon and Yosef Ashkenazy. Non-hydrostatic effects in the Dead Sea. *Journal of Marine Systems*, 187(June):36–51, 2018. ISSN 09247963. doi: 10.1016/j.jmarsys.2018.06.007.

Claire L. Parkinson and Warren M. Washington. Large-Scale Numerical Model of Sea Ice. *J Geophys Res*, 84(C1):311–337, 1979. ISSN 00221406. doi: 10.1029/jc084ic01p00311.

Stefano Querin, Alessandro Crise, Davide Deponte, and Cosimo Solidoro. Numerical study of the role of wind forcing and freshwater buoyancy input on the circulation in a shallow embayment (Gulf of Trieste , Northern Adriatic Sea). *Journal of Geophysical Research*, 111:1–19, 2007. doi: 10.1029/2006JC003611.

D. A. Randall. Single-Column Models as a Bridge Between Observations and Climate Models How Do We Test Parameterizations for GCMs ? Single-Column Model. In *ARM Science Meeting*, pages 1–3.

D. Reinert, F. Prill, H. Frank, and G. Zängl. Parameterization of Lakes in Numerical Weather Prediction. Description of a lake Model. *Consortium for Small-Scale Modelling*, (11):2000, 2008. doi: 10.5676/DWD{_}pub/nwv/cosmo-tr{_}1.

Andrew F. Roberts, Elizabeth C. Hunke, Richard Allard, David A. Bailey, Anthony P. Craig, Jean-françois Lemieux, and Matthew D. Turner. Quality control for model development Subject Areas : Author for correspondence :. *Philosophical Transactions of the Royal Society A: Mathematical, Physical and Engineering Sciences*, 376:1–18, 2018.

K. Salonen, M. Leppäranta, M. Viljanen, and R. D. Gulati. Perspectives in winter limnology: Closing the annual cycle of freezing lakes. *Aquatic Ecology*, 43(3):609–616, 2009. ISSN 13862588. doi: 10.1007/s10452-009-9278-z.

Tido Semmler, Bin Cheng, Yu Yang, and Laura Rontu. Snow and ice on Bear Lake (Alaska) - sensitivity experiments with two lake ice models. *Tellus, Series A: Dynamic Meteorology and Oceanography*, 64(1), 2012. ISSN 02806495. doi: 10.3402/tellusa.v64i0.17339.

Albert J. Semtner. A Model for the Thermodynamic Growth of Sea Ice in Numerical Investigations of Climate, 1976. ISSN 0022-3670.

J. Smagorinsky. General Circulation Experiments With the Primitive Equations. *Monthly Weather Review*, 91(3):99–164, 1963. ISSN 0027-0644. doi: 10.1175/1520-0493(1963)091⟨0099:gcewtp⟩2.3.co;2.

A. S. Thorndike, D. A. Rothrock, G. A. Maykut, and R. Colony. The thickness distribution of sea ice. *Journal of Geophysical Research*, 80(33):4501–4513, 1975. doi: 10.1029/jc080i033p04501.

Kristen Thyng, Chad Greene, Robert Hetland, Heather Zimmerle, and Steven DiMarco. True colors of oceanography: Guidelines for effective and accurate colormap selection. *Oceanography*, 29(3):9–13, 2016. doi: 10.5670/oceanog.2016.66.

M. R. Twiss, R. M.L. McKay, R. A. Bourbonniere, G. S. Bullerjahn, H. J. Carrick, R. E.H. Smith, J. G. Winter, N. A. D'souza, P. C. Furey, A. R. Lashaway, M. A. Saxton, and S. W. Wilhelm. Diatoms abound in ice-covered Lake Erie: An investigation of offshore winter limnology in Lake Erie over the period 2007 to 2010. *Journal of Great Lakes Research*, 38(1):18–30, 2012. ISSN 03801330. doi: 10.1016/j.jglr.2011.12.008. URL http://dx.doi.org/10.1016/j.jglr.2011.12.008.

Luke Van Roekel, Alistair J. Adcroft, Gokhan Danabasoglu, Stephen M. Griffies, Brian Kauffman, William Large, Michael Levy, Brandon G. Reichl, Todd Ringler, and Martin Schmidt. The KPP Boundary Layer Scheme for the Ocean: Revisiting Its Formulation and Benchmarking One-Dimensional Simulations Relative to LES. *Journal of Advances in Modeling Earth Systems*, 10(11):2647–2685, 2018. ISSN 19422466. doi: 10.1029/2018MS001336.

Jia Wang, Haoguo Hu, David Schwab, George Leshkevich, Dmitry Beletsky, Nathan Hawley, and Anne Clites. Development of the Great Lakes Ice-circulation Model (GLIM): Application to Lake Erie in 2003-2004. *Journal of Great Lakes Research*, 36(3):425–436, 2010. ISSN 03801330. doi: 10.1016/j.jglr.2010.04.002. URL http://dx.doi.org/10.1016/j.jglr.2010.04.002.

Brooke White, Jay Austin, and Katsumi Matsumoto. A three-dimensional model of Lake Superior with ice and biogeochemistry. *Journal of Great Lakes Research*, 38(1):61–71, 2012. ISSN 03801330. doi: 10.1016/j.jglr.2011.12.006. URL http://dx.doi.org/10.1016/j.jglr.2011.12.006.

Miles C. Wilson, Jennifer A. Shore, and Yerubandi R. Rao. Sensitivity of the simulated kingston basin-lake ontario summer temperature profile using FVCOM. *Atmosphere - Ocean*, 51(3):319–331, 2013. ISSN 07055900. doi: 10.1080/07055900.2013.800017.

Jinlun Zhang and W. D. Hibler III. On an efficient numerical method for modeling sea ice dynamics. *Journal of Geophysical Research*, 102:8691–8702, 1997.

APPENDICES

Appendix A

Experiences with the MITgcm

A.1 Problems Encountered and Possible Solutions

The timestep is a very important parameter that can have a significant influence over how quickly the model runs, and if the model remains stable. One problem that we came across while using the MITgcm is that we had trouble lowering the timestep below 1.0 s. An undergraduate researcher, Senja Walberg, discovered how to fix this issue. To lower the timestep below 1.0 s in the MITgcm, perform the following:

- In the `packages.conf` file, include the line `-cal`.
- In the `data.pkg` file, either include the line `useCAL=.FALSE.` or simply do not include the calendar package at all in that file.
- Be sure that none of the other data files are reliant on information related to the calendar package.
- Set the timestep parameter `deltaT` to be the desired value.

Setting up the KPP package could also cause some issues. To get the KPP package to function properly, do the following:

- Enable the KPP package according to the KPP documentation[1].
- If experiencing difficulty, either adding a very small amount of wind (e.g. order of 1E-16) or lowering the timestep may fix the problem.

[1] https://mitgcm.readthedocs.io/en/latest/phys_pkgs/kpp.html

A.2 Tips for Using the MITgcm

There can be a steep learning curve to using the MITgcm, especially if the user does not have any similar experiences. To help make the transition slightly smoother, see the Fluid's Wiki page for MITgcm tips[2]. The following presents more tips for using the MITgcm:

- Most of the simulations executed in this thesis took approximately two days to complete running on the Compute Canada machine, Graham[3] using 100 processors. If the model is running too slowly, consider trying one of the following if appropriate for the situation:
  - Increase the timestep.
  - Decrease the domain size, or use a coarser resolution.
  - Use the hydrostatic version of the model.
  - Use free-drift rheology.
  - Do not use the KPP package.
- It helps to avoid confusion if all data files and files affecting model parameterizations are in the same directory as the executable file when running the model. Then, if a parameter needs to be modified it can be done in the same directory. This also makes it easier to determine the specifics of a past model setup.

[2] https://wiki.math.uwaterloo.ca/fluidswiki/index.php?title=MITgcm_tips
[3] https://docs.computecanada.ca/wiki/Graham